ZTF-FCT
Zientzia eta Teknologia Fakultatea
Facultad de Ciencia y Tecnología

emari ta zabal zazu
Universidad del País Vasco
Euskal Herriko Unibertsitatea

Functional bent-core liquid crystals studied through second harmonic generation and X-ray diffraction

JESÚS MARTÍNEZ PERDIGUERO
(jesus.martinez@ehu.eus)

Advisor:
Jesús Etxebarria Ecenarro

Department of Condensed Matter Physics
Faculty of Science and Technology
University of the Basque Country

A thesis to apply for the the degree of Doctor of Physics, mention “Doctor Europeus”

July 2009

- *Euskal Herriko Unibertsitateko (UPV/EHU) Argitalpen Zerbitzua*
- University of the Basque Country - UPV/EHU Press
- ISBN: 978-84-9082-459-7

Agradecimientos/Acknowledgments

Lo primero es agradecer a mi director, Jesús Etxebarria, la confianza que depositó en mí cuando me aceptó como su doctorando para hacer lo que ha resultado en la presente memoria. Fue un buen profesor durante la carrera y ha sido un excelente director de tesis.

Los otros dos jefazos, César Folcia y Josu Ortega, también me han guiado durante este tiempo y su contribución para que esta tesis sea lo que es ha sido inestimable.

Y ahora que se acabaron los agradecimientos por cortesía, le toca al Dr. Ibon Alonso, con el cual he compartido largas horas de trabajo de laboratorio (largas normalmente por su culpa) y con quien he trabajado muy a gusto en todo momento. Más que agradecerle su aportación para la conclusión de esta tesis le agradezco su compañía y amistad.

Sin la ayuda, paciencia e interés de Raúl Montero de la Facilidad Láser de la UPV/EHU las medidas a largas longitudes de onda no habrían sido posibles y las largas horas ahí abajo habrían sido mucho más aburridas.

Los químicos también son necesarios en el campo de los cristales líquidos y tan solo gracias a las "minúsculas" cantidades de material que han tenido la gentileza de mandarnos hemos podido hacer algo. El competente grupo de químicos de la Universidad de Zaragoza ha sido nuestro principal proveedor. Por lo que me toca, he de mencionar a Inmacula Pintre, Nélida Gimeno y Blanca Ros. Among chemists, I am also grateful to Yongqiang Zhang from Displaytech, in Boulder CO, for the nice collaboration we have shared and the interest he has showed in our work.

Since I spent the last months of my doctorate in the University of Warsaw, there are people I want to thank there too. Profs. Gorecka and Pociecha accepted me in their group and were patient enough to clarify all my doubts. Phd. students Karolina and Mirek also welcomed me and made my stay enjoyable.

Luego está el resto de gente de los becádromos, que me han desviado de mis labores investigadoras con incontables horas de procrastinación. Por miedo a olvidarme de alguien (o de no recordar su nombre) no voy a nombrar a todos estos, ahora amigos, que han compartido conmingo esas horas tan necesarias como las de trabajo.

Como esto de hacer la tesis no puede ser todo científicos, también agradezco a amigos y familia la compañia y el apoyo que me han brindado durante todo este tiempo.

Finalmente quiero dar las gracias al Gobierno Vasco el apoyo económico durante estos años. También a los proyectos de investigación del Ministerio de Educación y Cienca (MAT2006-13571-C02 y MAT2003-07806-C02-02), de la UPV/EHU (9/UPV 00060.310-13562/2001) y Gobierno Vasco (IT-484-07)

Table of Contents

Chapter 1

Introduction

Usually a thesis is written for people working in the same or in a related field, for people who are already familiar with the subject and with the jargon used in it. Due to that, I am not going to give here an extensive introduction but just shed some light on the phenomena this thesis deals with.

For those wanting a sounder introduction to liquid crystals, there are plenty of good references that could be used, but I am very fond of [1] and [2], maybe because they were my first reading materials. In the topic of bent-core liquid crystals I highly recommend the reviews by Reddy and Tshierske [3], Takezoe and Takanishi [4] and Etxebarria and Ros [5]; three new reviews containing pretty much everything discovered until a couple of years ago. Non-linear optics is the other key point in this thesis. For this, I have followed my "bible" on the subject [6]. Also I have to mention that my lab mate Ibon Alonso's [7] and Michi Nakata's [8] dissertations have excellent and very handy introductory chapters on all these topics.

Liquid crystals

The denomination "liquid crystal" was coined on the verge of the 20th century by Otto Lehmann [9] to enlighten the properties of some interesting materials showing properties of both liquids (fluidity) and crystals (anisotropy) that his colleague Friedrich Reinitzer had sent him. The latter had noticed what he called "double melting" in some derivatives of cholesterol [10]. Upon heating, the crystal first melted to a cloudy liquid before transforming into a transparent liquid. So it was the discovery of this state of matter, which was left as not much more than a mere curiosity until its application to the liquid crystal display industry in the 1960s. That boost in liquid crystal research lasts still now, and impressive advances in the understanding of these materials have been made. But much more research is necessary because, for example, apart from the numerous technical applications, liquid crystal has been found to be an essential requirement for living matter [11][12].

There are no written rules about which materials will show liquid crystal phases, but it is known that molecules must posses a high structural anisotropy. Starting from this fact, one can now think of a molecular crystal possessing long-range order of the positions of the constituent molecules and, in addition, a long-range order of their orientations. If the temperature is increased, the crystal will eventually melt to an isotropic liquid, but as Reinitzer saw, this transition can take place in steps. These steps occur because of the different energies necessary to unleash the different inter-molecular and intramolecular degrees of freedom (rotation, translation, oscillations...).

An everyday analogy may help to clear up this phenomena. Think of matches in a matchbox as molecules in a molecular crystal. With a gentle movement of the box (temperature increase) the matches "flow" keeping a preferred average direction. They are able to move but they maintain a certain degree of anisotropy. Destroying the orientational order of the matches completely is not an easy task, and requires much more shaking, so we can conclude that the state is stable in a certain "shaking" (temperature) range. Maybe it is better to stop before pushing the matchbox analogy too far, and just pick up the fact that the liquid crystal state is something surprising but, somehow, to be expected.

Liquid crystal phases (a.k.a. mesophases) brought by purely thermal processes are labeled as *thermotropic* and we will be dealing with this kind in what follows. However, it is worth mentioning that other type, known as *lyotropic* liquid crystals, exists. In this case, some amphiphilic compounds show mesomorphism as a function of concentration, when mixed with certain solvents.

The thermotropic liquid crystals are, in their turn, classified depending on the molecular shape. During the years, apart from the initial simplest rod-like (calamitic) molecules, mesophases with molecules shaped as, for instance, discs [13], boards [14], hockey-sticks [15], bananas [4], Hs [16] or Ks [17] have been found . This thesis is mainly focused on the study of bent-core liquid crystals (commonly known as bananas), but, to introduce some generalities, calamitics will be used due to their simplicity.

Calamitic liquid crystals.

A calamitic mesogen is shown in Fig. 1. A long aromatic rigid core is functionalized with one or two flexible alkyl tails, whose mobility will try to avoid crystallization.

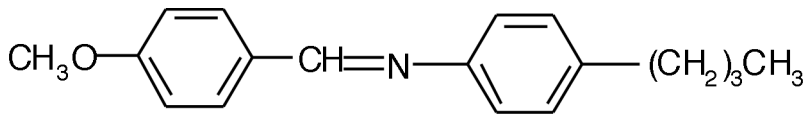

Fig. 1: Molecular structure of a typical calamitic mesogen (MBBA, phase sequence: Xtal - 22° - N - 47° – Iso).

These simple molecules give rise to a very rich variety of liquid crystal phases. The most typical ones are depicted in Fig. 2. Minimization of the excluded volume will lead to orientational long range order of the rigid cores forming the nematic phase N. In this phase the molecules are free to move, but, on the average, there is a preferred direction for the long molecular axis (a.k.a. molecular director). The chemical incompatibility of aromatic cores and hydrocarbon tails can cause their segregation and, consequently, long range positional order in one (or more) dimensions as in the different smectic phases where the molecules stack into layers: SmA and SmC. The molecules are free to move inside the layers, but changing layers is, somehow, more restricted. Spatial modulation of these layers leads to undulated and columnar phases, commonly encountered in bent-core compounds (see below). Obviously, mesophases (one or more) appear between the solid crystalline (or glassy) state and the isotropic liquid.

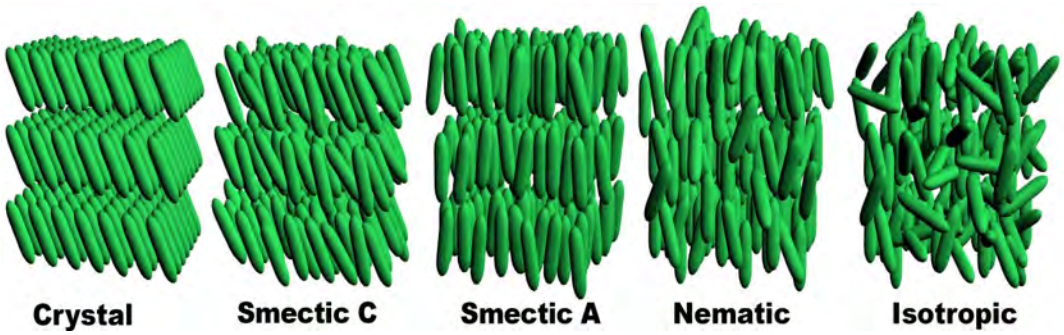

Fig. 2: Typical phase sequence of a mesogenic calamitic compound, from a low temperature crystalline phase (left) to the high temperature isotropic phase (right).

The parallel order of anisotropic molecules gives rise to the anisotropy of macroscopic physical properties. Perhaps the most easily observable one is the optical anisotropy in which the anisotropy of the molecular polarizability causes the optical anisotropy of the liquid crystalline state so that it shows birefringence. How this property is used to extract information about the phases is explained in Chapter 2, when dealing with polarized light microscopy

The structural symmetry of the N and SmA phases results in optical uniaxiality whereby the director is identical to the optic axis. However, in the case of the SmC, biaxiality is allowed by symmetry.

If chirality is introduced in the system (usually via chiral carbons) some new phases appear due to the lower symmetry requirements, the most important ones being the chiral nematic N* (or cholesteric) phase and the chiral SmC* (see Fig. 3). A helical structure is present in both and gives the material the ability to rotate the direction of the polarization of the light (see Chapter 5).

It was Meyer *et al.* in 1975 [18] who realized that the lower symmetry of the SmC* allowed the existence of spontaneous polarization in the direction perpendicular to the

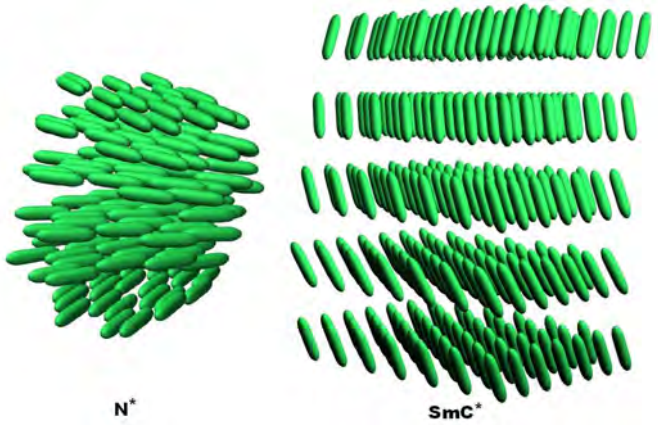

Fig. 3: N and SmC* phases of calamitic liquid crystals. In the N* phase the molecules describe an helix with the axis perpendicular to the molecular director. In the SmC* phase it is the tilt direction what describes an helix, changing from layer to layer.*

tilt plane. Due to the helix, this direction changes from layer to layer and there is no macroscopic polarization. Consequently, the SmC* is helielectric instead of ferroelectric, however the adjective ferroelectric is normally used. The helix can be unwound with an electric field (see Fig. 4)

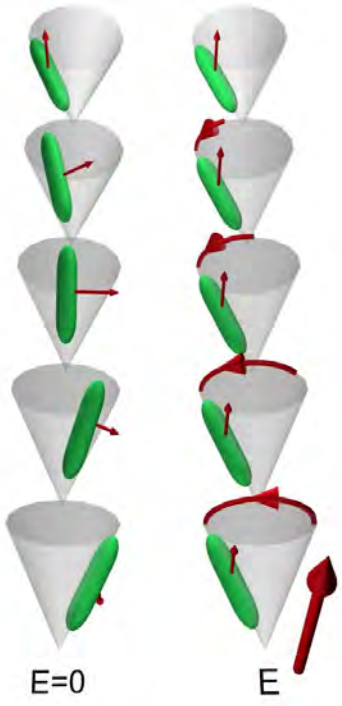

Fig. 4: Half of SmC pitch is sketched. The molecules describe a helix in which the dipoles (small red arrows in the figure) cancel on the average (left side). An electric field induces a collective motion of the molecules around the cone and the helix is unwound giving rise to a ferroelectric state (right side).*

Bent-core liquid crystals

Until the work of Niori *et al.* in 1996 [19] polar phases were unequivocally linked with chiral molecules, but the authors showed that banana shaped (bent-core) molecules boast polar ordered mesophases despite being achiral. This was the dawn of the bent-core liquid crystal field which is the main subject of this thesis.

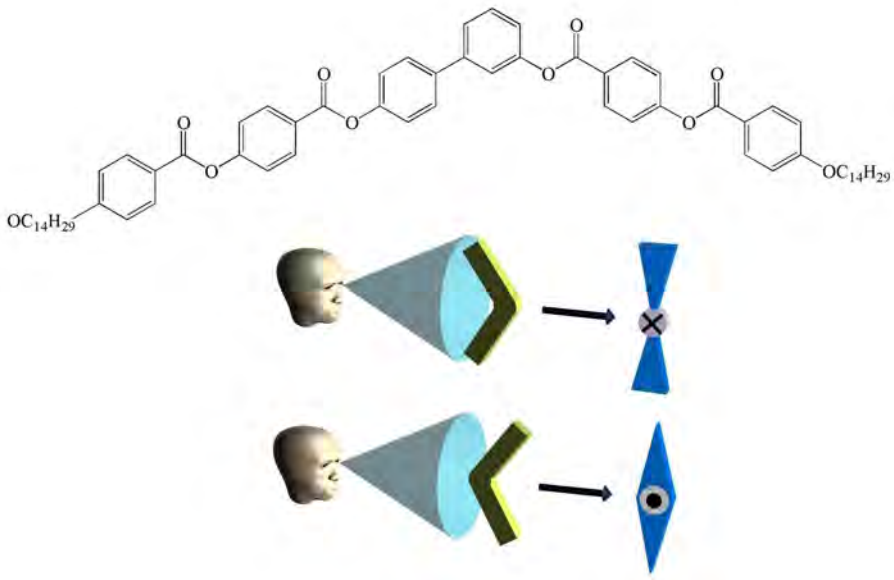

Fig. 5: Molecular structure of a typical bent-core mesogen (phase sequence: Xtal – 67.7º - SmCP – 156.5º – Iso) and diagram of how bent-core molecules are represented depending on the point of view. The cross and dot in the icons represent the bent directions (and logically the dipoles). The colors (red and blue in this work) represent the layer chirality (when present).

A typical bent-core mesogenic molecule is shown in Fig. 5. This apparently naive structural modification of a rod-like molecule gives rise to some radically new mesophases which were initially denominated as B phases and numbered chronologically (B1, B2, B3, etc.) [4]. It has been seen afterwards that some of these B phases were, in fact, grouping a wider range of structures and this terminology has ended up being ambiguous and will be avoided in this thesis when confusion is possible.

The appearance of new mesophases in bent-core materials is due to two reasons:

- The bent shape hinders the rotation around the molecular director (the string of the bow) and, to minimize the excluded volume, molecules tend to stack in a smectic fashion with parallel bent directions, which coincides with the molecular dipole.

- If the molecules tilt within the layers, the mirror symmetry is broken and opposite tilts give rise to opposite layer chiralities (see Fig. 6) [20]. In this way, a structure composed of achiral molecules becomes chiral.

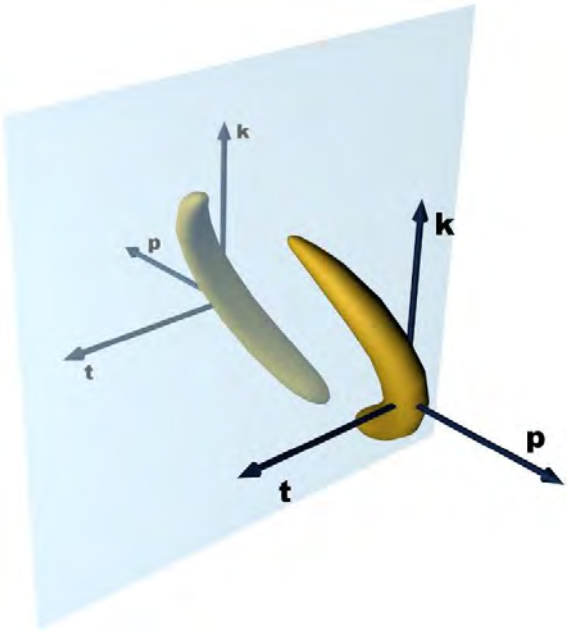

Fig. 6: When two layers have tilts in opposite directions they become two unmatchable mirror images. The trihedron formed by the tilt direction t, dipole moment p and layer normal k is not superimposable on its specular image by simple translations or rotations and the structure is chiral.

As mentioned above, quite a few B phases have been proposed but the structures have not been completely characterized. This thesis is focused on SmCP phases (B2), layer modulated phases (including the B1 and B7 families) and the soft crystalline B4 phase. Since it is not the aim of this introduction to give a deep review on the bent-core liquid crystal phases, only the mentioned ones will be shortly developed below. The structure of the B4 phase will be revised in this work and it will be described in detail in Chapter 5.

For the reader interested in more details, we refer to above-mentioned relatively recent reviews on the specific subject of bent-core liquid crystals. In [4] a enlightening description of the banana phases can be found. Another extensive review is [3] which possesses a special focus on structure-property relationships and chirality related phenomena. In [5] some functionalities of these materials are summarized.

SmCP phases

The SmCP phases gather both components that made bent-core molecules receive so much attention: polarity and chirality. In these phases the molecules are arranged in layers with a non-null tilt angle. Depending on the orientation of the tilt and molecular dipole directions in adjacent layers there are four (basic) SmCP phases: $SmC_{A,S}P_{A,F}$ (see Fig. 7). It is important to note that in this case, unlike the SmC*, the tilt and polarization directions are not correlated.

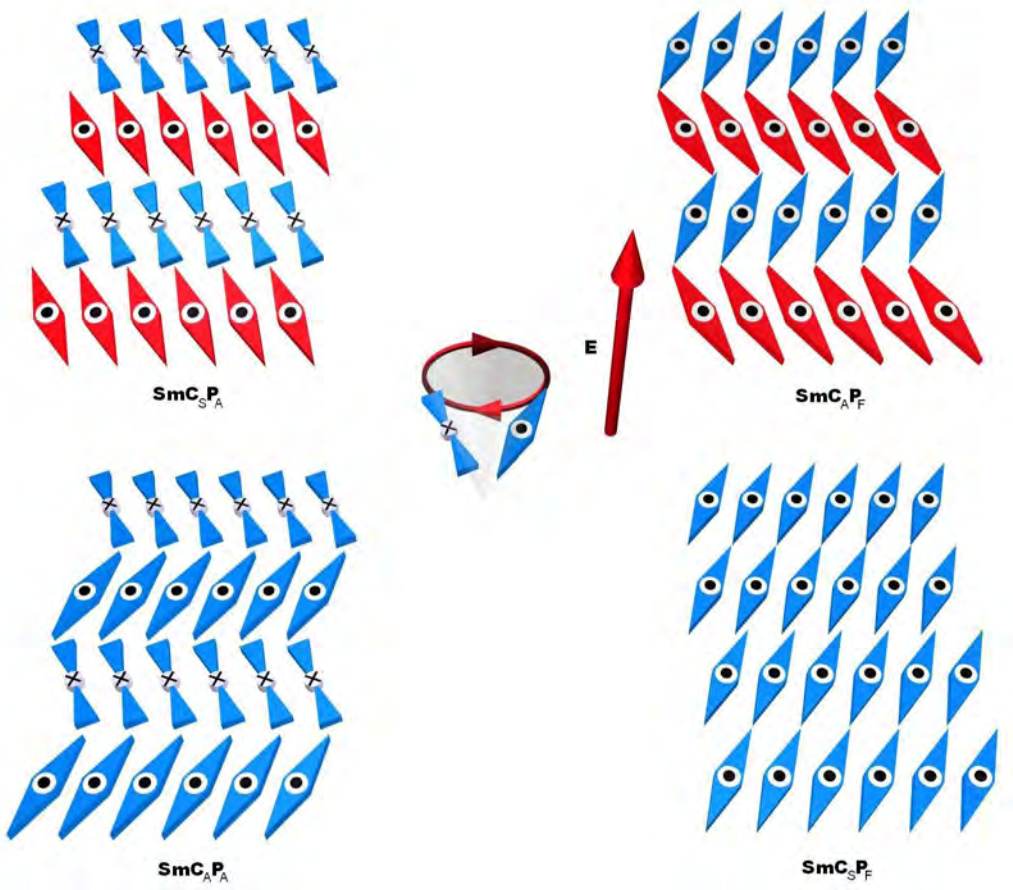

Fig. 7: The four basic SmCP phases. From the point of view of polarity the two structures on the left and the two on the right are anti- and ferroelectric respectively. From the chirality point of view, the two structures at the top are racemic and the two at the bottom homochiral. If the ground state is antiferroelectric and the switching takes place around the cone defined by the tilt and the layer normal (as depicted in the center of the figure), the structures on the left transform into the ones on the right under the application of an electric field.

The layer chirality alters from layer to layer in the SmC_SP_A and SmC_AP_F (racemic) phases. However, the SmC_AP_A and $SmCP_SP_F$ are homochiral, and all the layers posses the same chirality.

If we extend the correlation to more than two layers there are more possible tilt-

polarization combinations [21]. They can be described as a repetition of stacks of the four different basic structures (see above) including information on the interface between stacks. This gives rise to names such as $[SmC_SP_F]_aP_F$ (depicted in Fig. 62 pg. 70).

If we induce a polarization reorientation, the switching can be either along the cone (as depicted in the center of Fig. 7) or along the long molecular axis [22][23]. In the former case the chirality of the layers is kept and can be detected optically (see Fig. 15), while in the latter it is not. What kind of switching occurs depends on factors such as field frequencies and intensity, viscosity, temperature, etc. [24]

Layer modulated phases.

Unlike with classical rod-like molecules, when working with bent-core molecules a wide range of liquid crystal phases with layer modulations are found. These modulations can lead either to the formation of undulated layers (USmCP) or to the breakage of the layers to form columns (Col_x).

The driving force of the modulations seems to be polarization splay [25][26] which appears to avoid net macroscopic polarization. In Fig. 8 a block of bent-core molecules with splayed polarization is shown.

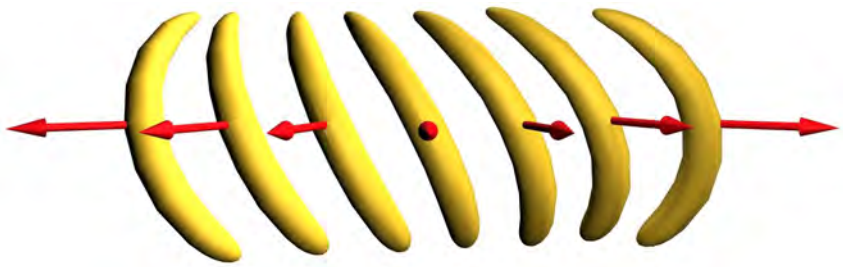

Fig. 8: The polarization splay reduces the net polarization locally. In the image the dipoles points outwards, but the splay can be also opposite with all the dipoles pointing inwards.

The splayed distribution of dipoles inside the layer forces the appearance of defects where the tilt decreases and, consequently, the layer thickness increases. To accommodate these defects the smectic planes undulate (see Fig. 9) giving rise to the USmCP phases [25].

When the layers break completely at these defects, a 2D array of columns is formed of the layer fragments. In this case, there are several possibilities depending on the tilt of the molecules. If the molecules are not tilted a rectangular lattice with an antiferroelectric arrangement of neighboring columns arise: Col_r phase. The polarization can be in the plane of the lattice (B1) or perpendicular to the plane of the lattice ($B1_{rev}$). When the molecules are tilted the lattice is oblique and is called $B1_{revTilted}$.

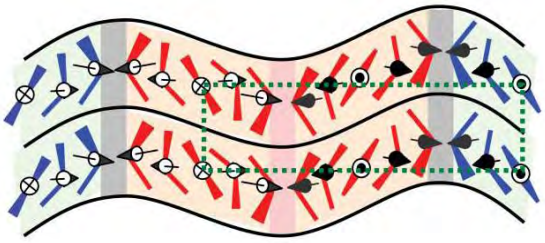

Fig. 9: Undulation of the smectic planes to best accommodate polarization splay. In this example the tilt changes at the defects. Reprinted from Ref. [3]

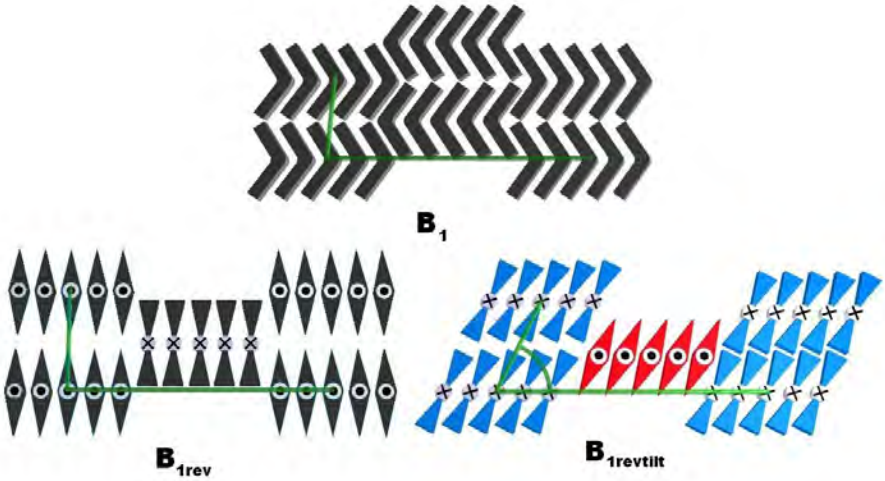

Fig. 10: The three most common columnar mesophases and their respective unit cells.

These phases are depicted in Fig. 10 and a reexamination will be carried out in Chapter 4 on the basis of X-ray diffraction measurements on aligned samples.

Modulated phases are sometimes switchable and cases in which the electric field induces a phase transition to an SmCP are found in the literature [27][28][29][30][31]. Gorecka *et al.* suggested that the type of switching (along the cone or along the molecular long axis) depends on the cross section of the columns [32].

It is worth mentioning that there are more general columnar structures in which the blocks are tilted with respect to the lattice axis [33]. Depending on this tilt, the structure is more or less lamellar and one can go continuously from a columnar to an undulated (or purely lamellar phase) just varying the orientation of the constituent blocks. This picture facilitates the understanding of the common origin of these frustrated phases.

Even more general structures have been proposed, adding smaller connecting blocks [33] or bilayer structures [34]. As can be seen, the variety of columnar phases is rather broad and is, definitely, not a closed group yet.

Chapter 2

Experimental techniques

Electro-optical study of liquid crystals

The electro-optical study is the most used tool in a liquid crystal laboratory. The basics are simple, but a thoroughly carried out electro-optical study could really be all that is needed to characterize many liquid crystal materials, leaving other techniques only for confirmation or study of peculiar properties.

Typically, after the synthesis of a mesogen, and probably a differential scanning calorimetry (DSC) study, the prelimilary characterization is done by polarized light optical microscopy. For the electro-optical study of liquid crystals, the samples are usually sandwiched between two glass slides which conform a cell where the material is confined. If the glasses are not fixed to one another, then, in the mesophase, these glasses can glide, which is the strongest confirmation of liquid crystallinity. However, as will be seen, usually these cells must have a fixed thickness or be treated in some way. Also, other confining techniques such as free standing films, thin films or fibers can be employed, but cells are the most commonly used.

In this thesis two kinds of cells have been used:

- **Commercial cells**: This type of cell usually has a surface treatment on the inner side of the glasses to favor a certain alignment of the material (planar or homeotropic). These treatments consist in the deposition of an aligning agent (e.g. lecitines or rubbed polimides). However, unfortunately, they are not as effective with bent-core materials as they are with calamitics. Apart from this, also a thin layer of indium tin oxide (ITO) is usually deposited on both glasses to apply electric fields through the material which could also help to obtain a planar alignment. In our lab, we normally use cells manufactured by Linkam™ with a nominal thickness of 5 μm. Exceptionally, we have used 2, 5 and 10 μm cells by EHC .
- **Home-made cells**: The complexity of bent-core liquid crystals and the use of certain

experimental techniques force the use of non-commercial cells. What lead us to build these cells is the necessity of very specific thicknesses or the application of an electric field in the plane of the glasses to obtain homeotropic alignment.

For their fabrication we start from a glass with a predeposited ITO layer on one of its faces. If we want to apply a field in the plane of the cell, we make use of wet photolithography to disconnect two zones of ITO (which will serve as electrodes) by a fixed separation. Usually, this gap lies in the 50 to 100 μm range. Next, we proceed to glue this ITO covered glass with other with no ITO on it. To do this and control the cell thickness at the same time, we use a UV light curing glue with spacers (glass spheres) of appropriate size dissolved in it. For an sketch of these cells see Fig. 11.

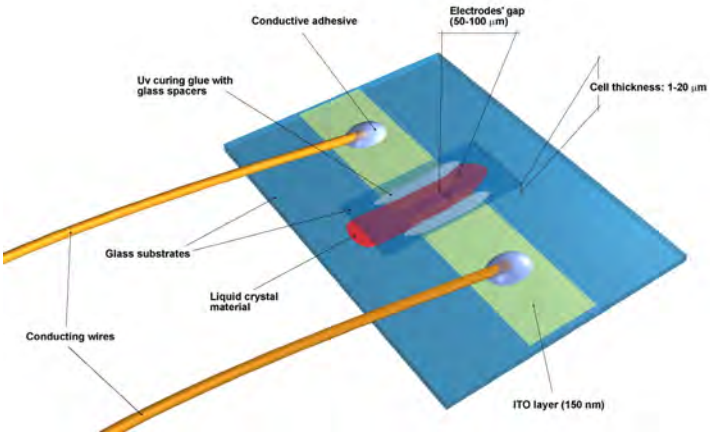

Fig. 11: Scheme of homemade cells used for optical measurements with in-plane electrodes.

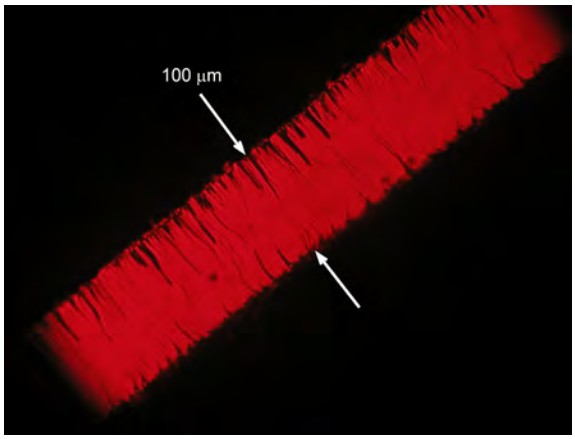

Fig. 12: Liquid crystal material aligned in a homemade cell under an electric field.

The strong structural anisotropy, characteristic of the molecules forming liquid crystal phases, and of the structures in themselves give rise to macroscopic optical anisotropy that is studied with the above mentioned polarized light optical microscope. This microscope is an adaptation of a regular microscope in which two lineal polarizers (one before, and the other after the sample) and a rotating stage have been added (Fig. 13)

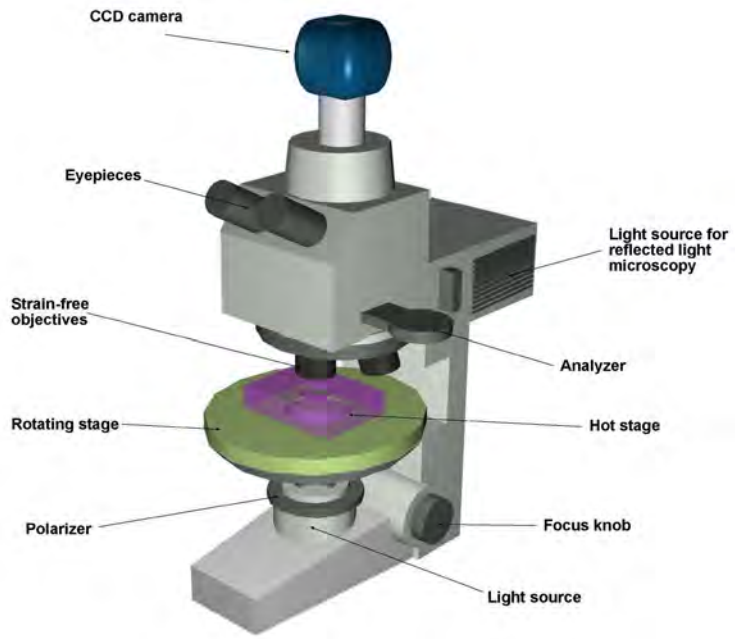

Fig. 13: Sketch of a polarized light microscope.

It is the optical anisotropy what changes the polarization state of the light passing through the sample. The retardation depends on the sample thickness L and material birefringence Δn, that is defined as the difference between the principal optical axes of a sample in a given direction. Since the polarizers in the microscope are usually with their axes perpendicular to each other, the intensity of a light wave with a wavelength λ and initial intensity I_0 is:

$$I = I_0 \sin^2(2\phi) \sin^2\left(\frac{\pi \Delta n L}{\lambda}\right)$$

where ϕ is the angle comprised between the polarizer and fast axis of the sample, Δn the birefringence and L the sample thickness. The intensity is null if $\Delta n = 0$, such as in optically isotropic samples (amorphous materials, cubic phases, …) or if the sample is oriented so that light travels along an optic axis. Also, in the case of one principal axis being parallel to either the polarizer or analyzer, the transmitted intensity will be null. This intensity depends on the thickness and wavelength, therefore if we use white light, interference colors will appear. If the sample is a monodomain, the texture (image seen through the microscope) will be uniform. However, in more disordered

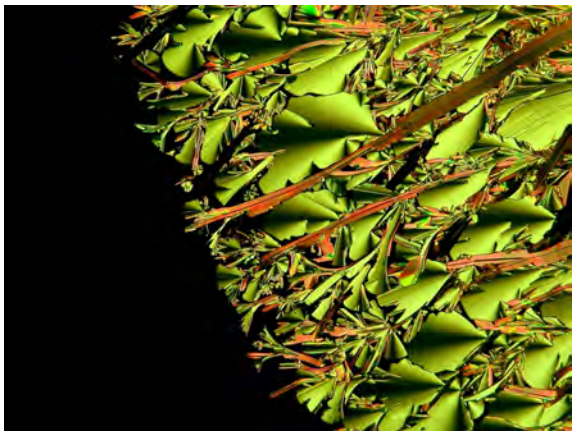

Fig. 14: Texture of a liquid crystal. The material on the left is still in the isotropic phase, so it is dark when seen through crossed polarizers. The right hand side shows a typical texture of a columnar mesophase.

samples, these effects vary from point to point, giving rise to more complex textures (see, for instance, Fig. 14).

The analysis of textures is a powerful and "simple" tool to extract precious information about a given material. Just by looking at texture changes with temperature, phase transitions can be detected. The different phases have quite distinct typical textures which a trained eye can easily discern (see, for instance, [35]). Upon application of an electric field, the switchability of the phase can be confirmed (although some types of switching are not detectable with this technique), and its polar properties deduced (see, for example, Fig. 15). If domains of fair size nucleate, tilt angle and birefringence measurements can also be performed.

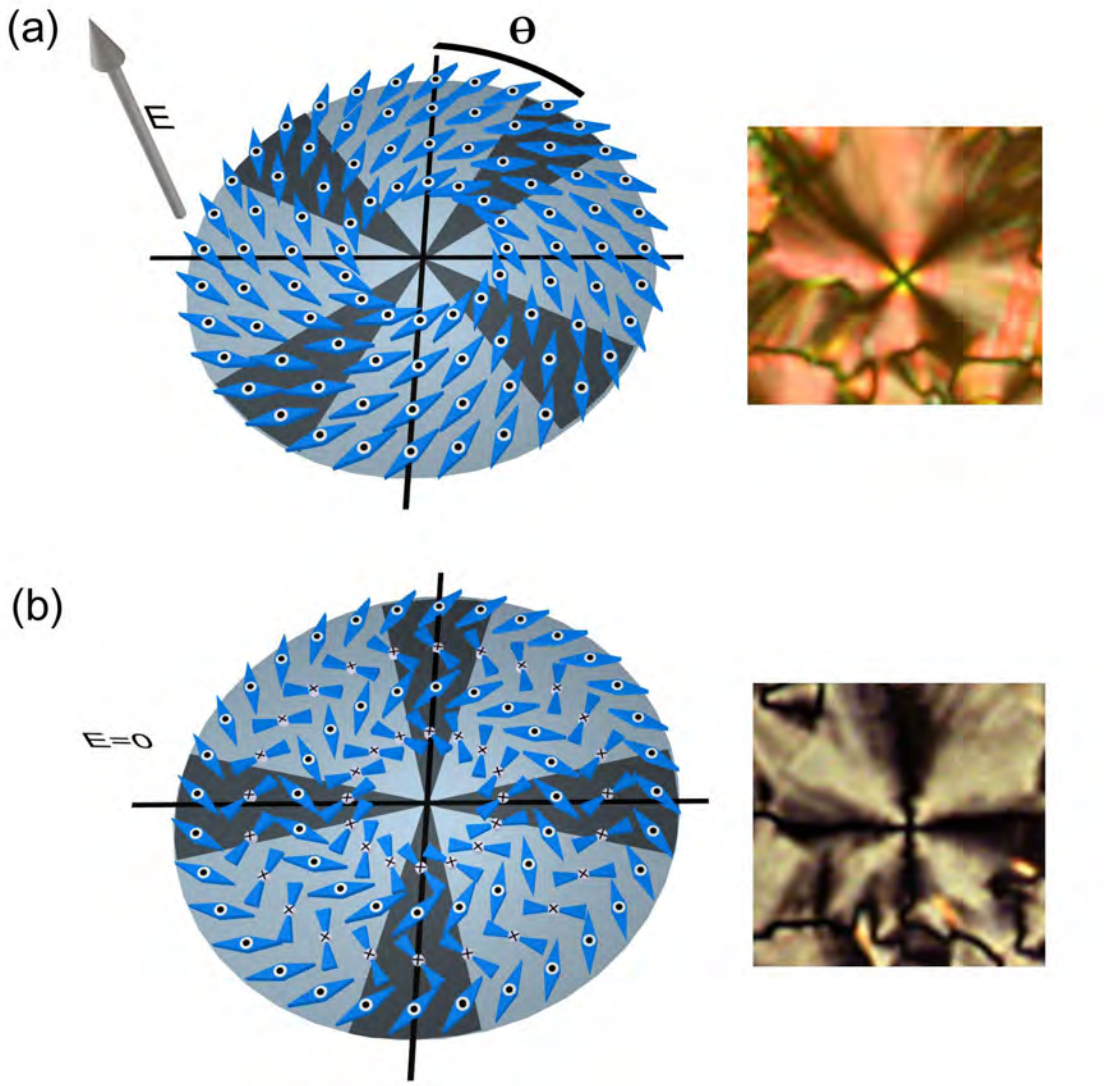

Fig. 15: Electrical switching of an homochiral circular domain. (a) Under an electric field, the synclinic order of the SmC_SP_F phase makes the extinction brushes be at an angle θ (which corresponds to the tilt angle of the molecules in the layers) with respect to the polarizers directions. (b) With the field off, the SmC_AP_A phase gives extinctions parallel to the polarizers. When the field is directed in the opposite direction of that in (a) the tilt is also opposite, and if the tilt is close to 45° (as is this case) the texture is practically indistinguishable.

X-ray diffraction

X-ray diffraction is a fundamental technique in the determination of crystalline structures and it is equally applicable and useful with a liquid crystal material. From a correct interpretation of diffraction diagrams, the arrangement of the molecules in the phase (or mesophase) can be obtained. Of course, changes in the diagram with varying temperature (or concentration) are interpreted as structural phase transitions.

The scattering of X-rays by an ordered material takes place along given directions of

space because of interference phenomena stemming from the lattice periodicities. This directions are given by the Bragg's Law:

$$2d\sin(\theta_m) = m\lambda \quad (1)$$

where d is the distance between atomic planes, θ_m is the diffraction angle, m an integer and λ the X-ray wavelength.

X-ray diffraction diagrams by liquid crystal phases show clear differences with those of crystalline solids. First, "elongated" mesogenic molecules give rise to larger periodicities and therefore peaks at smaller angles will appear (see eq. 1). The degree of order in liquid crystals is lower than in solids because molecules have a certain freedom (fluidity) to wander around resulting in wider diffraction peaks and less higher-order harmonics. This freedom also results in the most distinctive feature of a liquid crystal in an X-ray diffraction diagram: a broad diffuse peak at large angles (see Fig. 16).

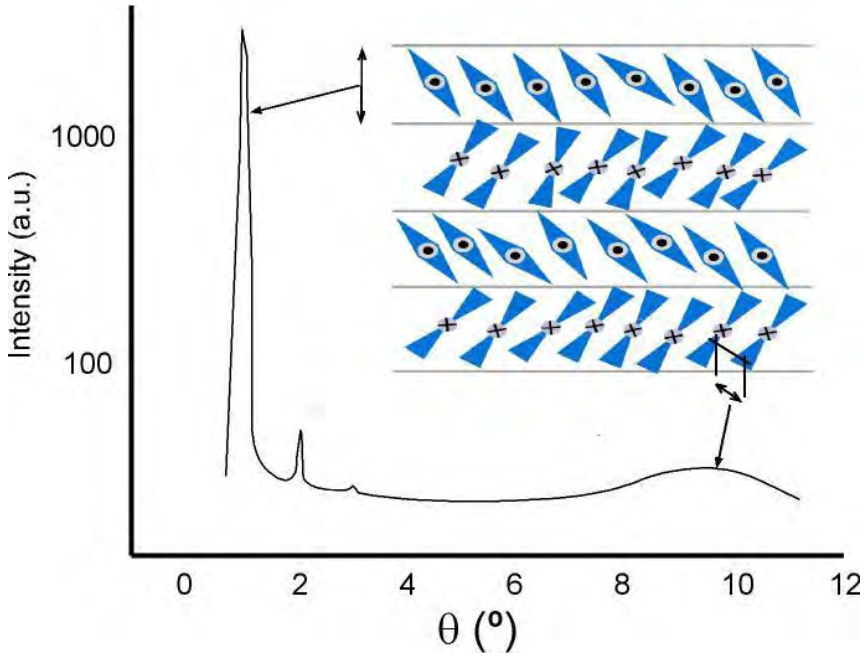

Fig. 16: X-ray diffraction pattern of a liquid crystal smectic phase. The phase depicted to enlighten the periodicities is a SmC_AP_A phase, but the diagram is general for any smectic phase without in-plane order. The sharpness of the layers fixes the number of observable harmonics.

Electronic density distribution

Information on the electronic density distribution can also be extracted from an X-ray diffraction diagram. The method is standard in the crystallography of solids and has been used in 2D (e.g. [30][33]) and 3D [36] liquid crystal phases.

The periodic electron density $\rho(x, y)$ can be expanded in terms of the (hk) Fourier components with amplitudes given by the complex structure factor $F(hk)$ [30]:

$$\rho(x, y)=\frac{F(00)}{A}+\frac{1}{A}\sum_{hk} \pm\left|F(hk)\right|\cos\left[2\pi(hx+ky)\right] \qquad (2)$$

where A is the area of the unit cell. In the above expression we have assumed that $\rho(x, y)=\rho(-x,-y)$ for an appropriate cell origin. It can be shown that this can be done for practically the whole set of structural models proposed up to now for the type of liquid crystals we deal with in this work. Under this condition the structure factor not only follows the relationship $F^{*}(h\,k)=F(\overline{h}\,\overline{k})$, which always holds, but it also real and, therefore $F(h\,k)=F(\overline{h}\,\overline{k})$. The quantities $\left|F(hk)\right|$ are related to the *hk* reflection intensities as $I(hk)=\left|F(hk)\right|^2$. The intensities $I(hk)$ are obtained from the X-ray diffraction peaks after background subtraction, taking into account the Lorentz and polarization corrections and the multiplicity of each reflection. The uncertainty left by the possible sign combinations is overcome by analyzing the plausibility of the electron density maps obtained for each one.

Once the electron density map is determined, the molecular cores are positioned on the maximum density regions of the map in order to pack and fill the volume as well as possible. This is done in agreement with previous experimental information (for example: anti- or ferroelectricity; or anti- or synclinicity) and attending to packing conditions, molecular size, and optimization of steric interactions.)

Experimental setup

In our lab, X-ray measurements are carried out in non-oriented samples (powder diffraction), what makes peaks circles due to the random orientation of domains. We have a small-angle goniometer equipped with a high-temperature stage and a linear position-sensitive detector (PSD) with 4° of angular range, where the main reflections occur in liquid crystals. In order to check the liquid crystalline character of the phases (i.e. see the broad diffuse peak), we employ a wide-angle goniometer of similar features. Monochromatic Cu K_{α} radiation is used (λ=1.5406 Å) and the materials are introduced in the isotropic phase into Lindemann capillaries with 0.5 mm diameter.

During the realization of this thesis I had the opportunity to work with the group lead by Ewa Gorecka and Damian Pociecha in the University of Warsaw and use their X-ray diffractometers. They have a really good facility and I was able to perform measurements on aligned samples. I used mainly the SAXS (Small Angle X-Ray Scattering) Brucker Nanostar system shown in Fig. 17 using CuK_{α} radiation. The 2D real-time position-sensitive detector allows for an easy interpretation of the patterns.

To obtain aligned samples, drops of material (which can be considered as thin films)

were deposited on mica substrates and expected to align due to surface tension when entering the mesophase from the isotropic phase. The quality of the alignment depends strongly on the material, cooling rate, drop size and proximity to the surface of the X-ray spot (~100 μm^2) on the sample. If the alignment obtained is good enough a direct image of the reciprocal lattice is observed (see, for instance, Fig. 39c in pg. 44). It is noteworthy to mention that due to the nature of the drop, there is a symmetry revolution axis perpendicular to the surface, which derives in a two-fold axis in the X-ray diagram about the vertical direction. Also due to this preferred direction, peaks diffracted in the direction parallel to the surface are more intense than they should be in relation to the rest. This is why, to extract the intensity of the peaks for the calculation of the electronic density distribution, powder samples must be used.

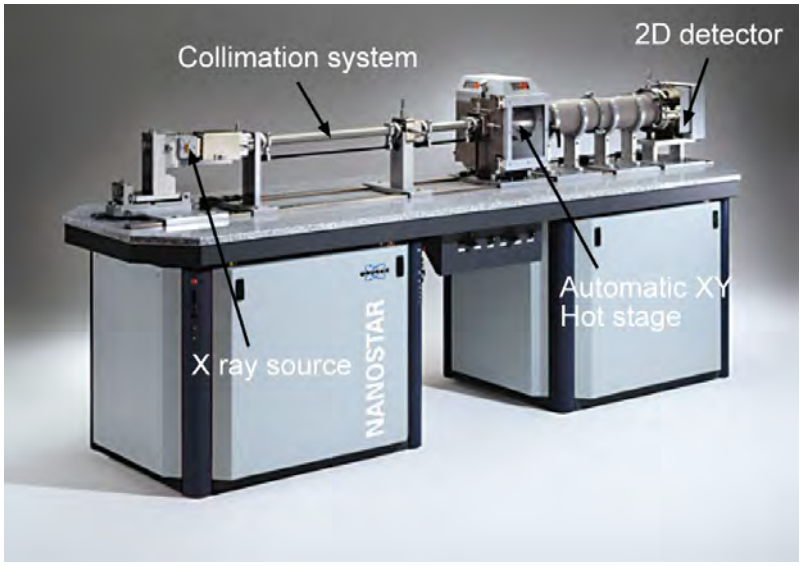

Fig. 17: SAXS Brucker Nanostar System.

Second Harmonic Generation.

The emission of a photon of frequency 2ω in a material via the absorption of two photons of frequency ω is a non-linear optical (NLO) process called second harmonic generation (from now on SHG). It is nonlinear because it can only be explained if terms containing higher order powers of *E* in the expansion of the induced polarization *P* are included:

$$P_i = \overbrace{\varepsilon_0 \chi_{ij}^{(1)} E_j(t)}^{linear\ optics} + \overbrace{\chi_{ijk}^{(2)} E_j(t) E_k(t) + \ldots}^{nonlinear\ optics}$$

where ε_0 is the electric permitivity of vacumm, $\chi^{(1)}$ the linear susceptibility tensor, $\boldsymbol{E}$ the electric field and $\chi^{(2)}$ the second order dielectric susceptibility tensor. If an electric field oscillates at a frequency ω ($\boldsymbol{E} \propto e^{-i\omega t}$), the second order nonlinear term can give

rise to a component of the polarization oscillating at a frequency 2ω ($\boldsymbol{E} \propto e^{-i2\omega t}$), which is the SHG signal.

Because a reversal of the electric field $\boldsymbol{E}$ must cause a reversal in the sign of $\boldsymbol{P}$, it is easily proved that second order effects are not present in materials with inversion symmetry. If the material is transparent over the frequencies of interest, we can assume that the susceptibility is independent of the frequency. Also, since the exchange of E_j and E_k has no physical implications, we can replace the subscripts kj by a single subscript following the contraction used for the piezoelectric coefficients. If we call $\chi_{ij}^{(2)} = 2 d_{ij}$ (where i ranges from 1 to 3, and j from 1 to 6) we can write the usual matrix relation for the second order induced polarization:

$$\begin{pmatrix} P_x^{NL} \\ P_y^{NL} \\ P_z^{NL} \end{pmatrix} = \begin{pmatrix} d_{11} & d_{12} & d_{13} & d_{14} & d_{15} & d_{16} \\ d_{21} & d_{22} & d_{23} & d_{24} & d_{25} & d_{26} \\ d_{31} & d_{32} & d_{33} & d_{34} & d_{35} & d_{36} \end{pmatrix} \begin{pmatrix} E_x^2 \\ E_y^2 \\ E_z^2 \\ 2E_yE_z \\ 2E_xE_z \\ 2E_xE_y \end{pmatrix}$$

Given the point-group symmetry of the material, this contracted tensor can be further simplified leaving a reduced number of different components [6]. If the case applies, the Kleinman's conditions can also be used to have even less components [6].

To obtain an expression for the SHG power $P^{2\omega}$ generated by a sample with nonlinear coefficients d_{ij}, the Maxwell's equations must be solved including the nonlinear polarization (see, for example, [6]). The result is the following:

$$P^{2\omega} = 8\left(\frac{\mu_0}{\varepsilon_0}\right)^{3/2} \frac{\omega^2 d_{eff}^2 L^2}{n^3} \frac{(P^{\omega})^2}{Area} \frac{\sin^2\left(\frac{\Delta k L}{2}\right)}{(\Delta k L/2)^2} \cdot T_{tot} \qquad (3)$$

where d_{eff}, a linear combination of d_{ij}, is the effective nonlinear coefficient taking part in a given experimental geometry determined by the polarizers and sample orientation, L is the sample thickness, $\Delta k = k_2 - 2k_1$ is the phase mismatch between the fundamental and SH wave, and T_{tot} is a factor accounting for all the applicable Fresnel coefficients of the experiment.

There are two unknown quantities in equation (3): d_{eff} and Δk. To obtain both of them, measurements using two (or more) cells with different thicknesses are carried out, and a simultaneous fitting is made. By changing the direction of the polarizer or analyzer, or using different sample orientations, we can measure different d_{eff} (in general, a combination of d_{ij}s) and characterize the d tensor completely [37].

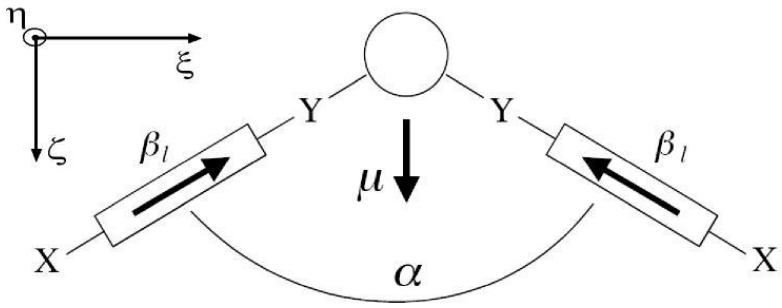

Fig. 18: Sketch of the structure of a bent-core molecule. X and Y represent donor and acceptor groups respectively. The molecular hyperpolarizability tensor β can be considered to arise from a unique one-dimensional hyperpolarizability β_l directed longitudinally along the wings of the molecule.

Araoka *et al.* [38][39] proposed a model for the hyperpolarizability of bent-core liquid crystals accounting for the C_{2v} molecular symmetry (even in asymmetric compounds the head-tail invariance makes this argument valid) and approximating the molecules as planar. Doing so the molecular hyperpolarizability tensor results in:

$$\beta = \begin{pmatrix} 0 & 0 & 0 & 0 & \beta_{\zeta\xi\xi} & 0 \\ 0 & 0 & 0 & 0 & 0 & 0 \\ \beta_{\zeta\xi\xi} & 0 & \beta_{\zeta\zeta\zeta} & 0 & 0 & 0 \end{pmatrix} \tag{4}$$

in the molecular reference frame of Fig. 18.

In this model, the macroscopic second order susceptibility tensor will only have three independent coefficients, namely $D = Nf^3 \langle \cos\Psi \rangle \beta_{\zeta\xi\xi}$, $D' = Nf^3 \langle \cos\Psi \sin^2\Psi \rangle \beta_{\zeta\zeta\zeta}$ and $d = Nf^3 \langle \cos^3\Psi \rangle \beta_{\zeta\zeta\zeta}$. Here, N is the density of molecules, f the local field factor and Ψ the angle between the macroscopic polarization and the molecular dipole moment (the brackets denote thermal average). For example, in the case of a SmC_SP_F phase the resulting **d** tensor is:

$$d = \begin{pmatrix} 0 & 0 & 0 & (D+D')\sin\theta\cos\theta & 0 & D\sin^2\theta + D'\cos^2\theta \\ D\sin^2\theta + D'\cos^2\theta & d & D\cos^2\theta + D'\sin^2\theta & 0 & (D+D')\sin\theta\cos\theta & 0 \\ 0 & 0 & 0 & D\cos^2\theta + D'\sin^2\theta & 0 & (D+D')\sin\theta\cos\theta \end{pmatrix}$$

where we chose the frame of reference so that x is along the projection of the molecule on the smectic plane, y along the bend direction and z, consequently, along the layer normal.

If perfect molecular order is assumed (so that $\Psi=0$ and the thermal averages are equal to 1 or 0) further simplification is achieved. In this context, $D' = 0$ and the two remaining coefficients are related to each other via the bending angle α:

$$\frac{D}{d}=\tan^2\left(\frac{\alpha}{2}\right) \tag{5}$$

where it has also been assumed that the molecular hyperpolarizability is mainly due to β_l, the longitudinal hyperpolarizability along the molecular wings (see Fig. 18). This assumption results in $\beta_{\zeta\xi\xi}=2\beta_l\cos\frac{\alpha}{2}\cdot\sin^2\frac{\alpha}{2}$ and $\beta_{\zeta\zeta\zeta}=2\beta_l\cos^3\frac{\alpha}{2}$.

The nonlinear tensor for the SmCP is easily obtained by means of rotating and averaging (if the layers are not identical) the molecular hyperpolarizability tensor. It results in:

$$\mathrm{SmC_SP_F}\quad \boldsymbol{d}=\begin{pmatrix} 0 & 0 & 0 & D\sin\theta\cos\theta & 0 & D\sin^2\theta \\ D\sin^2\theta & d & D\cos^2\theta & 0 & D\sin\theta\cos\theta & 0 \\ 0 & 0 & 0 & D\cos^2\theta & 0 & D\sin\theta\cos\theta \end{pmatrix} \tag{6}$$

$$\mathrm{SmC_AP_A}\quad \boldsymbol{d}=\begin{pmatrix} 0 & 0 & 0 & D\sin\theta\cos\theta & 0 & 0 \\ 0 & 0 & 0 & 0 & D\sin\theta\cos\theta & 0 \\ 0 & 0 & 0 & 0 & 0 & D\sin\theta\cos\theta \end{pmatrix}$$

$$\mathrm{SmC_AP_F}\quad \boldsymbol{d}=\begin{pmatrix} 0 & 0 & 0 & 0 & 0 & D\sin^2\theta \\ D\sin^2\theta & d & D\cos^2\theta & 0 & 0 & 0 \\ 0 & 0 & 0 & D\cos^2\theta & 0 & 0 \end{pmatrix} \tag{7}$$

$$\mathrm{SmC_SP_A}\quad \boldsymbol{d}=0$$

SHG measurements are usually performed in the ferroelectric phases. If the polarization of the light is parallel to the field direction, it is called p-light, and if it is perpendicular s-light. Then, measuring in the p-p configuration of the light polarization (the first p for the incident light and the second one for the measured one) we get $d_{\text{p-p}}=d_{22}$ and for s-p $d_{\text{s-p}}=d_{12}$, from where we can extract information on both coefficients (D and d).

SHG experimental setup I

The experimental setup is standard. A Q-switched Nd:YAG laser shooting 6 ns pulses at a 5 Hz frequency acts a the fundamental wave source. The trigger of the laser source is in synchrony with the electric field on the sample, which is placed in a rotable Instec™ hot-stage. Care must be taken with the laser intensity so that the sample is not damaged; in our case the peak intensity at the sample is estimated to be around 1 $\mathrm{MWcm^{-2}}$. Linear polarizers control the polarization of the incident light as well as of the SH wave. As sketch of the apparatus on the optical bench is depicted in Fig. 19.

Due to the difficulty to obtain an accurate value of many of the quantities in eq. 3, and for simplicity, we usually compare the SHG power of the LC sample with that of a material with a know nonlinear coefficient to obtain an absolute value of d_{eff} for the LC

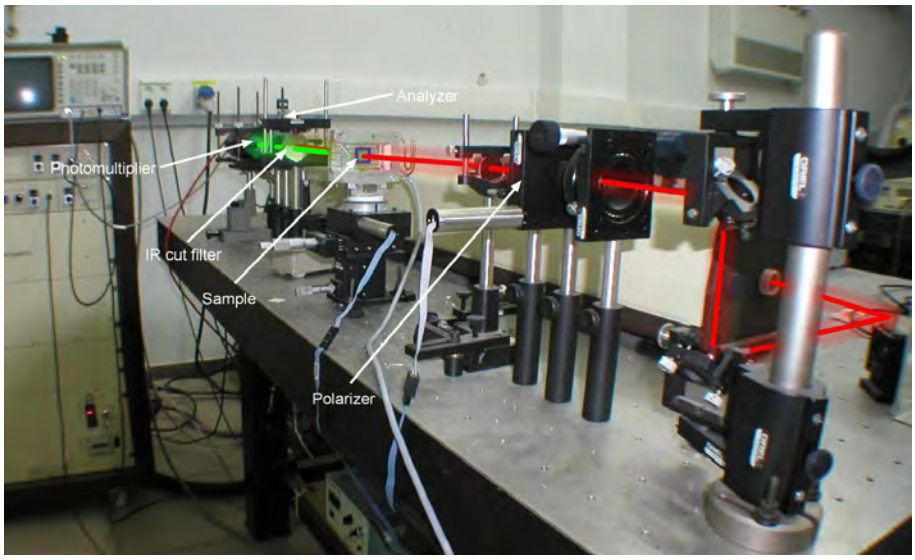

Fig. 19: SHG bench working at 1064 nm. The light from the Nd:YAG is linearly polarized and a quarter wave plate is placed before the polarizer to ensure that we can rotate it without changing the intensity of the light hitting the sample. Also a filter cutting visible light is present to remove non-desired radiation from the lamps of the laser source.

material. d_{eff} is 0.4 pmV^{-1} for quartz when its optic axis is on the plane of incidence and both the incident and collect light are polarized parallel to it.

SHG experimental setup II

If the sample is non-transparent resonance effects appear and eq. (3) is not valid. The formulas to deal with that situation were derived by Herman and Hayden [40] and are more complex. They will be presented in Chapter 3.

To get rid of these resonance effects we made use of the Laser Facility in our University and set up another SHG bench working at a wavelength high enough to avoid absorption bandsa at the generated wavelength (see Fig. 20).

In this case, ultrashort light pulses are generated by a commercial Ti:Sapphire oscillator-regenerative amplifier laser system (Coherent) that provides a 1 kHz train of 40 fs pulses centered at 800 nm. A portion of the amplifier output drives an optical parametric amplifier (OPA) tunable in the 300-2600 nm range (Coherent OPERA).

Due to the position of the absorption bands of the materials measured in this thesis, we usually worked at 1550-1600 nm. At this wavelength the pulse width was estimated to be about 465 cm^{-1} and the duration 40-45 fs. The pulse energy was ca. 10 μJ.

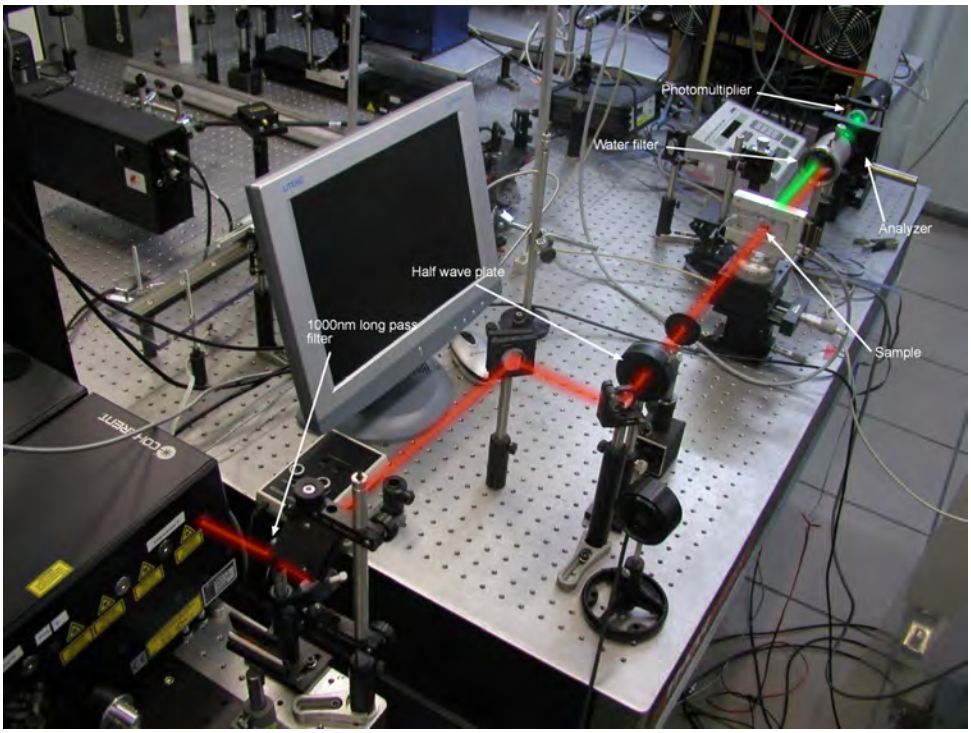

Fig. 20: At the exit of the laser source a 1000 nm long pass filter is present to remove any spurious radiation coming out from processes in the parametric amplification of the beam. The light from the OPA is linearly polarized and a half wave plate is placed to control its polarization angle. After the SHG a water filter gets rid of the fundamental light wavelenght.

Due to the oscillations of the power output of the laser source, a beam splitter redirects part of the light to a BBO (β-BaB_2O_4) crystal and the SHG wave generated by this was collected with a photodiode. This signal is used as reference to correct for the intensity fluctuations.

Chapter 3

Liquid crystal materials for non-linear optics

Second harmonic generation has always been used in our lab as another exploratory tool for the study of liquid crystals, but, during the last few years, to accurately measure and maximize the non-linear optical (NLO) response in this type of materials have become objectives in themselves.

The industry of non-linear optical materials is nowadays almost a monopoly of inorganic compounds and poled polymers, and it will continue to be like that in the near future. However, NLO liquid crystals could improve up to the point where they could become a competitive alternative.

Ultrafast electro-optic modulators are the most direct application of materials with good NLO response. The important material property is described by the electro-optic tensor **r** that relates the birefringence change with the applied field [6]. This is a second order effect (see Chapter 2) mixing a field at a visible frequency and another with much lower frequency (~0). From the experimental point of view, the use of a low frequency field makes it difficult to separate the molecular motion contribution (slow) from those of electronic origin (fast). The latter determines the Pockel's **r** tensor, which is what should be maximized. Out of resonances, it can be shown that the tensor **r** is related to the second order susceptibility tensor d via $r_{ij}=4\pi d_{ij}/n^4$, implying that a good SHG performance of a material derives in a fast electro-optic response. In our lab we thus use SHG characterization to measure the NLO performance of the materials.

Soon after the re-discovery of bent-core liquid crystals in the mid nineties, people realized that they could be really good contenders for applications in NLO [41][42][43], beating the efficiencies of calamitic liquid crystals by far [44]. The first reason of this excitement came from the fact that bent-core polar phases present a large level of stereocontrol, in which often more than 50% of the molecules have their dipoles pointing in the same direction, a percentage that drops to less than 15% in typical

calamitic polar phases. This is due to the fact that bent-core molecules pack more efficiently with their kink (= dipole) directions parallel.

Secondly, the insertion of long bulky highly polarizable units along the polar direction in rod-shaped molecules is in conflict with the calamitic character of the molecule and, therefore, with its mesogenicity. This is a serious limitation that is not present on bent-core compounds (see Fig. 21). Long highly polarizable structures can be inserted in the lateral wings of the bent-core molecule without spoiling their liquid crystalline character. From the practical point of view, this gives more freedom when it comes to designing new materials, and it is the approach that we have used in the search for improved liquid crystal materials for NLO.

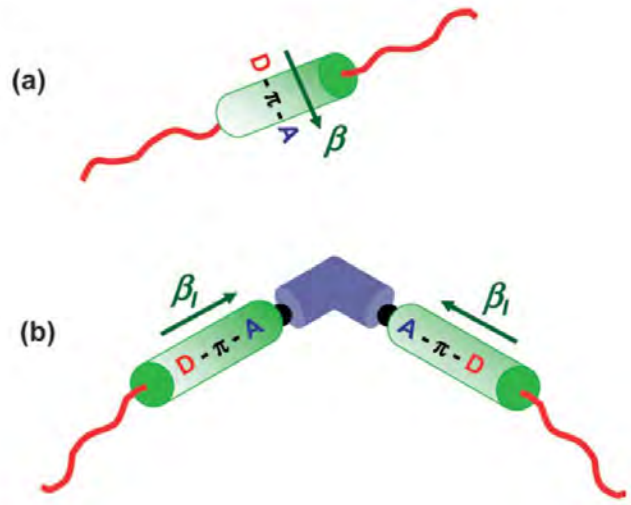

Fig. 21: Sketchs of (a) a rod-like molecule and (b) a bent-core molecule. The main electron donor D and acceptor A groups and their π conjugations are shown, as well as the vector components of the hyperpolarizability tensor β_l.

Before getting down to the study of the compounds, it is worth pointing out that despite references on the subject of NLO characterization of liquid crystal materials are not numerous, big differences are found for the NLO coefficients of the same material depending on the source it is looked up. These discrepancies could be due to different sample preparation or data processing. They are not still completely clear and are still object of debate. See, for instance, refs. [37], [43] and [45].

For reference, Fig. 22 shows the NLO coefficients measured in our lab for several representative bent-core materials. These values were the ones to beat when we started looking for NLO improved molecular structures. We can say that for liquid crystals to be used in real applications, values close or higher to those of the currently used materials should be reached (for example, in $LiNbO_3$ d~30 pmV^{-1}). A target value of r~50 pmV^{-1} has been considered reasonable [46].

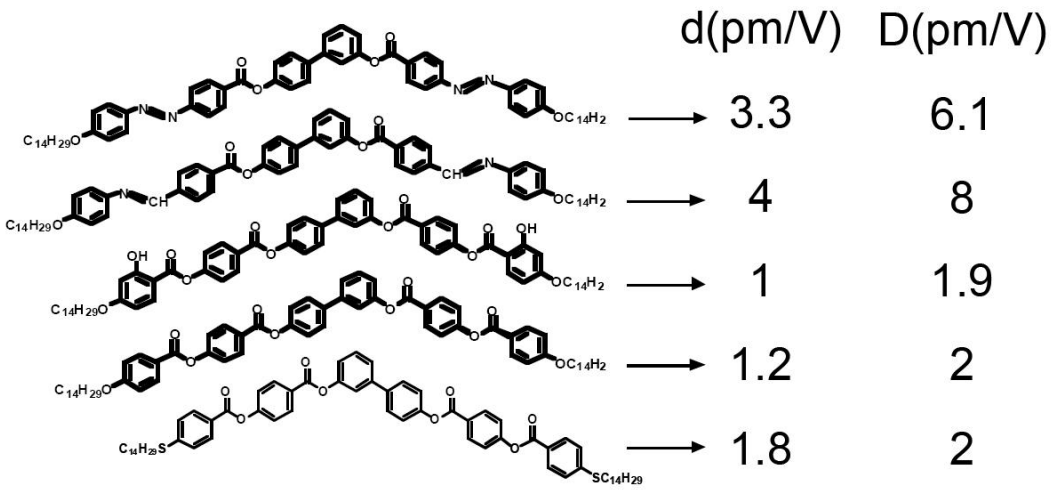

Fig. 22: Values of the NLO coefficients (see tensor (6) pg. 21) for several typical bent-core compounds.

In this thesis, several bent-core materials including different donor and acceptor groups, as well as different conjugations, were studied. Of course, trying to make innovative liquid crystal materials including new functional groups is not easy and several dead-ends were encountered. Fortunately, not all of the attempts were unfruitful and, as described below, some interesting results were indeed obtained.

Piperazine and α-cyanocinnamate groups

A bent-core molecule was synthesised including piperazine and α-cyanocinnamate due to their outstanding behavior as donor and acceptor groups respectively [47]. As can be seen in Fig. 23, the conjugation is also good via an azobenzene system.

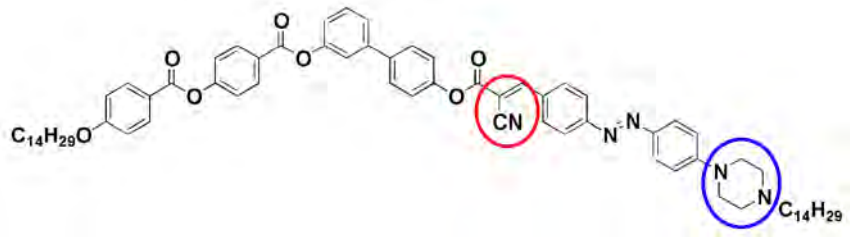

Fig. 23: Molecular structure of the compound studied. It is worth noticing the piperacine (blue) and α-cyanocinnamate (red) groups conjugated via an azo linkage to maximize NLO effects.

This custom-made molecule has all the ingredients to have a great NLO efficiency. As a starter, using EFISH (at a fundamental wavelength 1.9 μm) an encouraging estimation of $\mu\beta$=560·10-48 esu was obtained for the compound. In this quantity μ is the permanent dipole moment and β the vector part of the hyperpolarizability tensor along

μ. However there are not only pros, some cons are also found without much effort. First of all, the material is not a mesogen. As shocking as this is, this obstacle is not as big as it can seem at the beginning and it can be overcome making a mixture with a mesogenic host matrix. In this case, a 0.5 mole fraction mixture of this compound with the fourth compound in Fig. 22 gave rise to the following phase sequence presenting a convenient polar mesophase: Iso - 155ºC - SmC_AP_A - 45.4 – Xtal.

For the SHG measurements we needed aligned samples, which are not always possible to obtain when working with bent-core materials. In this case, using the type of cells described in Fig. 11, we managed to obtain good oriented samples in the field-induced SmC_SP_F phase (see Fig. 24)

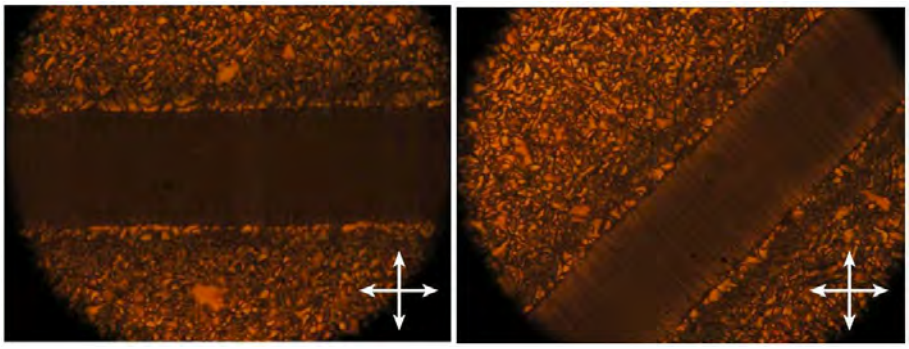

Fig. 24: Aligned gap under a 4.3 Vμm^{-1} field in the 1.3 μm thick cell. Clear extinction is achieved confirming the quality of the molecular alignment. The size of the gap is 60 μm.

Apart from the mesogenicity issue, we find what probably is the main drawback: the transparency-efficiency trade-off. The material has a strong absorption band in the blue and green parts of the spectrum (see Fig. 25), which gives it an intense red color. This has to be taken into account when calculating the non-linear coefficients if the light used in the NLO experiment (either fundamental or generated) lies in that part of the spectrum. There are two options to go around this problem: i) Either use light out of the absorption band to measure the NLO coefficients out of the resonance; ii) or account for the absorption in the material including the imaginary part of the index of refraction to obtain the SHG efficiencies in the resonance zone.

Obviously the first option is the simplest and the cleanest, and in the second case one has to realize that too much absorption can lead to big difficulties in the measurements as well as in the data processing. In our case, the effect of the absorption is, in fact, reduced in the mixture (since the matrix is completely transparent at those wavelengths).

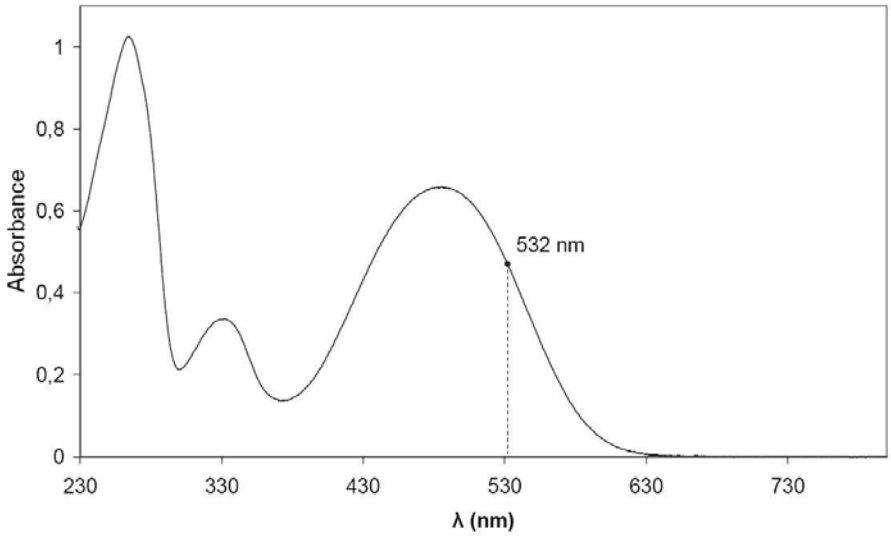

Fig. 25: Absorption spectrum of the studied compound (see Fig. 23) in a solution of CH_2Cl_2 with a concentration $c=1.86\cdot10^{-5}$ M and an interaction length of 1 cm. The absorbance at 532 nm is $A_{532} = 0.47$. This parameter is defined through the equation $I/I_0=10^{-A}$ with I and I_0 the trasmitted and incident light intesities. The molar absorptivity is $\varepsilon=A/c$ (absorbance of a 1M solution with a 1 cm interaction length) In our case: $\varepsilon_{532} = 25561\ M^{-1}cm^{-1}$.

In any case, it is always interesting to know how a material behaves in the region close to the resonance and, since there are not many studies on the real effects of resonances in the SHG in general, and none in liquid crystal materials, we decided to employ both methods and compare results.

i) Non-absorptive measurement:

Looking at the absorption spectrum (Fig. 25) one easily sees that to be out of the resonance zone the SH needs to occur at wavelengths longer than 630 nm. We used the experimental setup described in Chapter 2 working at a fundamental wavelength of 1600 nm and safely generating at 800 nm.

In eq. (3) we can group factors in a constant *C* that can be obtained from a measurement of the SHG intensity at the maximum of the first Maker's fringe from a y-cut quartz sample in the p-p configuration of the light polarization. Doing so we obtain the following equation:

$$P^{2\omega}=C\cdot d_{eff}^{2}L^{2}\frac{\sin^{2}\left(\frac{2\pi\,\delta n\,L}{\lambda}\right)}{\left(\frac{2\pi\,\delta n\,L}{\lambda}\right)^{2}} \tag{8}$$

Where δn is the material index mismatch between the second harmonic and the

fundamental light, which depends on the experimental configuration of the polarizer and analyzer.

Using the procedure described in Chapter 2 and using cells of different thicknesses (5.5, 9.8 and 18 μm) we fitted the p-p signals as shown in Fig. 26 to eq. (8) to get a value for $d_{eff}=d$ (see tensor for the SmC_SP_F phase (eq. (6) on pg. 21)). Since it was the first time we used this experimental setup, we used two cells of each of the thicknesses (see graph below) to confirm reproducibility.

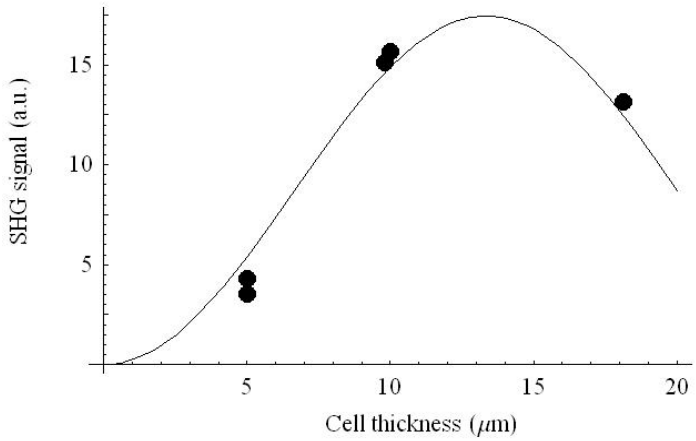

Fig. 26: The black dots are SHG data obtained for 5 different cells of the studied mixture in the p-p configuration of the light and using 1600 nm fundamental wavelength. Some thicknesses are repeated to confirm reproducibility. The solid line corresponds to a fit to eq. (8) with the following parameters: d=4 pmV^{-1} and $\delta n=n_o(2\omega)-n_o(\omega)=0.03$.

The resulting value is d=4 pmV^{-1}. We can extrapolate this result to the pure compound, getting a d_{pure}=8 pmV^{-1}. This linear extrapolation in the concentration is assumed to be valid. The validity of this hypothesis has been proved in this thesis in one case with compound H2 of Fig. 29.

Measurements in the s-p configuration of the light polarization were also performed to obtain experimentally the value of D and are shown in Fig. 27. In this case d_{eff} for the pure compound is 5 pmV^{-1} and value equal to $D\sin^2(\theta)$ (see tensor (6)), where θ is the tilt angle. Despite of the determination of $\theta=44^\circ$ from X-ray measurements, optical textures point towards a clearly smaller optical tilt, which could not be accurately determined due to the small size of the domains, but was estimated to be around $30-35^\circ$. This would derive in D~17 pmV^{-1}.

A theoretical estimation of the NLO coefficients will be now made in terms of the molecular and structural parameters. We will start from the value $\mu\beta$=470·10^{-48} esu measured for the active lateral structure of the molecule by EFISH (λ=1.9 μm). On the

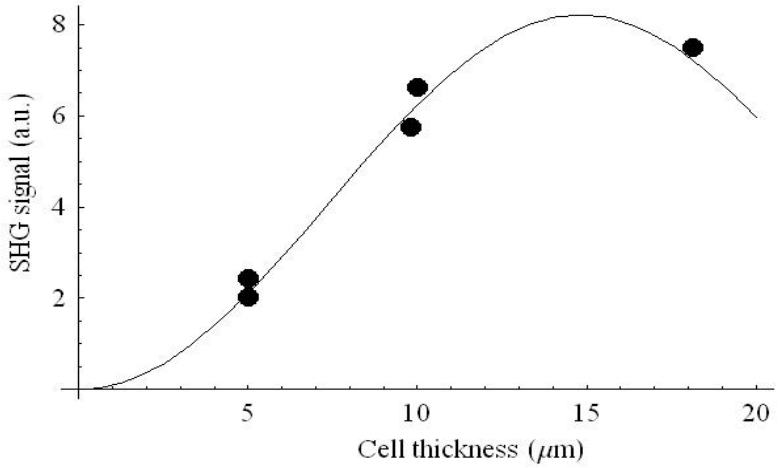

Fig. 27: The black dots are SHG data obtained for 5 different cells of the studied mixture in the s-p configuration of the light and using 1600 nm fundamental wavelength. The solid line corresponds to a fit to eq. (8) with the following parameters: d_{eff}=2.5 pmV^{-1} and $\delta n=n_e(2\omega)-n_o(\omega)$=0.03.

other hand, using the AM1 molecular model, the dipole moment of this structure is μ=4.5 D (debyes). We can then estimate a β_l=100·10^{-30} esu longitudinal hyperpolarizability component. Using the formulas in pg. 21 and assuming that $\langle\cos^3\Psi\rangle\approx 0.7\langle\cos\Psi\rangle$ (gaussian distribution for the Ψ angle) and $\langle\cos\Psi\rangle=0.61$ (as for the classic P-8-OPIMB [48]) we obtain that D'=0.1D and d=0.23D.

Finally, taking N=(6.023·10^{23}/P_m) cm^{-3}, P_m=1162 g, a mass density of 1 gcm^{-3}, and the local field factor f^3=3 (in the Lorentz approximation, $f=(n^2+2)/3$, where n *is* the refractive index) D=14.9 pmV^{-1}, which implies that d=3.4 pmV^{-1} at 1.9 μm. Using a two level model [49] with λ_0=472 nm from Fig. 25 these values are slightly corrected to D=17.5 pmV^{-1} and d=4.0 pmV^{-1}, theoretical results that are in surprisingly good agreement with the experimental ones given the amount of assumptions involved in the estimation.

ii) Resonance-enhanced measurement:

The maximum of the absorption band is at 472 nm (Fig. 25) so that our Nd:YAG laser generating SHG at 532 nm is the perfect tool for the study of the material behavior close to the resonance. The experimental setup is depicted in Chapter 2.

As mentioned above eq. (3) is no longer valid and has to be rededuced taking the absorption into account (complex index of refraction). This has been done in [40], where Herman and Hayden corrected the theory of Jerphagnon and Kurtz [50] for the SHG in absorbing materials. If there is absorption only at 2ω, the formula to be used is

[40]:

$$P^{2\omega} \propto d_{eff}^2 L^2 e^{-aL/2} \frac{\sin^2\left(\frac{2\pi\delta n L}{\lambda}\right)+\sinh^2(aL/4)}{(2\pi\delta n L/\lambda)^2+(aL/4)^2} \quad (9)$$

where *a* is the absorption coefficient and can be calculated from the absorption spectroscopy data, and the rest of the quantities are defined as for equation (3). For the calculations we obtained *a* from linear extrapolation of the data of the material in a solution of CH_2Cl_2 (Fig. 25) to the concentration of the mixture. The resulting value is 2.52 μm^{-1}.

As in the non-absorptive case, there are two unknown quantities in equation (9), d_{eff} and δn, and we need more than one measurement to get them. The approach is the same and 0.55, 0.75, 1.35, 2.10 and 5.50 μm thick cells were used to perform the fit shown in Fig. 28 for the p-p configuration of the incoming and generated light polarizations.

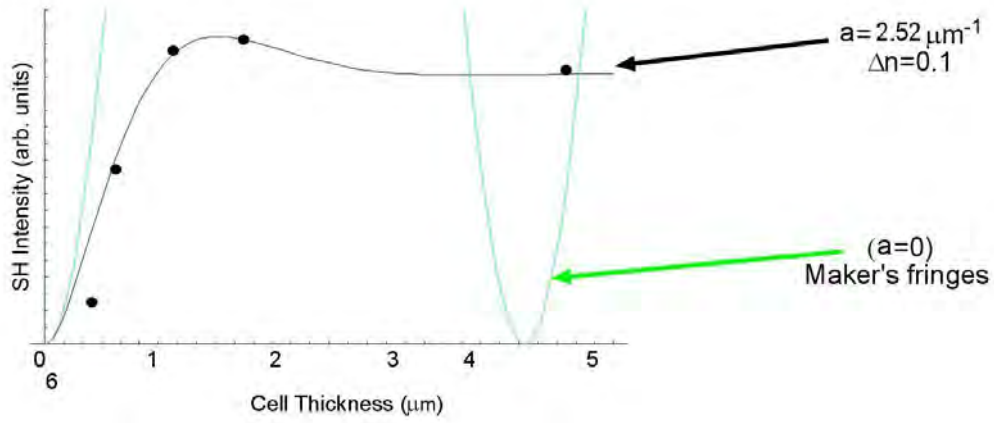

Fig. 28: The black dots are SHG data obtained for 5 different cells of the studied compound in the p-p configuration of the light and using 1064 nm fundamental wavelength. The solid line corresponds to a fit to eq. (9) with the following parameters: d=24 pmV^{-1} and Δn=0.1, which gives a d_{pure}=48 pmV^{-1}(assuming linear concentration dependence). Also the non-absorptive case is graphed in green, showing the so-called Maker's fringes.

d_{pure}=48 pmV^{-1} is obtained for the pure compound. Again, using eq. (5), we can estimate the value for the other coefficient: D_{pure}~140 pmV^{-1}. These results, though resonance-enhanced, are very remarkable.

After measuring the NLO coefficient *d* at both wavelengths we can compare them directly and obtain, for the first time an enhancement factor: 48/8=6. Also from the value of D_{pure}=17 pmV^{-1} at λ=1.6 μm and using this enhancement factor we could make another estimation of D_{pure} at λ=1.064 μm of more than 100 pmV^{-1} confirming the order of magnitude of the measured coefficients.

DR-1 dimer

An alternative molecular geometry to bananas with the capability of accepting chromophores with large hyperpolarizabilities along the polar axis keeping at the same time the proper shape for mesogenicity was suggested in [51] by Walba *et al.* This new approach was based on a novel "H-shaped" molecular structure including the prototypical NLO chromophore p-nitro-p'-(dialkylamino)-azobenzene (the chromophore found in the NLO dye disperse red 1 (DR1)) in which a pair of rod-shaped molecules are connected by an azo bridge. Various compounds were synthesized [51], and although none of them possessed the necessary polar phases for NLO applications, the approach was good and worthy of further research.

Recently two dimer-like FLCs with appropriate phase sequences were synthesized by chemists at Displaytech Inc. [52]. An azo bridge connects the two calamitic structures in compound H1, whereas compound H2 presents the NLO disperse red DR-1 chromophore. The molecular structure and phase sequence of these materials are shown in Fig. 29. As can be seen, broad temperature ranges are obtained for the enantiotropic ferroelectric phases, which were carefully characterized by POM, X-ray diffraction and polarization current response [52].

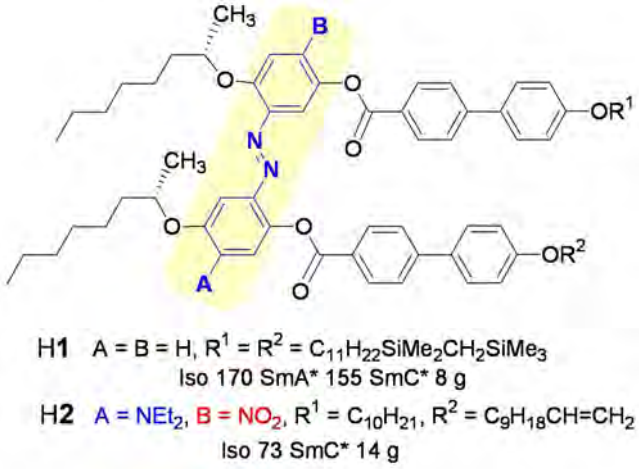

Fig. 29: Molecular structure of the H shaped compounds used in this study. H1 is used as a transparent host matrix of H2, which incorporates a DR-1 NLO unit. g is a glassy state.

As in the case of the previous compound (Fig. 23), compound H2 has a strong absorption band. This time the maximum at 531 nm (see Fig. 30) is almost equal to the SHG light wavelength of our Nd:YAG laser. To quantify its NLO efficiencies by means of SHG using the Nd:YAG laser it was found appropriate to prepare mixtures of H1 and H2 to reduce the absorption effects. Two mixtures with 10 and 20% molar ratio of H1 in H2 were used. These mixtures were thermodynamically characterized and were showed to exhibit the same phase sequence as H1 [52].

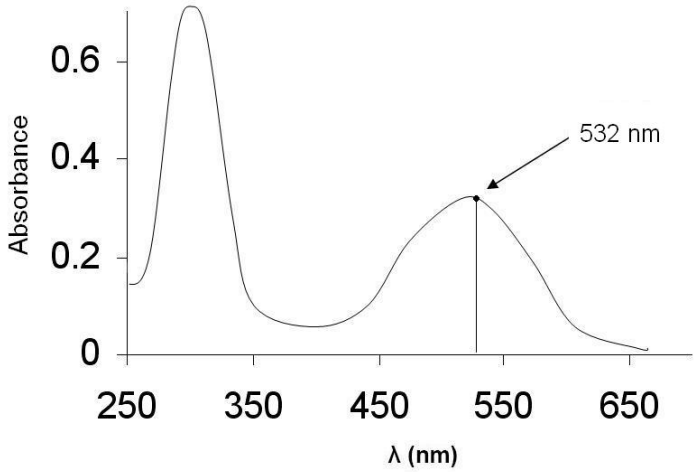

Fig. 30: UV-Vis spectrum of compound H2 (see Fig. 29) in CH_2Cl_2 solution showing a strong absorption band at 531 nm, the absorbance and molar absorptivity at 532 nm are A_{532} = 0.285 and ε_{532} = 33912 $M^{-1}cm^{-1}$).

Cells with nominal thicknesses of 1, 2, and 3.75 μm and in-plane electrodes were employed. Under the application of an electric field, good homeotropic alignment was obtained (see Fig. 31). The saturation of the SHG signal was obtained applying fields around 0.6 $V\mu m^{-1}$.

As with the previous compound, the absorption coefficient *a* was deduced doing a linear extrapolation from the UV-Vis spectrum of H2 in dilute CH_2Cl_2 solution (Fig. 30) obtaining a value of 0.614 μm^{-1} for the mixture at 10% concentration and the double for the one at 20%.

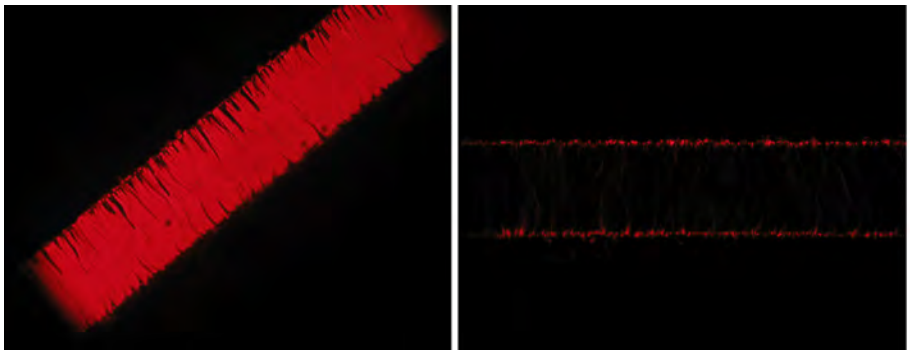

Fig. 31: Aligned 100 μm wide gap under the application of a high electric field. Clear extinction is achieved confirming the quality of the molecular alignment.

As can be seen, the DR-1 unit is almost directed along the FLC polar axis (see Fig. 29). Being so, it is the d_{22} coefficient the one maximized by the chemical design (see tensor (6) on pg. 21, which has the exact same form as the one of a SmC*). Graphs in Fig. 32a

and b show the results in the p-p configuration of the light polarization. The fits to equation (9) in δn and d_{eff} for the 10 and 20% mixtures at a temperature of 165ºC give $d_{22}(10\%)=1.5$ and $d_{22}(20\%)=3.9$ pmV^{-1} respectively. Measuring in other configurations we confirmed that the remaining d_{ij} coefficients were much smaller. This fact proves that the DR-1 unit is, as designed for it, well directed along the polar axis.

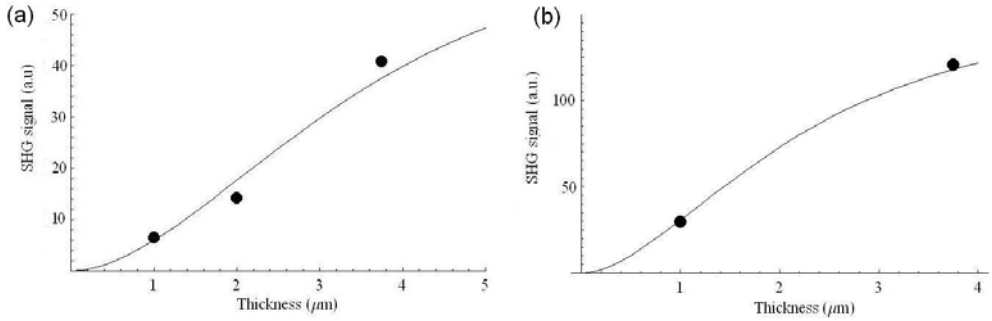

Fig. 32: SHG experimental data and theoretical fit to eq. (9) for the mixtures at (a) 10% and (b) 20% concentration.(fundamental wavelength at 1064 nm and p-p configuration). The fitting values are $d_{22}(10\%)=1.5$ and $d_{22}(20\%)=3.9$ pmV^{-1} ($\delta n\sim0.02$).

With these results an extrapolation for the value of $d_{22}(100\%)$ in the pure compound can already be made. The efficiency of compound H1 alone was checked to be negligible so we can state that the signal comes exclusively from compound H2. The value of $d_{22}(20\%)$ is roughly the double of that of $d_{22}(10\%)$, what is consistent with a linear dependence of this value with the concentration. Consequently the extrapolation gives a $d_{22}(100\%)$ of 15 pmV^{-1} (starting from the value obtained for the mixture at 10% because of the use of three cells instead of two), making it at least three timer larger than those of the best calamitic FLCs [53] and comparable to that of most bent-core materials (see Fig. 22).

A typical temperature dependence of the SHG signal is graphed in Fig. 33. This data was obtained cooling the 3.75 μm thick cell at 20% concentration under a 0.4 Vμm^{-1} DC electric field from the isotropic phase. The signal gradually increases as the temperature decreases, topping at around 50 ºC and remaining constant a lower temperatures. Once the field was turned off at room temperature, the signal dropped to half the field value after 10 minutes and to one fourth of it after 2 hours. This fact reveals a supercooled ferroelectric phase relaxing slowly to the helical ground state SmC*.

Of course, as before, we have to take into account that the high value of d is enhanced by the resonance of Fig. 30. To know to what extent this value is enhanced we also performed SHG measurements of these cells at a fundamental wavelength of 1600 nm. Now the theoretical treatment of the measured data is that of the transparent case. Fittings in δn and d_{eff} (d_{22}) are shown in Fig. 34a and b.

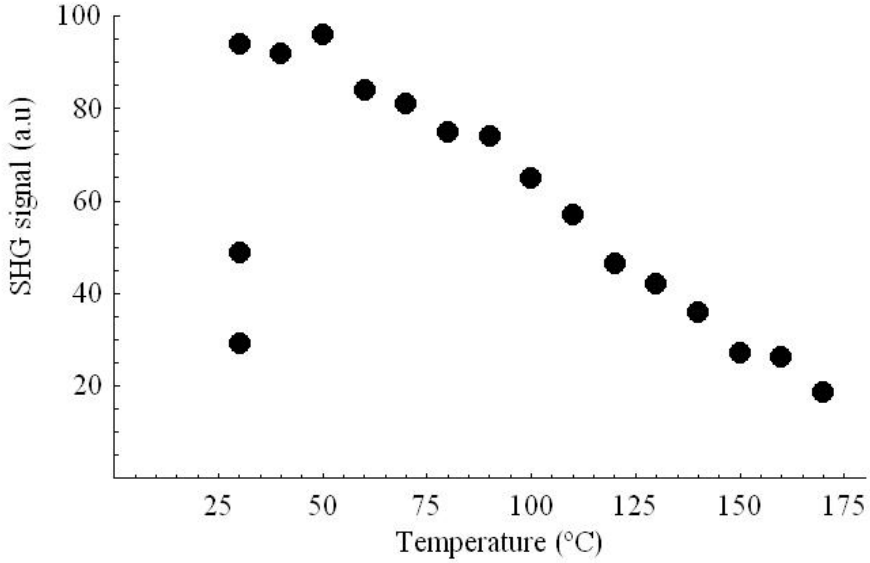

Fig. 33: Temperature dependence of the SHG signal. Data for the 3.75 μm thick cell with a 20% concentration is show when cooling under a 0.4 $V\mu m^{-1}$ electric field. The three data points corresponding to the lowest temperature are taken with the field applied, and 10 and 120 minutes after switching it off.

As expected, these values are not as large as the ones calculated for the absorptive case but, still, they are very high and one whole order of magnitude larger than the values reported for calamitic NLO FLCs. Here, the linear dependence of the d values with the concentration is clearly observed.

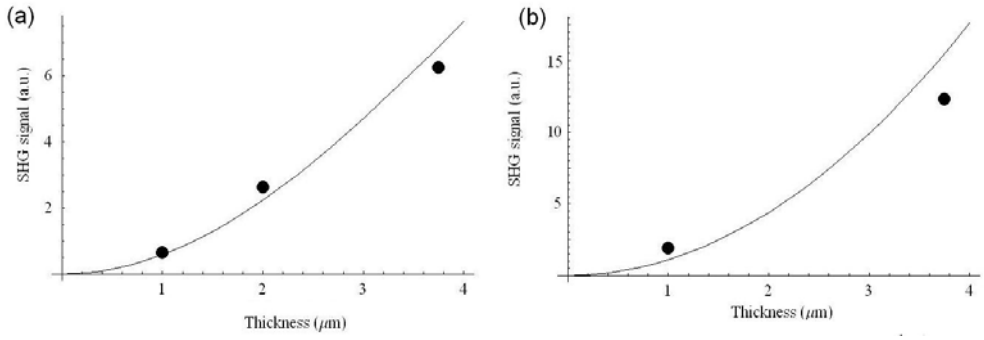

Fig. 34:SHG experimental data and theoretical fit to eq. (3) for the mixtures at (a) 10% and (b) 20% concentration.(fundamental wavelength at 1600 nm and p-p configuration). The fitting values are $d_{22}(10\%)=0.43$ and $d_{22}(20\%)=0.95\ pmV^{-1}$ ($\delta n\sim 0$)

From a direct comparison of the values obtained in the absorbing and non-absorbing cases we can estimate that the resonance enhancement factor is around 4. It is really interesting to see that experimentally this divergence is not so huge, and this, together with the result obtained for the previous compound (Fig. 23) give a qualitative idea of the behavior of the NLO coefficients in the resonance zone.

Finally measurements directly with the pure H2 compound were carried out. The high absorption band of this compound peaking at 531 nm (see Fig. 30) makes the data obtained by generating SH light in that part of the spectrum not treatable. This lead us to only perform measurements with a 1600 nm wavelength light (where the sample is transparent for the fundamental as well as for the SHG light).

The pure compound has a rather high viscosity, which reveals itself in the high electric fields necessary to align the material in the homeotropic cells. Fields as high as 22 $V\mu m^{-1}$ were employed to obtain a decent saturation of the SHG signal. Cells with 100 μm wide gap between electrodes and thicknesses of 1, 2, 3.75, 7 and 11 μm were used. The fit in δn and $d_{22}(100\%)$ is shown in Fig. 35 for the optimized configuration (p-p light and normal incidence).

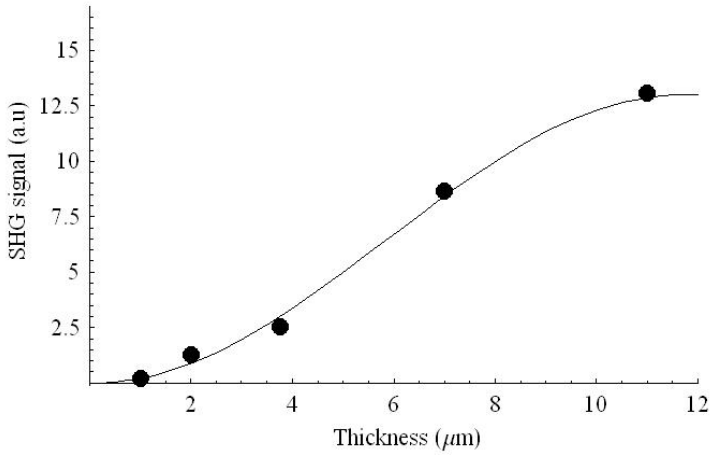

Fig. 35: SHG experimental data and theoretical fit to eq. (3) for the pure compound H2 (fundamental wavelength at 1600 nm and p-p configuration). The fitting values are $d_{22}(100\%)=4.5\ pmV^{-1}$ and $\delta n=n_o(2\omega)-n_o(\omega)=0.04$.

A very remarkable value for $d_{22}(100\%)$ of 4.5 pmV^{-1} was obtained in this transparent zone. Again, this result proves the good design of the molecule to optimize the NLO response.

Also the $d_{21}(100\%)$ coefficient (s-p configuration) was measured and a value of 1.5 pmV^{-1} was obtained. The results and fit are shown in Fig. 36.

Comparing now the concentration dependence of the d_{22} coefficient on the concentration, a linear relation is revealed (see Fig. 37), confirming the validity of the hypothesis made above.

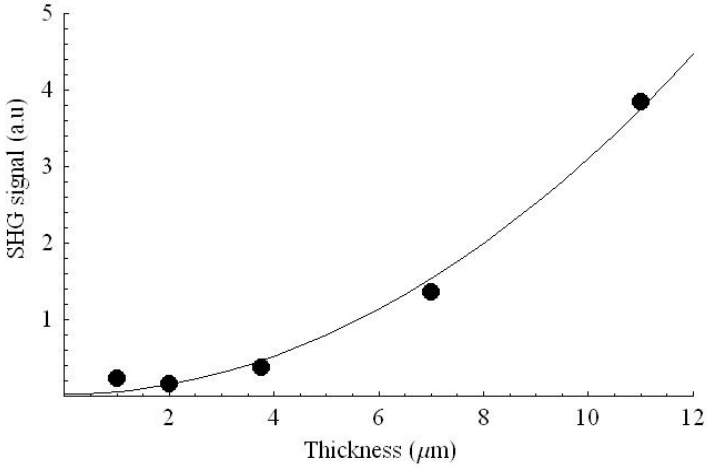

Fig. 36: SHG experimental data and theoretical fit to eq. (3) for the pure compound H2 (fundamental wavelength at 1600 nm and s-p configuration). The fitting values are $d_{12}(100\%)=1.5\ pmV^{-1}$ and $\delta n=n_e(2\omega)-n_o(\omega)\sim 0$.

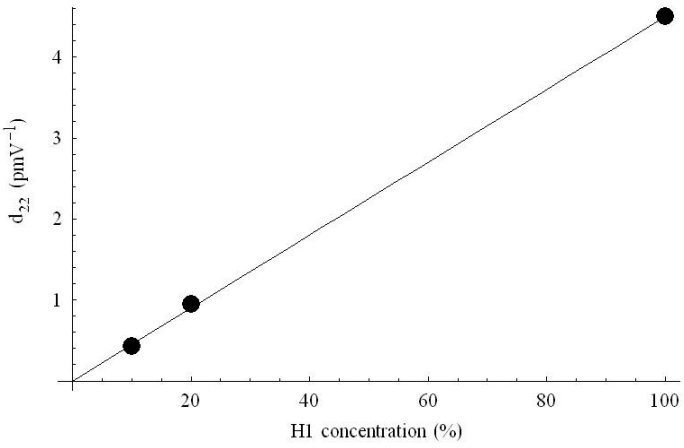

Fig. 37: Concentration dependence of the d_{22} coefficient. A clear linearity can be deduced from the data points.

We now turn to present a simple theoretical calculation to account for the NLO coefficients the pure compound. The molecule is modeled as possessing a single hyperpolarizability vector component β along the DR-1 group. This hyper-polarizability component makes an angle φ with the macroscopic polarization direction (see Fig. 38).

To account for the head-tail invariance in liquid crystals, we can assume that layers are composed of a 50% mixture of molecules with both orientations (see Fig. 38). When calculating the molecular hyperpolarizabilities and summing up for both populations, only the components $\beta_{yyy}=\beta\cos^3\varphi$ and $\beta_{zzy}=\beta\cos\varphi\sin^2\varphi$ survive, and are equal

for both populations. If a possible disorder around the z axis (characterized by the angle Ψ) is permitted we have:

$$\beta^d_{yyy} = \langle \cos^3 \Psi \rangle \beta_{yyy}$$

$$\beta^d_{yxx} = \langle \cos \Psi \sin^2 \Psi \rangle \beta_{yyy}$$

$$\beta^d_{yzz} = \langle \cos \Psi \rangle \beta_{yzz}$$

where the brackets represent thermal averages.

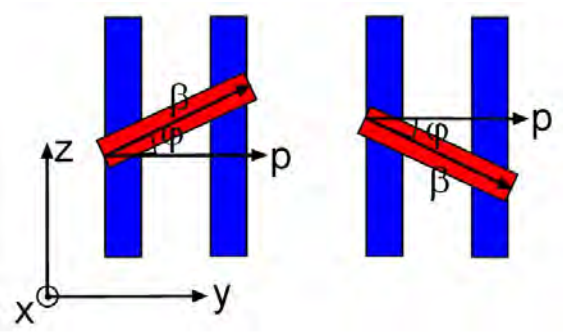

*Fig. 38:Head-tail invariance can be simulated by assuming populations with 50% weight in each layer of the two molecular orientations depicted. The blue parts represent the calamitic legs of the molecule and the red one the DR-1 unit. **p** is the macroscopic polarization direction, β the hyperpolarizability vector component and φ the angle between them.*

If we now position the molecule in the frame of reference XYZ of the SmC phase (where X is directed along the tilt direction in the smectic layer, Y along the layer polarization and Z along the layer normal) we have:

$$\beta_{YYY} = \beta^d_{yyy}$$

$$\beta_{YXX} = \beta^d_{yxx} \cos^2 \theta + \beta^d_{yzz} \sin^2 \theta$$

$$\beta_{YZZ} = \beta^d_{yxx} \sin^2 \theta + \beta^d_{yzz} \cos^2 \theta$$

$$\beta_{XYZ} = \beta^d_{yxx} \sin \theta \cos \theta - \beta^d_{yzz} \sin \theta \cos \theta$$

where θ is the tilt angle.

The susceptibility tensor components that survive are:

$$d_{22} = Nf^3 \beta_{YYY}$$

$$d_{21} = Nf^3 \beta_{YXX}$$

$$d_{23} = Nf^3 \beta_{YZZ}$$

$$d_{14} = Nf^3 \beta_{XYZ}$$

and we can obtain the following relationship for the two coefficients measured experimentally:

$$\frac{d_{21}}{d_{22}} = \frac{\cos^2\theta \langle \cos\Psi \sin^2\Psi \rangle \beta_{yyy} + \sin^2\theta \langle \cos\Psi \rangle \beta_{yzz}}{\langle \cos\Psi \rangle \beta_{yyy}}$$

Assuming $\langle \cos^3\Psi \rangle \approx 0.7 \langle \cos\Psi \rangle$ (gaussian distribution for Ψ):

$$\frac{d_{21}}{d_{22}} \approx \frac{0.3}{0.7}\cos^2\theta + \frac{1}{0.7}\sin^2\theta \tan^2\varphi$$

In the present case $\varphi = 25º$ and $\theta = 44º$ and we obtain: $d_{21}/d_{22} = 0.37$, which compares correctly with the experimental result: 0.33.

On the other hand, using the experimental P_s results and the theoretical value (AM1 molecular model) for the transverse dipole moment (μ=2.077 D) we have made a theoretical estimate of d_{22}. From $P_s = N\mu\langle \cos\Psi \rangle$, taking P_s =70 nCcm^{-2} at 70 ºC, and N=4.7·10^{26} m^{-3} (assuming a mass density of 1 gcm^{-3} and a molecular mass 1272 g) we deduce $\langle \cos\Psi \rangle = 0.21$. On the other hand, if there is only a β unit in the molecule along the transverse direction we have approximately $d_{22} = Nf^3 \langle \cos^3\Psi \rangle \beta$. Typically $f^3 = 3$, and $\langle \cos^3\Psi \rangle = 0.15$ (assuming a Gaussian distribution for Ψ, with a width that gives the correct $\langle \cos\Psi \rangle$ value). Furthermore, we have taken β=49·10^{-30} esu according to [49]. This β value corresponds to the DR-1 molecule and is for a fundamental wavelength 1.9 μm, i.e., out of resonances. With all these data we get d_{22}=4.5 pmV^{-1}. As can be seen, the agreement is good, proving the validity of the model.

The promising results in this compound pave the way for a new molecular-shape approach in the search for a generation of liquid crystals showing competitive optimized NLO responses. Indeed, some research with trimer-like molecules possessing even larger functional groups is in progress.

TTF compounds

Thetratiafulvalene (TTF) units are known for their intermolecular charge transfer properties (see [54][55][56][57]). This fact makes them interesting to be integrated in liquid crystal materials. Three bent-core materials containing TTF units are extensively studied and characterized in Chapter 7, but here, due to the a priori suitability of these compounds for NLO applications, a short comment about their NLO properties will be included.

A complete characterization of the second order susceptibility tensor **d** could not be carried out because of the high threshold electric field to obtain aligned samples. Nevertheless, a rough estimation could still be made for two of the three compounds (I and II in Fig. 76, pg. 90) in non-oriented samples, containing each of them one TTF unit.

The saturated (30 $V\mu m^{-1}$) SHG signal obtained in these non-oriented planar samples is about five times that of typical bent-core compounds as, for instance, P-8-O-PIMB [37]. Assuming that the sample is formed by a random distribution of domains whose size is smaller than the SHG coherence length, the second order dielectric susceptibility components d_{ij} can be roughly estimated to be about twice those values.

Taking into account that the molecules have only one active leg possessing a TTF group, the synthetic strategy of using such units can give rise to materials with even higher NLO efficiencies. For example, a similar bent-core molecule with a TTF group in each leg would double the values of the d_{ij} components, i. e. four times those of P-8-OPIMB. Using the data of this compound, we would obtain really remarkable d_{ij} coefficients of about 20 pmV^{-1}. This proves the validity of the TTF donor group as a good choice to enhance the NLO properties in this kind of materials, despite the π-system is not optimized in the present molecules since the ester group breaks the conjugation.

Chapter 4

Study of aligned samples of modulated phases

In this chapter, three compounds presenting the B1-B2 dimorphism will be studied by means of X-ray diffraction on aligned samples. This will allow for a better understanding of the columnar phases, and a new model will be proposed for the dipole ordering among the different blocks in these structures.

The B1-B2 transition is rather unusual and very few compounds have been reported to posses such dimorphism [28][58][59][60][61]. In some cases it has been found that an electric field can induce this B1-B2 sequence [28][60][61]. A priori, this transition from columnar to smectic phase would suppose a huge structural change but, surprisingly, the transition enthalpy observed by DSC measurements is very small [62], meaning the change cannot be too drastic. This shocking characteristic common to this type of materials makes it interesting to look deeper into the transition mechanism. Some studies have already been done [62]. Moreover, as mentioned in the introduction, there are several structures (with different symmetry groups) under the B1 nomenclature, and the well-established character of the B2 phase can help to shed some light onto the B1 structure if the transition is correctly understood.

For this study, drops of compound A, B and C were analyzed by means of SAXS in a Brucker Nanostar diffractometer (see Chapter 2). The samples were aligned by cooling the isotropic phase of the materials below the clearing point at different cooling rates.

Compound A

The molecular structure, X-ray diffraction diagram as a function of temperature and typical 2D X-ray diffraction patterns for the B1 and B2 phases of compound A are shown in Fig. 39. The centered cell parameters in the columnar phase are a=100.9 Å and c=56.8 Å (at 150 ºC) giving the diffraction pattern a pseudo-hexagonal symmetry. The parameters show no appreciable temperature dependence in all the B1 phase range.

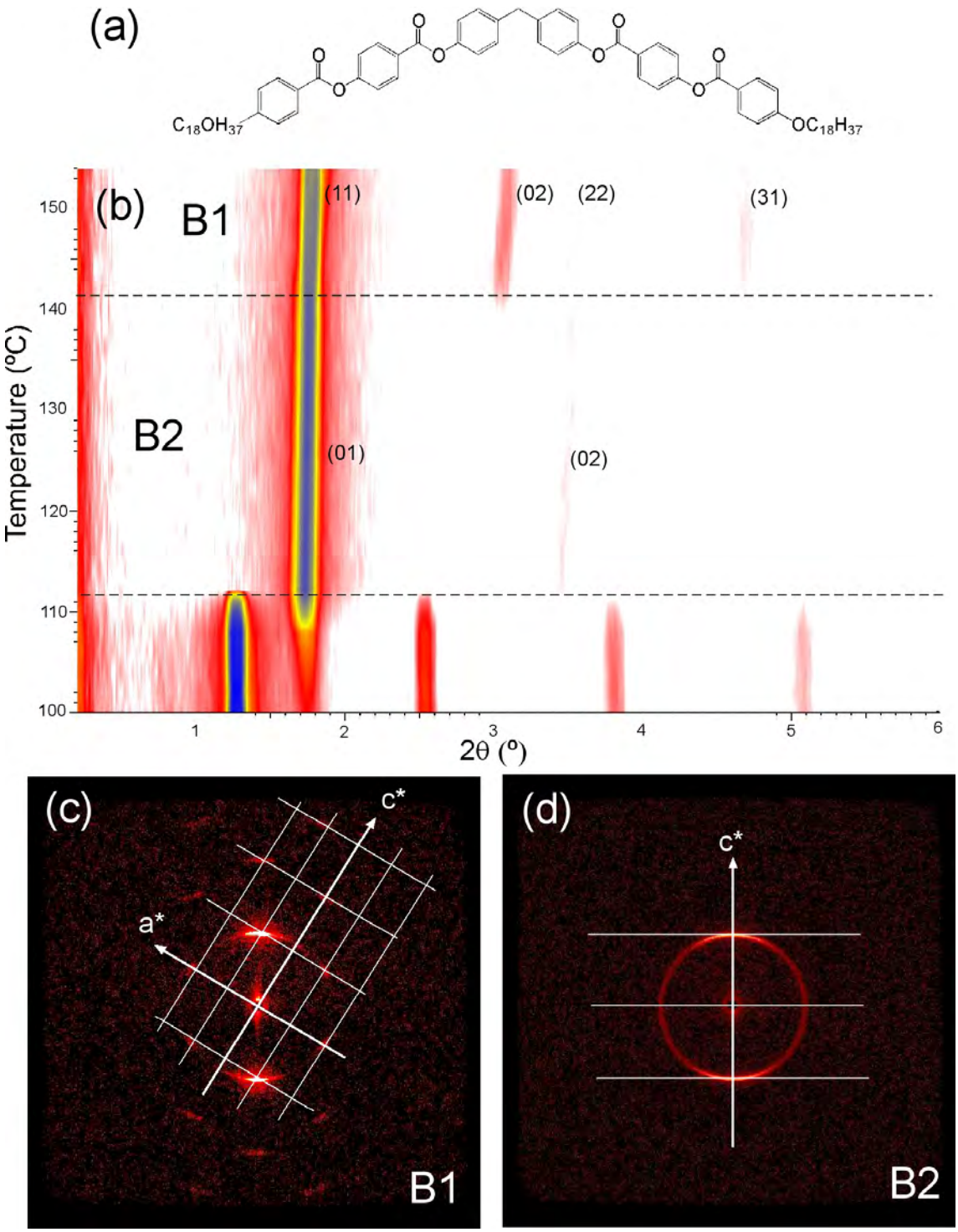

Fig. 39: (a) Molecular structure of compound A. (b) X-ray diffraction diagram as a function of temperature. (c) and (d) X-ray diffraction pattern for aligned drops in the B1 and B2 phases respectively.

As can be seen in Fig. 39b, the peak (11) in the B1 phase transforms into the smectic peak of the B2 phase in a continuous fashion and consequently the layer spacing is equal to the distance corresponding to the (11) reflection in the columnar phase (49.7 Å) at the transition temperature. In addition, in Fig. 39c and d we can see that the alignment is kept during the transition and the two mentioned directions coincide.

A comment must be made regarding the indexation of Fig. 39c. For the correct indexation, it has to be taken into account that the meridian direction is always a mirror plane in the 2D X-ray diagrams obtained from drops. This occurs because the aligned drops are made of domains with all possible orientations around the vertical axis. In the diagram of Fig. 39c with pseudo-hexagonal symmetry this mirror plane implies that all peaks out of the meridian are in fact double peaks coming from a lattice equivalent to the one sketched there but rotated 180 º around the (11) direction. In the following compounds, without this hexagonal symmetry, the peaks are split and both lattices are necessary to account for the peaks in the diagram (see, for example, Fig. 42).

Since smectic layers will be formed in the B2 phase, it is then logical to think that blocks of the B1 phase at the same height in the drop will have the same polarization direction. An ideal situation is depicted in Fig. 40. Rectangular blocks are tilted about 30º with respect to the normal of the substrate (or normal to the drop surface), so that the (11) planes are horizontal. Molecules inside the blocks are parallel to the *c* direction, giving rise to a perfect $B1_{rev}$ phase (see Chapter 1), with the peculiar characteristic that blocks in adjoining corners of the centered cell have opposite polarization directions (see blocks of different color in Fig. 40). The real centered cell would be four times bigger (extending *a* and *c* in Fig. 40 up to twice their value), but to directly see it, resonant X-ray diffraction is necessary, work that is currently in progress.

In the light of Fig. 40, we propose now a mechanism for the columnar to smectic transition. As the temperature is lowered, molecules at the sides of the blocks go up and down (see arrows in Fig. 41b) maintaining the parallelism and making the "layer shift" smaller than half a molecule. The blocks would not be rectangles anymore, but parallelograms (see Fig. 41a and b). When the "layer shift" disappears (in the smectic phase), the blocks would have an ideal 60º opening angle and the tilt of the molecules would be 30º. This model gives the right layer spacing ($c \cdot \cos(30º)$=49.2 Å in the B2 phase) and also would explain the low enthalpy of the process. The transition could even be second order.

It is noteworthy that in an all-trans conformation, compound A has a molecular length of 74 Å. This means that if we consider it rigid, the tilt in the smectic phase would be of 47º and of 38º in the columnar one. However, it is reasonable that the long flexible alkyl chains are somehow disordered or, maybe, molecules are interdigitated giving rise to a smaller effective molecular length, which ideally, in the framework of our model, would be the length of *c*, i.e., ~57 Å.

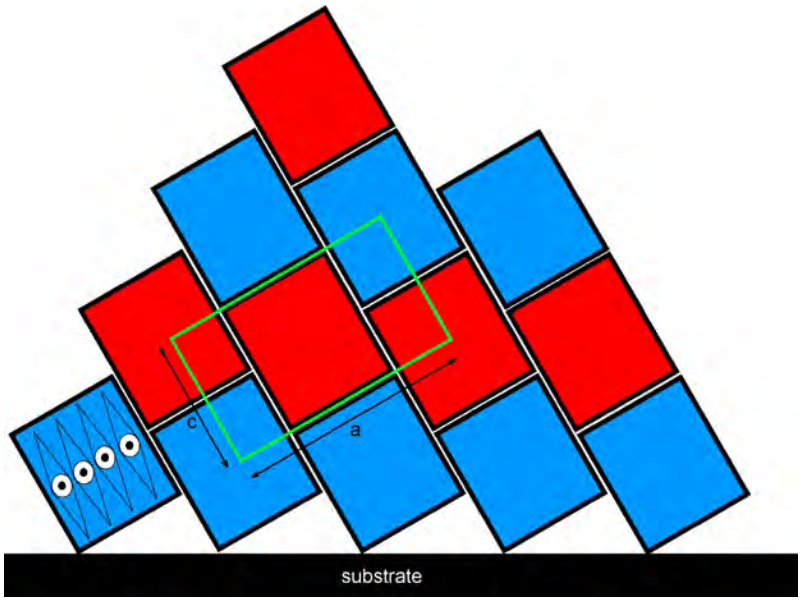

Fig. 40: Ideal arrangement of the blocks in the aligned drop. The molecules are orientated along the c direction and the blocks are tilted about 30° with respect to the substrate normal. The color of the blocks represents the polarization directions, alternating with blocks at different heights.

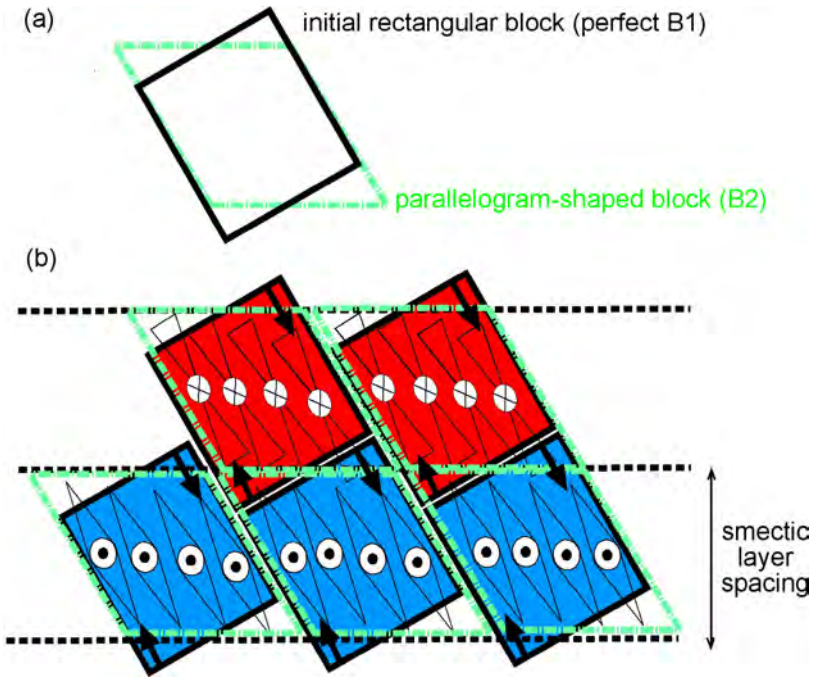

Fig. 41: (a) Sketch of the change in the block shape through the transtion from B1 to B2 phase. (b) Movement of the molecules in the blocks to form a smectic layer. The structural change can take place in a continuous fashion meaning that the transition could be of secord order.

Compound B

The molecular structure, X-ray diffraction diagram as a function of temperature and typical 2D X-ray diffraction patterns for the B1 and B2 phases of compound B are shown in Fig. 42. The centered cell parameters in the columnar phase are a=70.7 Å and c=53.7 Å (at 158 °C) and the layer spacing in the smectic phase is 45.1 Å. This compound has already been studied in ref [30], where an electric-field induced transition from B1 to B2 was found.

In this material, the alignment is also kept during the transition from the columnar to the smectic phase. The only difference with the observed behavior of compound A is a small sudden change in the position of peaks (11) in the B1 phase and (01) in the B2 (Δd=2.2 Å). The very similar behavior to that of compound A supports the generality of the proposals made above.

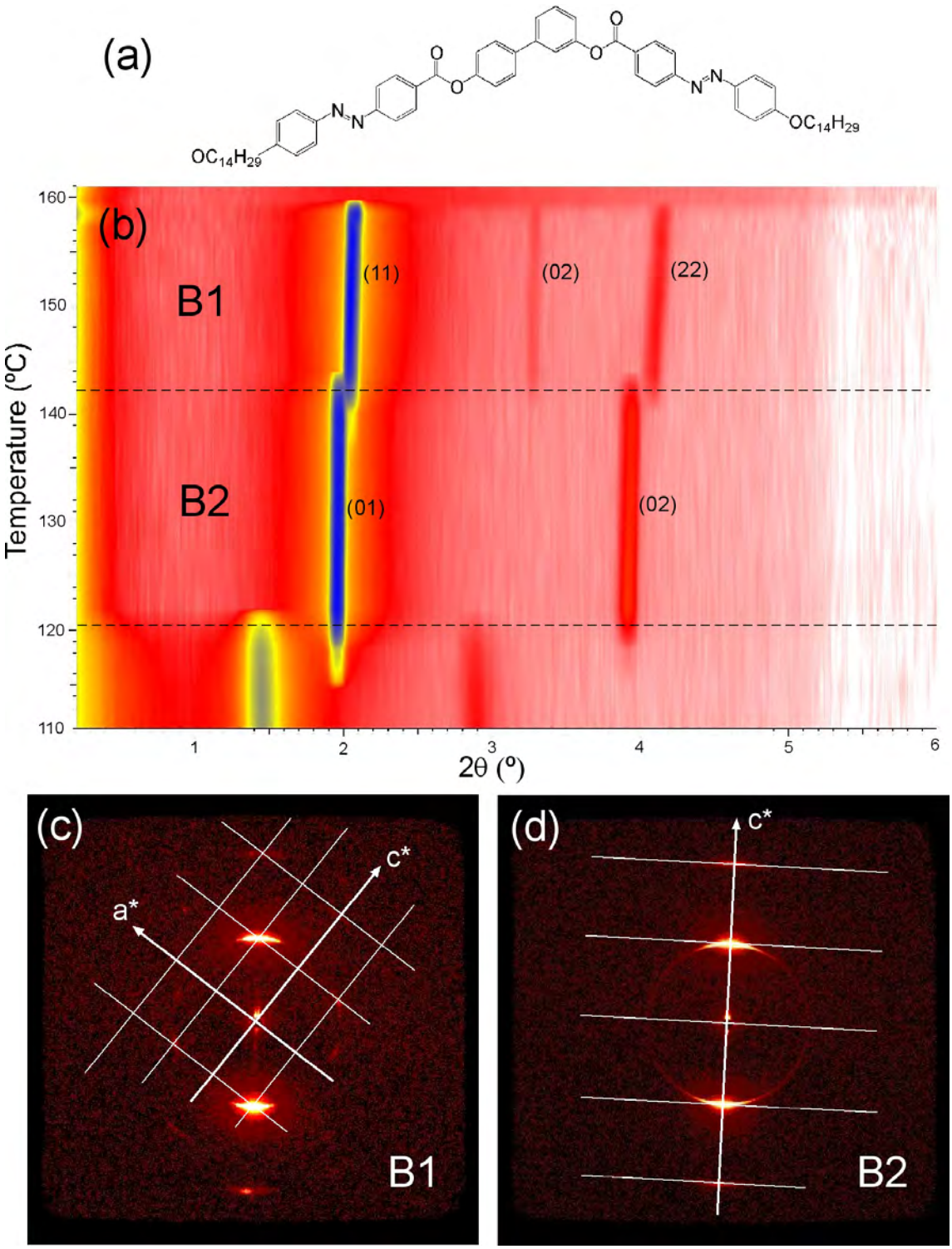

Fig. 42: (a) Molecular structure of compound B. (b) X-ray diffraction diagram as a function of temperature. (c) and (d) X-ray diffraction pattern for aligned drops in the B1 and B2 phases respectively (the slight deviation from the vertical of the (11) direction in (c) and of the (01) direction in (d) is due to a small tilt of the substrate with respect to the detector)..

Compound C

Finally the molecular structure, X-ray diffraction diagram as a function of temperature and aligned X-ray diffraction patterns in the B1 and B2 phases of compound C are shown in Fig. 43.

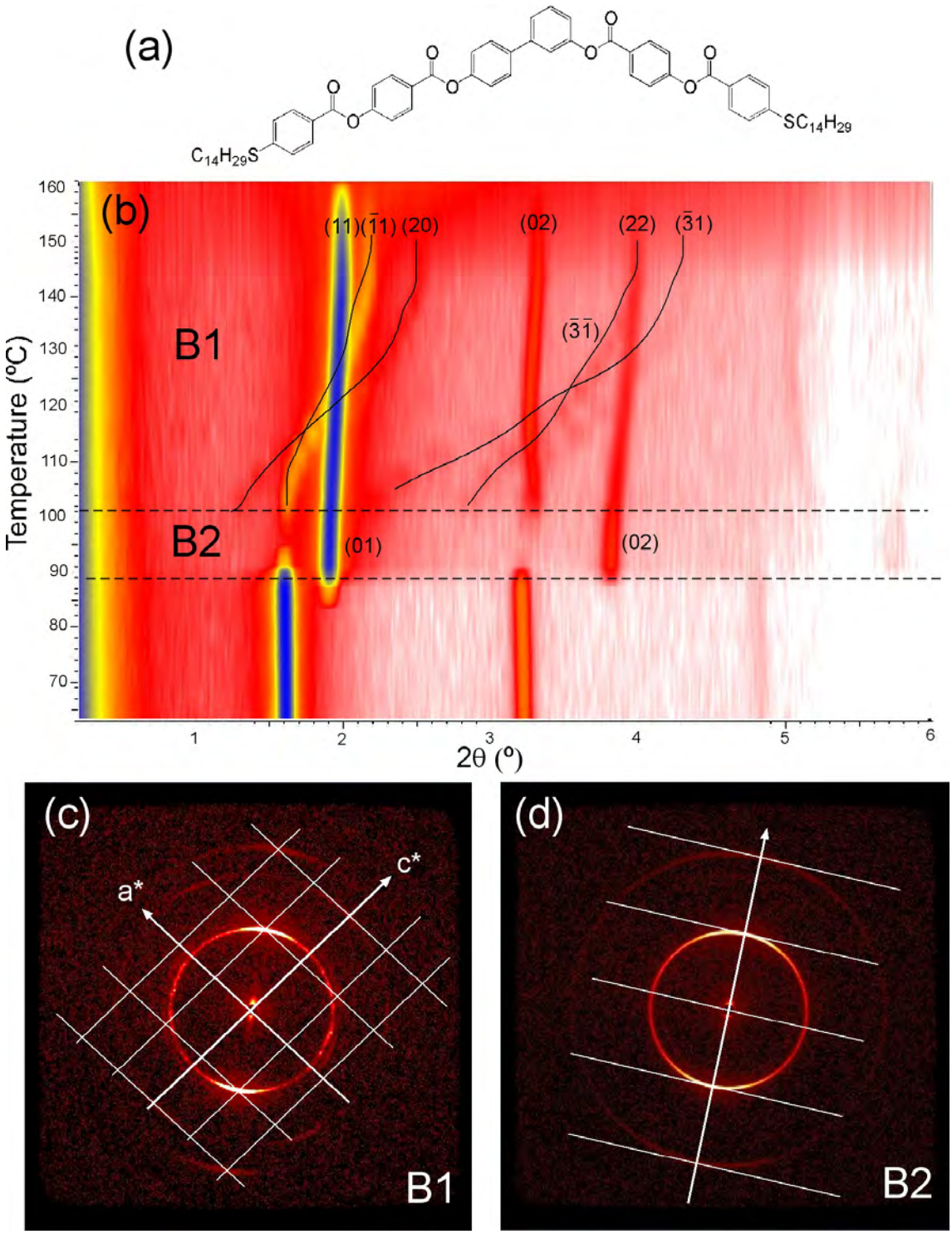

Fig. 43: (a) Molecular structure of compound C. (b) X-ray diffraction diagram as a function of temperature. (c) and (d) X-ray diffraction pattern for aligned drops in the B1 and B2 phases respectively (the slight deviation from the vertical of the (11) direction in (c) and of the (01) direction in (d) is due to a small tilt of the substrate with respect to the detector)..

In Fig. 43b, the variation of the position of peaks with large *h* Miller index is noteworthy. In Fig. 44 the change of the centered cell parameters *a* and *c* and β is shown. *c* is constant through the columnar phase temperature range, but *a*, as well as β, undergo big changes (from 70 to 134 Å and from 85 to 104° respectively). This rather unusual behavior can be seen as a lamellarization process in which the pseudo-layer spacing is kept constant, while the modulation within them changes. To enlighten this, the angle θ between the *c* (fixed) direction and the "layer" normal (see Fig. 45) is calculated and shown to be constant in Fig. 44.

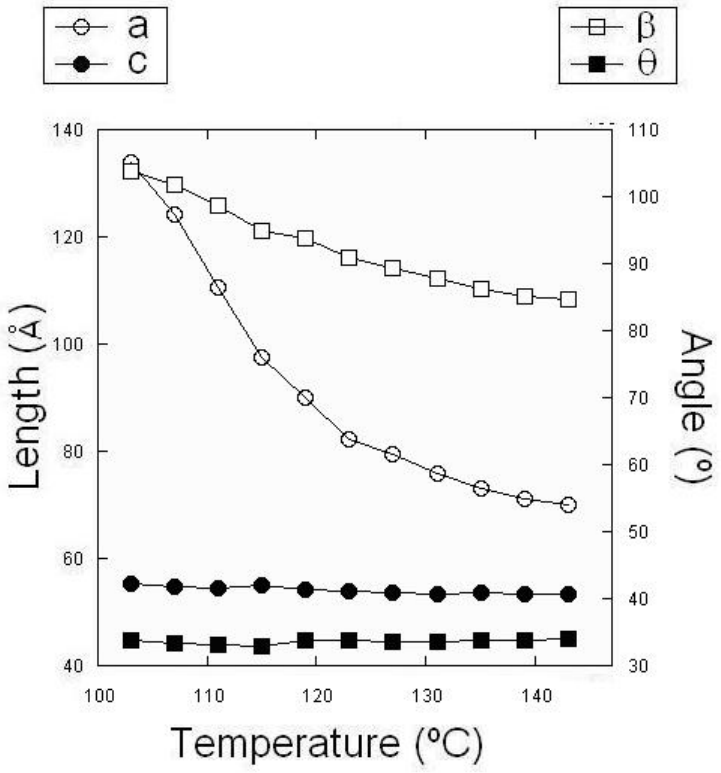

Fig. 44: Variation of the cell parameter a, c and β with temperature. Also the temperature dependence of the angle θ (see Fig. 45) is graphed..

This process may be more clearly understood using the illustrative electronic density diagrams of Fig. 46 at the two extreme temperatures of the columnar phase. On cooling, the blocks in the (11) pseudo-layers become longer and longer, but since the *c* parameter is fixed (both in the magnitude and orientation), the angle β has to increase, giving the phase even more smectic character. During the process θ is constant. At the transition, the layer is perfectly formed.

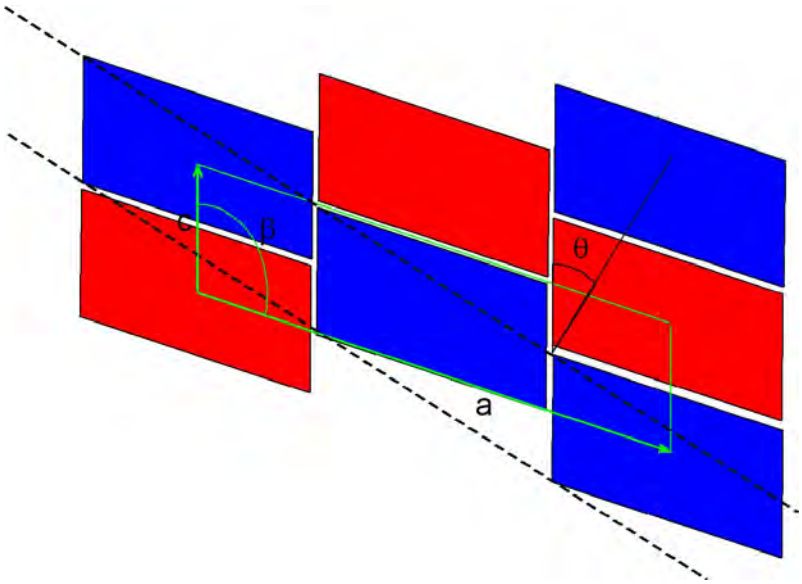

Fig. 45: Arrangement of the blocks in compound C. The centered cell is depicted as well as the pseudo-layer (dashed lines). The colors represent opposite polarization directions.

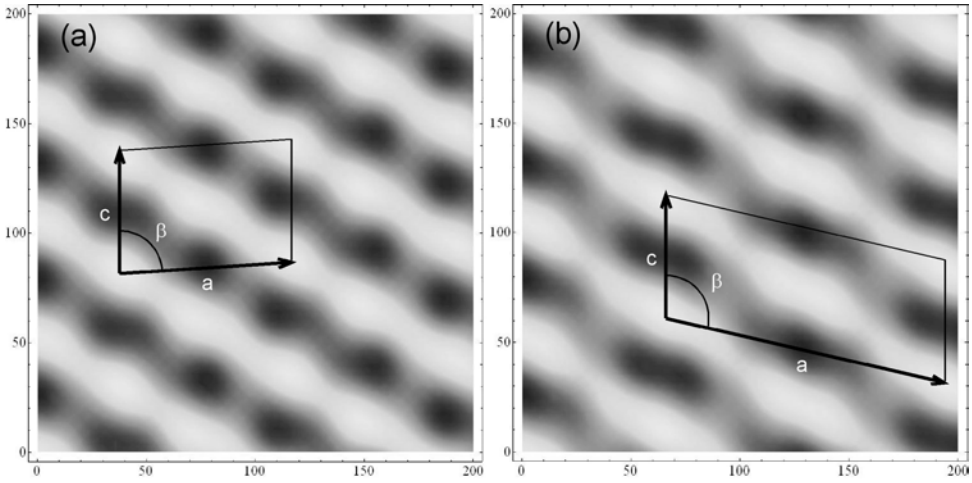

Fig. 46: Illustrative electron density diagrams of the columnar phases at the extremes of the temperature range, (a) at 143 ºC and (b) at 103 ºC. The lamellar character increases with decreasing temperature, as we approach the transition to the smectic phase.

The calculated layer spacing in the smectic phase is $d_{B2}= c\cdot\cos(\theta)$~46 Å, which compares prefectly with the experimental one (46 Å)

In these materials, the process leading to the smectic phase from the columnar one is different to that of compounds A and B, but still in the non-resonant X-ray diffraction centered cell the blocks in adjoining corners have opposite polarization directions, contrary to what is usually believed.

In conclusion, the classical structure for the B1 phase (see Fig. 10) has been discarded (at least in these cases) and, in its place, the structure shown in Fig. 47 is proposed. Cell 1 corresponds to the usually employed B1 cell. This is not an actual cell, but it can be used for interpreting non-resonant X-ray diffraction experiments since these are not sensitive to the polarization direction. The primitive cell for non-resonant X-ray diffraction is also depicted in the figure (cell 2). Finally, the real centered and primitive cells are 3 and 4 respectively in Fig. 47. The structure is monoclinic (β=90 ° is just a coincidence in compound A), and the symmetry group of the structure is P2/n. Using resonant X-ray diffraction, a direct evidence of how the molecules are arranged in the blocks can be obtained. This experiment is currently in progress.

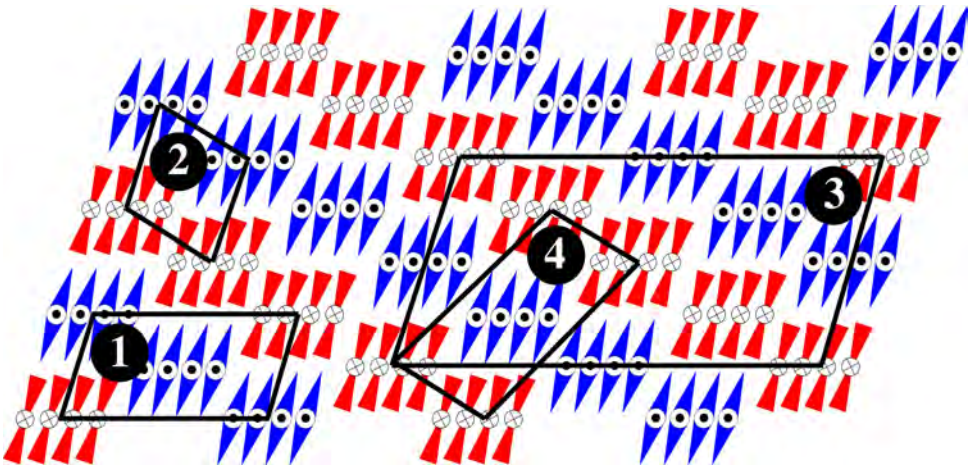

Fig. 47:Different cell choices in the B1 phase proposed. (1) and (2): Non-resonant X-ray diffraction centered and primitive cells respectively. (3) and (4): Resonant X-ray diffraction centered and primitive cells respectively.

Chapter 5

Desymmetrization and optically isotropic phases

The optical isotropy present in some of the bent-core liquid crystal phases (dark phases) together with the appearance of chirality domains (conglomerate), gives them the name of dark conglomerates (see Fig. 48). The various origins from which the optical isotropy, chirality segregation and optical activity could stem from in this kind of phases make them perfect candidates for the fundamental study of part of the interesting phenomenology of bent-core materials. The phases gathering these characteristics are: The B4[*], a soft crystal in which desymmetrization (see below) was firstly observed [63]; the B2[*] (dark conglomerates) (e.g. [64]); the B7[*] phase [65]; and it has even been suggested in the nematic phase of some bent-core compounds N[*] [66].

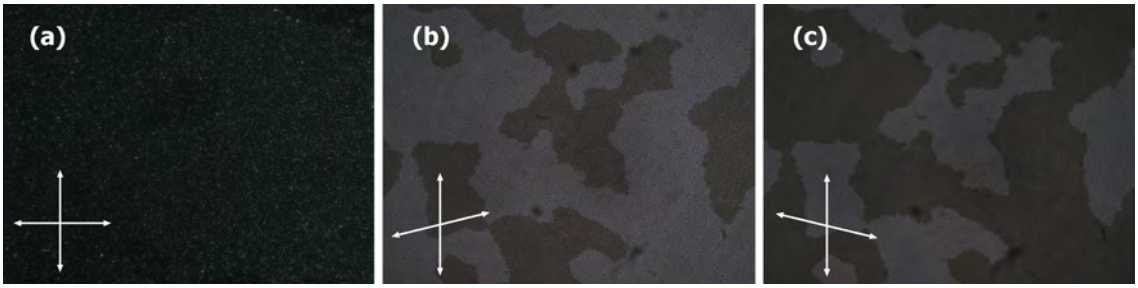

Fig. 48: Textures of a dark conglomerate phase: (a) between crossed polarizers; (b) and (c) chirality domains as seen uncrossing the polarizers in both senses due to opposite optical activity.

The spontaneous or induced segregation of macroscopic chiral domains (desymmetrization) is one of the most striking, interesting and studied phenomena of the physics of achiral bent-core liquid crystals. If birefringence is small, the existence of chiral domains of opposite handeness in a sample can be confirmed with the help of the polarizing microscope. Each domain has an optical activity that rotates the

polarization of the light passing through. Therefore, slightly uncrossing the polarizers, we will see contrast between domains of opposite sign (Fig. 48). The rotatory power of the sample can be estimated straightforwardly if the birefringence is small. Desymmetrization is not exclusive of optically isotropic samples, though it is in these cases where it is most easily observable. When the birefringence is not negligible other more complex methods must be employed to observe the desymmetrization: such as the observation of the behavior of the sample under field (looking at the rotation sense of circular [8] or striped [67] domains) or circular dichroism measurements [68]. It is worth mentioning the measurement of the optical activity by Hough et al [69][70] in the smectic phase of a bent-core compound (presenting birefringence). A correction to this work has been made recently [71].

The proportion of domains of opposite chirality in a sample is usually 1:1. However, adding chiral dopants [72] or using cells with treated surfaces [73], this balance can be broken and even a sample with a defined chirality can be obtained.

Why the chiral segregation process occurs and where chirality comes from are questions without a clear answer, despite intensive research. In this thesis various compounds possessing this kind of mesophases have been studied (B2[*] and B4[*]), and insights into the understanding of their structure and behavior have been achieved, digging a little bit more into the physics of these interesting materials.

The B4[*] phase.

The B4[*] phase was firstly observed in the P-n-OPIMB family of compounds [74] (see Fig. 50), which have become reference materials in the bent-core liquid crystal field. Not likely a fluid mesophase, the B4 phase seems to be some kind of soft crystal: In the X-ray diffraction diagram (see Fig. 53) a series of sharp peaks appear in the wide angle region (where a diffuse peak is expected for a genuine liquid crystal (as in Fig. 16). At low angles only one peak (and several harmonics) are present, giving a strong lamellar character to the structure. Comparing the layer spacing with the molecular length it is concluded that the molecules are not tilted. The full indexation of this X-ray diagram is not trivial and has been object of study in this thesis.

Another peculiarity of this phase is the presence of a blue color as background for the typical isotropic texture, recalling the blue phases. Sekine *et al.* [74] used this to propose a TGB (twist grain boundary) structure with the helix axis perpendicular to the surface of the cell which would cause selective reflection. Also Rayleigh light scattering superimposed on the absorption of molecules in the near-UV region was proposed to explain this phenomenon [75]. The existence of an helix has been proved by other means, for instance, electronic microscopy in freeze fractured samples showed a 250

nm helical pitch, in concordance with the color of the selective reflection [76]. The formation of the helix was attributed to an escape from a net macroscopic polarization due to a ferroelectric packing of the molecules in the ribbons (the long axis of the molecules was parallel to the helix axis).

This model with ordered helices was discarded by Ortega *et al.* in the basis of a clear independence of the selective reflection wavelength on the incidence angle [39], which suggested a random distribution of the helices in the sample. Moreover, although the B4[*] does not show any response to an external electric field, it does possess a remarkable SHG signal. This also rules out that the polarization of the smectic blocks is perpendicular to the helix axis. Taking into account these evidences it was suggested that the polarization in the blocks was parallel to the helix axis [77] (see Fig. 49).

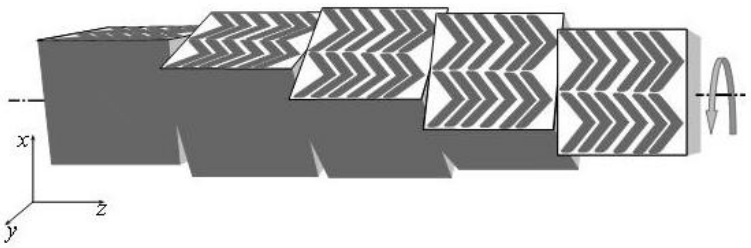

Fig. 49: Structure of the B4 phase proposed by Araoka et al. [77]. The laboratory reference frame is also shown.

Regarding the origin of the chirality in this phase, the first option to be ruled out is the layer chirality, because the molecules are non-tilted. NMR (nuclear magnetic resonance) studies [78] pointing towards a chiral conformation of the molecules, together with the fact that the helix formation is not due to an escape from the polarization, results in a very likely molecular origin for the chirality in the B4[*] phase. The formation of the TGB structure must be then caused by a coupling with the molecular conformational chirality.

Chiral molecular conformations are not stable in liquids (or ordered liquids) but, as stated above, the B4[*] has a strong crystalline character that can explain the stability. Desymmetrization processes in crystallizations are common and the highly compact packing of the molecules gives rise to a preference in the formation of chiral domains (molecules with the same handedness pack more efficiently). Surprisingly, a relationship between the chirality domains in the B4[*] phase and those of a B2 phase lying above (in temperature) is clearly observed. In the B2 phase, the conformations are not stable and a mechanism has been proposed coupling the chiral molecular conformation in the B4[*] with the tilt in the B2 phase [78].

In this thesis, new results have been obtained allowing for a deeper understanding of this phase. An aligned B4[*] domain has been obtained, which permitted a direct comparison of the SHG signal between the B2 and B4[*] phase, showing a huge

mismatch that could not be compatible with the current B4[*] models. On the other hand, an X-ray study has been undertaken. In this case, the focus has been on the indexation of the full diffraction diagram, from which the electronic density distribution has been also deduced and an local antiferroelectric structure is proposed. This structure explains the low SHG efficiency of this phase.

Structural study of two materials presenting the B4[*] phase

(Text adapted from [79])

The studied materials are P-n-OPIMB $(n=8, 12)$ from the already mentioned classical family of bent-core compounds, where the majority of the research on the B4[*] has been made in the literature (e.g. [39],[45],[80]). The chemical structure and phase sequence are depicted in Fig. 50.

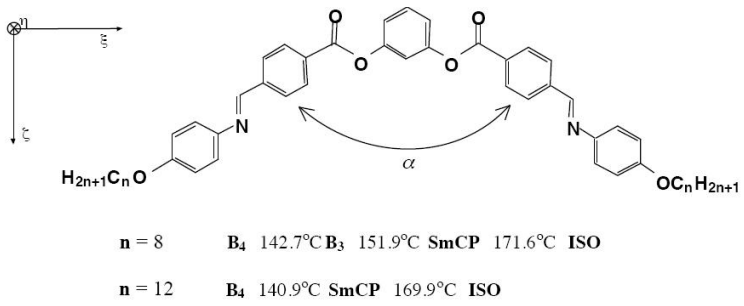

Fig. 50: Molecular structure and phase sequence of P-8-OPIMB and P-12-OPIMB together with the reference frame of the molecule. The temperatures correspond to those obtained by DSC on cooling.

Fig. 51 shows the general characteristics of the B4[*] textures in two different samples of P-12-OPIMB. The textures are dark under crossed polarizers (Fig. 51a and c) and chiral domains are visible when slightly uncrossing the polarizers (Fig. 51b and d). However, it must be pointed out that there are differences depending on the thicknesses, aligning agents and thermal history of the different samples. For example, Fig. 51a presents an almost perfect isotropic phase (EHC planar cell of 7 μm thickness). In contrast, the texture of Fig. 51c exhibits much more birefringent domains embedded in an isotropic dark background (Linkam planar cell of 5 μm thickness). It is not easy to deduce a general rule to predict the amount of birefringent inclusions in the different samples. However, there exists a clear correlation between the proportion of inclusions and the SHG signal detected in the samples, i.e., the more birefringent domains, the higher the SHG signal.

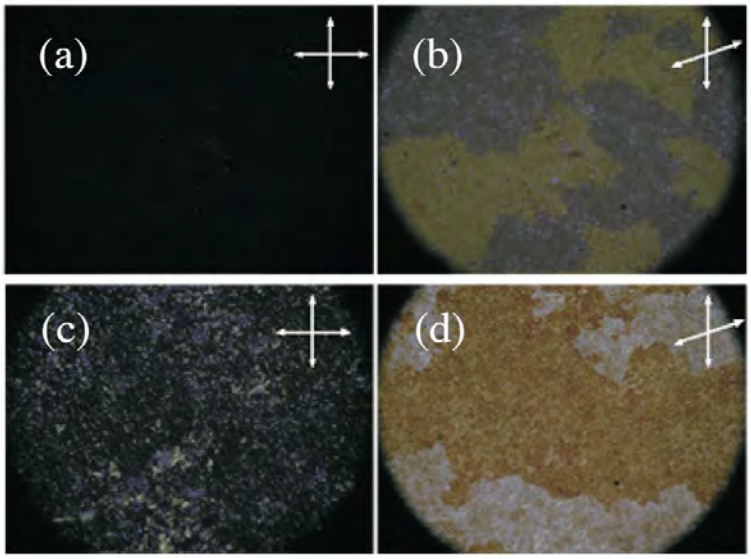

Fig. 51: B4 phase textures in two different samples of P-12-OPIMB. (a) and (b) were obtained in a commercial 7μm thick EHC cell, and (c) and (d) in a 5 μm thick Linkam cell. The textures under crossed polarizers, (a) and (c), show different amount of birefringent inclusions. Slightly uncrossing the polarizers chiral domains are easily observable in both samples ((b) and (d)). All photos are 500 μm wide.

These correlations can be explained assuming that the B4[*] phase is intrinsically SHG active but mainly consists of domains of a mesoscopic scale and randomly distributed. Under this scheme the birefringence would essentially vanish as a consequence of the averaging. Only a small proportion of the domains would be macroscopic, giving rise to the birefringent inclusions embedded in the dark texture. These domains are also responsible of the SHG signal.

Home-made cells with in-plane electrodes and no surface treatment were also prepared. By applying an electric field of 15 $V\mu m^{-1}$ parallel to the substrate in the SmCP phase, it is possible to align the material. This strategy has been reported to be successful by different authors in SmCP phases [30][37][45][81][82]. Surprisingly, after cooling down into the B4 phase a previously aligned SmCP sample under DC field the alignment remained. Fig. 52 shows the texture of the sample between crossed polarizers. As can be seen, a good quality alignment has been obtained between the electrodes. Fig. 52a indicates that the principal directions of the optical indicatrix are set along the electric field direction and its perpendicular. In Fig. 52b the sample has been rotated about 45°. The texture shows a grey colour, which implies a birefringence $\Delta n = 0.02$ (sample thickness 5 μm). This value is compatible with the currently available model for the B4 phase proposed in Ref. [77] (see Fig. 49) if the TGB axis is arranged along one of the principal axes (presumably the electric field direction). In fact by modeling the molecule as two uniaxial wings with ordinary and extraordinary refractive indices $n_o = 1.5$ and $n_e = 1.7$ respectively and, with a bending angle $\alpha = 120^\circ$,

the birefringence value of a smectic layer can be obtained. The optical indicatrix of the TGB structure can be deduced by averaging about its helix axis the dielectric tensor corresponding to the constituent smectic blocks filled with non-tilted molecules. Under this scheme a theoretical birefringence value $\Delta n = 0.026$ is obtained, which is in good agreement with the experiment. It must be pointed out that it is the first time that the B4[*] phase has been aligned. The result is remarkable and implies that the B4 phase is not intrinsically isotropic but can appear with different domain patterns. Previously, Thisayukta *et al.* [83] obtained in this material a large spherulite domain in the B4[*] phase after cooling down a sample previously aligned homeotropically in the SmCP phase. However, in our case, order has been obtained in a given direction since the helix axis is parallel to the applied electric field in the whole sample.

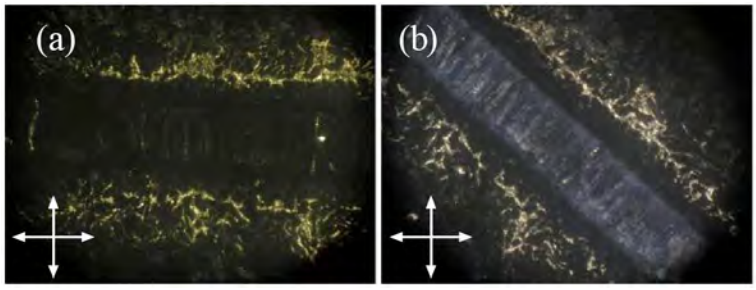

Fig. 52: Aligned domain obtained cooling a sample of P-12-OPIMB from the B2 phase into the B4 phase with a large in-plane DC field. (a) shows the extinction of the domain along the polarizer directions. (b) shows the same domain rotated 45° (photos are 500 μm wide).

In order to ascertain the structure of Fig. 51 it is interesting to calculate the second order susceptibility tensor corresponding to this structure. Assuming the model proposed by Araoka *et al.* [38] the SHG signal is mainly driven by the longitudinal molecular hyperpolarizability along the lateral wings of the molecules (see Chapter 2, page 20). The obtained second order susceptibility tensor in the xyz frame of Fig. 49 is given by:

$$\mathbf{d} = \begin{pmatrix} 0 & 0 & 0 & 0 & D/2 & 0 \\ 0 & 0 & 0 & D/2 & 0 & 0 \\ D/2 & D/2 & d & 0 & 0 & 0 \end{pmatrix}$$

According to the above expression the SHG signal corresponding to a macroscopic domain of the B4 phase must be of the same order of magnitude as that of a $SmCP_F$ phase [37]. In fact, the obtained **d** tensor is equal to that of a SmC_AP_F structure with a tilt angle of 45° and perfect molecular order (see tensor (7) in pg. 21). To check this theoretical result we carried out SHG measurements in the oriented sample of Fig. 52 at normal incidence in different configurations: polarizer and analyzer set parallel or perpendicular to each other and to the helix axis. It seemed reasonable to expect similar SHG signals in this phase and in the SmCP phase under electric field. However, the

efficiency in the SmC_AP_F resulted to be higher in two orders of magnitude than that of the B4 phase. This fact unambiguously indicates that the aligned region of the sample cannot be a ferroelectric TGB domain as depicted in Fig. 51.

In order to clarify this question we carried out X-ray measurements in the B4 phase of both materials at small and wide angles. Fig. 53 shows the X-ray patterns in the B4 phase for both the P-12-OPIMB (orange symbols) and P-8-OPIMB (green symbols). No appreciable changes were found at different temperatures within the B4 phase. Black symbols represent the corresponding data for the P-12-OPIMB in the SmCP phase. In the B4 phase both compounds exhibit, at small angles, several peaks (blue arrows in Fig. 53), which correspond to different harmonics of a given periodicity compatible with the layer spacing. In both compounds the obtained values imply a non-tilted structure taking into account their molecular lengths in the most extended configurations. As expected the layer spacing of the P-12-OPIMB is larger than that of the P-8-OPIMB due to its larger aliphatic chain. In both compounds harmonic reflections $(00l)$ are visible up to $l=6$, indicating well-formed layers. Remarkably, some of these reflections are missing ($l=4, 5$ for P-8-OPIMB; $l=3, 4$ for P-12-OPIMB). Their widths are not resolution limited, indicative of short-range local lamellar order.

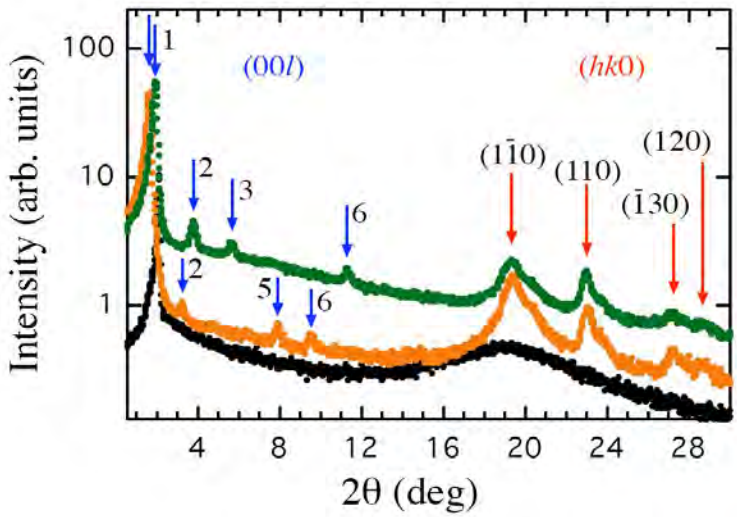

Fig. 53: X-ray diffraction patterns of the B4 phase of P-8-OPIMB (green) and P-12-OPIMB (orange) and the B2 phase of P-12-OPIMB (black). The indexation for the main peaks of the B4 phase is shown. Numbers corresponding to the blue arrows indicate the l value of the (00l) reflections.

At wide angles the broad diffuse maximum characteristic of the SmCP phase splits into 4 different main peaks (red arrows in Fig. 53). In both cases, the diagram for the wide-angle region is similar to the reported by Pelzl *et al.* for the B4 phase of P-8-OPIMB [75]. These reflections are not harmonic of the small angle ones, indicating that other

periodicities are present apart from the smectic ones. In addition the shapes of these peaks show the contribution of other weaker reflections. As can be seen in Fig. 53 the angular position of the four peaks almost coincide in both compounds. This fact can be understood if these peaks are indexed in the form $(hk0)$ since the condition $l \neq 0$ would imply a different angular position, as the smectic layer length is different in both compounds. Fig. 54 shows a magnification of the interval $2\theta = 26^{\circ} \leftrightarrow 30^{\circ}$ for P-12-OPIMB where a repetition of the measurement at the same temperature (open squares in Fig. 54) was performed in order to corroborate the existence of the weak reflection indexed as (*120*). P-8-OPIMB and P-12-OPIMB present a similar indexation scheme. In both cases the structure is monoclinic with the monoclinic c axis perpendicular to the smectic layers. The indexation parameters are $a = 4.64\,\text{Å}$, $b = 11.34\,\text{Å}$, $c = 55.86\,\text{Å}$ and $\gamma = 104.36^{o}$ for P-12-OPIMB and $a = 4.67\,\text{Å}$ $b = 11.35\,\text{Å}$, $c = 47.03\,\text{Å}$ and $\gamma = 104.26^{o}$ for P-8-OPIMB. Since the phase is monoclinic and chiral the only possible point group is C_2, with the twofold axis along the smectic layer normal. Furthermore, assuming that the molecular dipole moments are contained in the smectic layers (as in any lamellar phase), then they are perpendicular to the twofold axis and, therefore, the obtained point group is only compatible with an antiferroelectric structure.

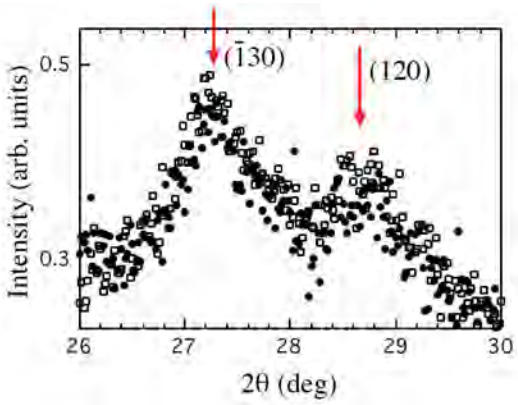

Fig. 54: Magnification of the interval 2θ = 26° - 30° for P-12-OPIMB. Solid circles and open squares represent two successive measurements at the same temperature that were performed in order to make clear the existence of the weak (120) reflection.

In order to clarify the structure inside the layer we have analyzed the electron density distributions that correspond to the four wide-angle main peaks $(hk0)$ of P-12-OPIMB. The method is explained in Chapter 2. There are 4 $(hk0)$ reflections, and therefore, in principle, 2^4 distinct sets of sign combinations for the Fourier components $F(hk0)$ of the charge density. However, among the sign sets, only 4 different charge density maps are actually obtained, since the rest only represent a shift in the origin of the map plot.

This is because the sign of $F(1\bar{1}0)$ and $F(120)$ can be fixed arbitrarily, something equivalent to select the origin of the unit cell in one of the four twofold axes located at $(0,0,0)$, $(\frac{1}{2},0,0)$, $(0,\frac{1}{2},0)$ and $(\frac{1}{2},\frac{1}{2},0)$ (see Fig. 55). In fact, $F(hkl)$ transforms into $(-1)^{hn_1+kn_2+ln_3}F(hkl)$ when the origin is changed to $\frac{n_1}{2}\boldsymbol{a}+\frac{n_2}{2}\boldsymbol{b}+\frac{n_3}{2}\boldsymbol{c}$ and, consequently, there is a different combination of the signs of $F(1\bar{1}0)$ and $F(120)$ for each one of the possible origins (+ +, − −, − + and + − respectively). Therefore, the different charge density maps are given by the 4 possible sign combinations of $F(110)$ and $F(\bar{1}30)$.

From the independent set of signs, the combination (+ − + +) (signs correspond to the peaks ordered in increasing angular position) has been selected on the basis of molecular packing criteria. The resulting electron density map is depicted in Fig. 55.

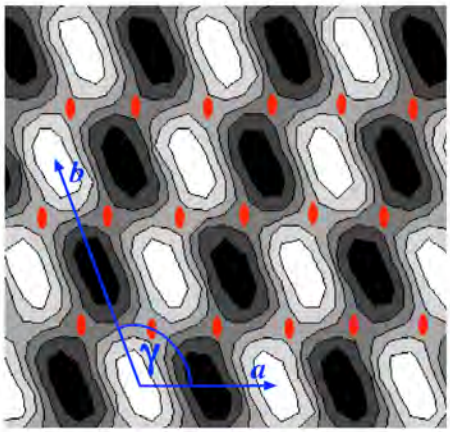

Fig. 55: Two-dimensional electron density map (ab projection) of P-12-OPIMB obtained from the X-ray intensities of the four main (hk0) reflections. The unit cell is depicted together with the twofold axes (red).

In order to investigate how the molecules are packed, we first try to find how many there are in a unit cell. We will use crystal volume increments [84] to evaluate the theoretical density in the solid. For example, for P-12-OPIMB, the theoretical molecular volume in the solid is $V_{mol,sol}=1281\,\text{Å}^3$ and the density $\rho_{sol}=1.156\,g\,cm^{-3}$, obtained by assuming an average packing coefficient $K=0.7$ [85]. In the isotropic liquid the volume per molecule is $V_{mol,is}=1630\,\text{Å}^3$ and the density $\rho_{is}=0.908\,g\,cm^{-3}$, obtained with $K=0.55$ [85]. The average density (more appropriate for the B4 structure) is then $\rho=1.032\,g\,cm^{-3}$. Now, if we assume 2 molecules in the cell this density compares very well with the value deduced from the measured unit cell volume $V_{cell}=abc\sin\gamma$, giving $\rho=1.039\,g\,cm^{-3}$. The presence of 2 molecules per 3D cell also implies 2

molecules per each cell of the projected structure shown in Fig. 55. Thus each high-density region in that figure must correspond to one molecule.

The structure is mainly determined by the packing requirements of the cores inside the layer. Typically, banana compounds pack inside the layers with ferroelectric order. Therefore the antiferroelectric character of the B4 phase should be due to a 2_1 screw axis along the layer normal. In other words, the polarization would alternate from layer to layer. However, this structure would imply a centered Fourier map characteristic of compact packing (see Fig. 55). Although the density map indicates an almost centered structure, it is not rigorously true since the X-ray diagram presents the $(1\,2\,0)$ reflection. In order to overcome this contradiction, we propose the structure presented in Fig. 56a. The corresponding space group is *P*2. Fig. 56b represents a view of the ***bc*** plane. In both figures, regions where the projection of the electron density on the ***ab*** plane contains the superposition of two adjacent molecules are indicated in yellow. These correspond to the white regions of the Fourier map in Fig. 55. It must be remarked that the antiferroelectric ordering inside the layer is compatible with efficient molecular packing since molecules with opposite direction of the dipole moment do not undergo unfavorable steric interactions due to the true crystalline arrangement of the molecules in this phase.

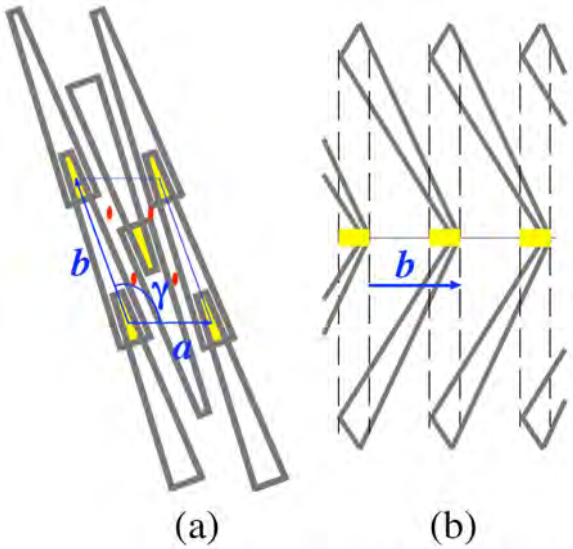

Fig. 56: Schematic view along the c-axis of the in-layer molecular arrangement proposed for the B4 phase (a) and a view along the direction perpendicular to the bc plane (b). The twofold axes are depicted in red and the unit cell is highlighted in blue. In both figures the superposition of two adjacent molecules is indicated in yellow.

In addition, the proposed structure allows to explain the optical properties of this phase. On the one hand, the optical dielectric tensor of that structure is identical to that of the ferroelectric arrangement. Therefore, assuming a TGB axis close to the polar direction, as in the model proposed by Araoka *et al.* in Ref. [77], both structures result to be optically equivalent. Consequently the agreement between the experimental and calculated birefringence values for the sample of Fig. 52 remains valid in this new structural scheme. On the other hand, now it is possible to account for the low SHG efficiency that this phase presents. The symmetry of the proposed structure allows the existence of SHG since, taking into account the conformational chirality of the molecules [86][87][88][89][90] that exclude the existence of a mirror plane perpendicular to the twofold axis, the symmetry space group is *P2* (Fig. 56a). However, the SHG efficiency is expected to be small as the molecules are antiferroelectrically arranged and, therefore the nonlinear response of the structure is expected to be greatly reduced.

Finally, the analysis developed here indicates unambiguously that each one of the TGB blocks of the B4 phase is a 3D crystal structure, and not a lamellar arrangement with a mere in-plane order as commonly believed. In this sense, although according to Ref. [90] the molecular chains of successive layers melt forming liquid-disordered planes parallel to the smectic layers above and below the cores, these chain regions should permit a correlation transfer between the positions of cores in adjacent layers. Otherwise the wide-angle reflections should not be visible. This can be easily seen taking into account that the lack of correlation works mathematically as a kind of Debye-Waller factor that in our case results in $2\mathrm{M} = 4\pi^2 S_{\|}^2 \langle u_{S_{\|}}^2 \rangle$. This quantity reduces the reflections intensities a factor $e^{-2\mathrm{M}}$ (equivalent to the temperature factor). In the above expression $S_{\|}$ is the component of the diffraction vector parallel to the ***ab*** plane and $\sqrt{\langle u_{S_{\|}}^2 \rangle}$ is the square mean value of the displacements in the direction of $S_{\|}$. In our case

$$S_{\|} = \frac{1}{\sin^2 \gamma} \left[\frac{h^2}{a^2} + \frac{k^2}{b^2} - \frac{2\mathrm{hk}}{ab} \cos \gamma \right]$$

and the following values result, for example, for the temperature factor of the $(1\bar{1}\,l)$ reflections when small displacements are considered:

$\sqrt{\langle u_{S_{\|}}^2 \rangle}$	$e^{-2\mathrm{M}}$
1 Å	0.153
1.5 Å	0.0147
2 Å	0.00055

According to this result, the intensity of the strongest $(1\bar{1}\,0)$ reflection would be

drastically reduced if the lack of correlation between layers involves displacements larger than about 10% of the cell parameters. In Fig. 57 we can see diffraction diagram for P-12-OPIMB corrected for the Lorentz factor. The size of the peaks in the wide angle region is noteworthy, being the peaks at larger angles even higher than the first harmonic of the layer spacing. It is not likely that these peaks are reduced by large factors as those calculated above. Hence, it seems that the layers are indeed correlated.

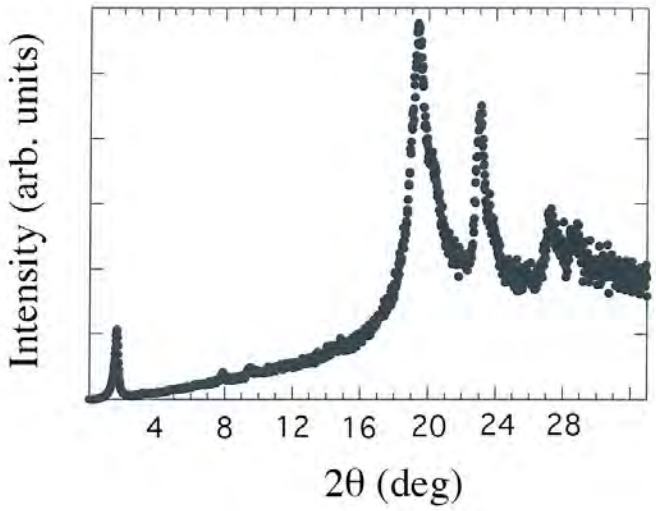

Fig. 57: Diffraction diagram for P-12-OPIMB corrected for the Lorentz factor.

As a conclusion of this study of the B4[*], results of texture observations, SHG and X-ray diffraction measurements point towards a TGB structure with antiferroelectric arrangement of the molecules inside the layer. We have prepared an aligned sample with the helix axis parallel to the substrate, whose birefringence indicates that the TGB axis in the B4[*] phase is expected to be close to the polar axis. On the other hand, the low SHG efficiency measured in that sample is compatible with the proposed structure, whose symmetry allows the existence of NLO response but the antiferroelectric arrangement of the molecules results in a low SHG performance.

Optical isotropy and chirality in the B2[*] phase.

In contrast to the B4[*] phase, the B2 phase does not possess positional order inside the layers and its liquid crystallinity is well defined. The X-ray diffraction diagram is simple and it presents: a single reflection at low angles (and maybe some of its harmonics); and a diffuse reflection at higher angles, due to the in-plane disorder (see Fig. 16). This X-ray diffraction pattern usually corresponds to birefringent textures, but some optically isotropic mesophases also show it.

The origin of the optical isotropy is not straightforward and several proposals can be

found in the literature. The easiest explanation describes the phase as randomly distributed microscopic domains (smaller than the optical wavelength) that average their contribution to the index ellipsoid [91]. It has also been suggested that if molecules are arranged in a SmC_AP_A fashion and the tilt is close to 45°, the birefringence should be really small. In fact if the tilt angle θ and the molecular bending angle α of the banana follow the relation $\alpha = 2\tan^{-1}(1/\cos\theta)$, Δn is exactly zero [92].

The width of the smectic peak is not resolution limited, so there must be some kind of frustration in the formation of the layers. Moreover, the impossibility to obtain aligned samples suggests that the disorder is intrinsic to this type of dark mesophases. Freeze fracture experiments [93] showed that the smectic layers are strongly curved, giving rise to structures similar to the ones of the L3 phases in lyotropic liquid crystals [94]. The coherence length for flat layers is smaller than the optical wavelength, explaining the optical isotropy.

It has been demonstrated theoretically by DiDonna *et al.* [95] that this kind of structures can indeed be stable (comparing with the formation of flat layers) if the value of the so-called saddle-splay elastic constant of the material is negative enough.

Where the frustration in the formation of the flat smectic layers giving rise to such a disordered phase stems from is not clear and three different causes have been given:

- Steric reasons: The molecules cannot accommodate well in a flat layer because excluded volumes would give rise to a highly inefficient packing. This is due to the different cross-section areas required by different molecular segments.
- Escape from a macroscopic polarization (in the case of a ferroelectric phase).
- Molecular conformational chirality.

In this thesis, a material presenting two optically isotropic phases (a conglomerate and a racemate) depending on the field treatment has been studied. Using electro-optic and SHG measurements, it has been concluded that, at least in this case, the steric reasons are responsible for the frustration in the flat layer formation.

Study of a material showing the B2[*] phase

(text adapted from [64]).

The chemical structure of the material and the phase sequence in the absence of field are shown in Fig. 58. The synthesis and a preliminary characterization of the compound was published in [96]. Also, previous dielectric and optical studies were reported in Refs. [97] and [98] respectively.

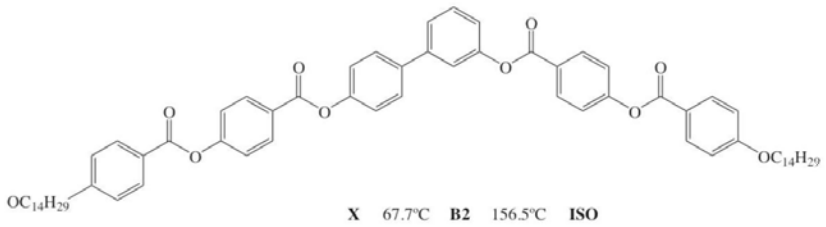

Fig. 58: Chemical structure and phase sequence on cooling of the studied material.

Cooling the sample from the isotropic phase the texture of Fig. 59 is obtained. The X-ray diffraction diagram and the extinction brushes at 45º with respect to the polarizer directions indicates a SmC_SP_A structure. Fig. 60 shows the optical textures at T=146 °C after cooling the material from the isotropic phase under a strong square-wave field (12 $V\mu m^{-1}$, 10 Hz) and its subsequent removal. The dark phase with the chiral domains is clearly visible by slightly uncrossing the polarizers (Fig. 60a and b). On further application of the field the texture (Fig. 60c) becomes highly birefringent $(\Delta n = 0.14)$. This indicates a SmC_SP_F structure.

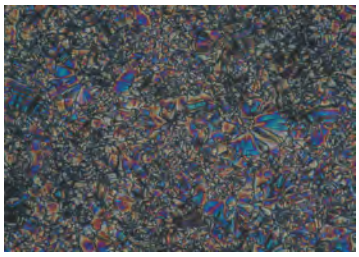

Fig. 59:Texture of the material when cooling from isotropic.

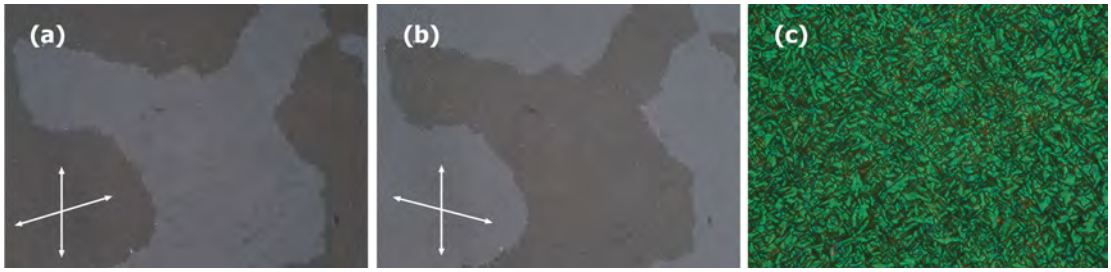

Fig. 60: Homochiral dark conglomerate phase. Textures observed 10º below the transition temperature after cooling from the isotropic phase under a square-wave electric field ($12V\mu m^{-1}$, 10Hz). After field removal, domains of opposite chirality can be clearly seen slightly uncrossing the polarizers, as show in (a) and (b) (600 μm wide). Picture (c) (240 μm wide) shows the texture with the field on ($12V\mu m^{-1}$).

A different behavior results if the field is applied after cooling the material into the normal SmCP phase. In this case, again, a dark texture is obtained after field removal (Fig. 61a) but now there are no chiral domains (dark racemate). Furthermore, the texture aspect after a subsequent field application (Fig. 61b) is clearly different to that

of the preceding case. The most abundant color of the photograph corresponds to a small birefringence (about $\Delta n = 0.06$). Sometimes a variety of colors can be found, indicating inhomogeneous birefringence. The interpretation of this texture is not easy.

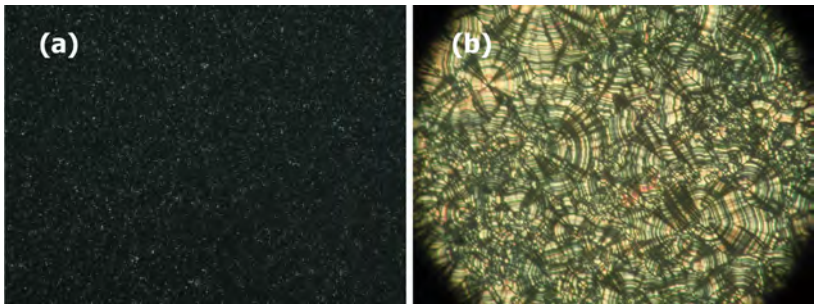

Fig. 61: Racemic dark phase. Textures observed at 10ºC below the transition temperature after cooling from the isotropic phase and then applying a square-wave electric field (15 Vμm^{-1}, 10Hz): (a) (1200μm wide) after field removal; (b) (250μm wide) under a field of 8 Vμm^{-1}.

As can be seen, the texture exhibits circular domains with extinction brushes rotated 45° with respect to the polarizers direction. This fact rules out the possibility of a simple racemic anticlinic structure (SmC_AP_F). However, the birefringence is smaller than that corresponding to a synclinic state. A possible explanation of this fact could be made in terms of an unbalanced arrangement of chiral domains (SmC_SP_F) of both hands along the sample thickness. In fact, in a first approximation, the birefringence should be smaller since the indicatrix of the adjacent domains of opposite chirality approximately alternate their fast and slow axes due to the proximity of the tilt to 45° [98]. Under this model the sample could be considered, form an optical point of view, as a synclinic structure of smaller birefringence and, therefore, the brushes of the circular domains should appear rotated 45°. The birefringence value must be roughly the enantiomeric excess proportion multiplied by the birefringence of the homochiral structure $(\Delta n = 0.14)$. The domains with birefringence $(\Delta n = 0.06)$ should be composed of a proportion of different chiralities 70:30%.

Another possibility to explain the texture of Fig. 61b is in terms of a kind of imbalanced $[SmC_SP_F]_aP_F$ domains see Fig. 62 (using the nomenclature of [21] and explained in the caption). If in a wavelength of visible light the number of layers of opposite tilt were balanced, the birefringence would be almost null (recall that the tilt angle is close to 45º). This configuration of the layers would explain the dark rings present in the circular domains (Fig. 61b). If there is an imbalance, the birefringence would rise, but the brushes would still appear at a 45º angle. Since this imbalance is not expected to be large in the distances of interest, the birefringence would never get to the values of the synclinic state. This can explain the yellow domains $(\Delta n = 0.06)$ and the pinkish ones (with a slightly higher Δn).

A comment must be made regarding the dark state corresponding to this texture. If the

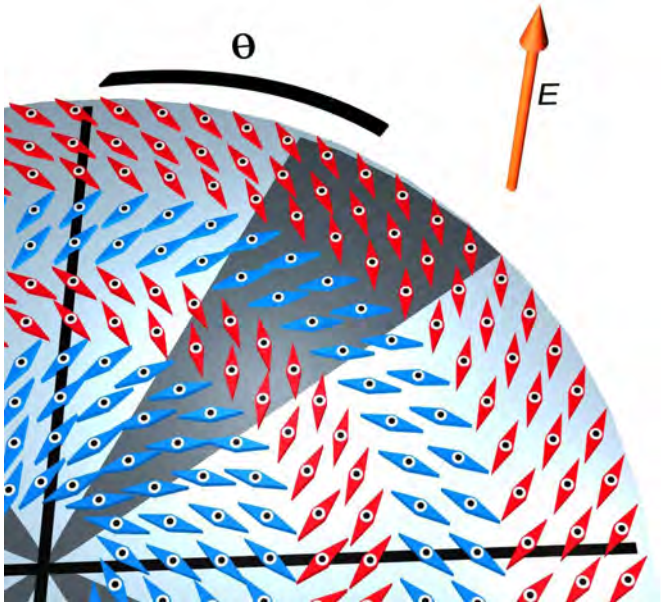

Fig. 62: Imbalanced $[SmC_SP_F]_aP_F$ domains. The basic structure is between square brackets; the first subindex indicates the type of clinicity between adjacent stacks and the next one the polar correlation.

proportion of different chiral domains remained after field removal, the optical activity should be about 40% of that of the chiral dark state of Fig. 60 and, therefore, gyrotropic domains should be easily observed taking into account our experimental resolution. However, this is not the case since the dark state (Fig. 61) is optically inactive. This fact would imply a reversible field-induced chiral segregation in this material.

The existence of a racemic variant of the optically isotropic state means that the electric field is not able to segregate irreversibly the different chiralities from the (presumably racemic) SmCP initial structure (see Fig. 59). This behavior contrasts with the obtained on cooling the isotropic liquid under field. However, in both cases a dark phase has been induced by the field treatment. An important conclusion can be deduced from these observations: at least in our compound, chirality (supramolecular or conformational) does not play any relevant role in the generation of the dark phases. This is in agreement with the theoretical model of Ref. [95] where chirality is not necessary to induce the curvature of the flat smectic layers. It is not easy to explain why the chiral domains are separated if the field is applied in the isotropic phase. Probably in the isotropic phase there already exist some clusters of molecules with definite supramolecular chirality (cybotactic groups) segregated by the action of the field. However, the chirality segregation is less efficient and reversible if the field is applied to an already condensed racemic mesophase. A possible mechanism driving the chirality segregation was proposed by Pyc *et al.* [99], and is based on the change of chirality of layer regions by molecular rotations about their long axes. It seems that in

our material this mechanism is completely effective only when the layers are being formed from the isotropic phase. Although the presence of an electric field is necessary to induce the dark phases, once they are formed, they remain stable without any sign of relaxation into the normal SmCP phase, at least for time periods about 60 h.

An important point to be clarified in this material is what the structure of the dark phase at a microscopic scale is. According to X-ray measurements the molecules form a tilted lamellar structure [96]. However, determining the type of polar arrangement of the phase (ferroelectric or antiferroelectric) is not trivial due to the distortion of the structure that the material presents at a mesoscopic scale. In this respect, several experimental results pointing to a ferroelectric ground state have been reported up to now but none of them can be considered as conclusive.

A short-pitch ferroelectric helical structure was proposed by Etxebarria et al [98] on the basis of the observation of a deformed helix regime under a triangular-wave electric field. In that work, it was assumed a macroscopic domain size in which the optical isotropy was achieved by averaging the dielectric tensor for all the azimuth angles of the molecular director due to the short pitch proposed for the helix [98]. However, in this compound a racemic variant of the dark phase appears, wherein helical arrangements cannot be justified. Therefore, the isotropic texture shown in Fig. 61a cannot be explained assuming a macroscopic domain size.

According to Diez *et al.* [97] the polarization-current response, under a triangular-wave electric field, presents two main peaks per half period, as is the case in an antiferroelectric arrangement. The measured value of the polarization is 900 $nCcm^{-2}$. However, as also reported in that work, this behavior is in contrast with the high values of the dielectric strength of the dominant mode $(\Delta\varepsilon \approx 70)$, which suggests a ferroelectric structure. A short-pitch ferroelectric helical structure was also proposed by the authors to make both results compatible. Recently, however, Pociecha *et al.* [100] have shown that an intense dielectric mode (antiphase phason mode) exists in antiferroelectric smectic phases with weak antiferroelectric interaction (such as bent-core liquid crystals) and significant quadrupolar interlayer coupling. In addition, the predicted profile for the dielectric strength of this mode vs. bias field is similar to that reported for this compound in Ref. [97].

The assumption that the dark phase is a disordered sponge-like phase in which the coherence length of the smectic arrangement is mesoscopic, seems to be compatible with all the experimental observations. However, the dipole ordering between adjacent layers in the ground state of the structure is not clarified yet. With that purpose, a comparison study between the switching dynamics of the SHG signal and the light transmission between crossed polarizers was carried out. The idea for that study is as follows. It is well known that for typical materials possessing dark phases the characteristic relaxation time to the dark state after the removal of an electric field is

much longer than the times involved in the ferroelectric switching [91][92][101][102] [103][104][105]. Therefore, if the phase presented antiferroelectric order, a difference between both characteristic times should arise that, in principle, could be detected. SHG and light transmittance measurements were carried out, after a sudden electric field removal, in order to measure both characteristic times. Measurements were carried out both in the homochiral and racemic variants of the dark phase.

Commercially available (Linkam) 5 μm thick cells were used to prepare the samples for both experimental techniques. The SHG setup with a Nd:YAG laser has been described in Chapter 2 (SHG setup I). A periodic stepwise electric field (see Fig. 63a), synchronized to the laser trigger, was applied perpendicular to the sample substrates with 20 $V\mu m^{-1}$ step amplitude. The sample was positioned at oblique incidence making an angle of 35° with respect to the laser beam. Fig. 63b and c show the SHG intensity versus time both for the homochiral and racemic phases respectively at 146°C, for the falling part of the step electric field. By monitoring the 90%-10% fall-times 60 μs and 100 μs were obtained for the homochiral and racemic phases respectively.

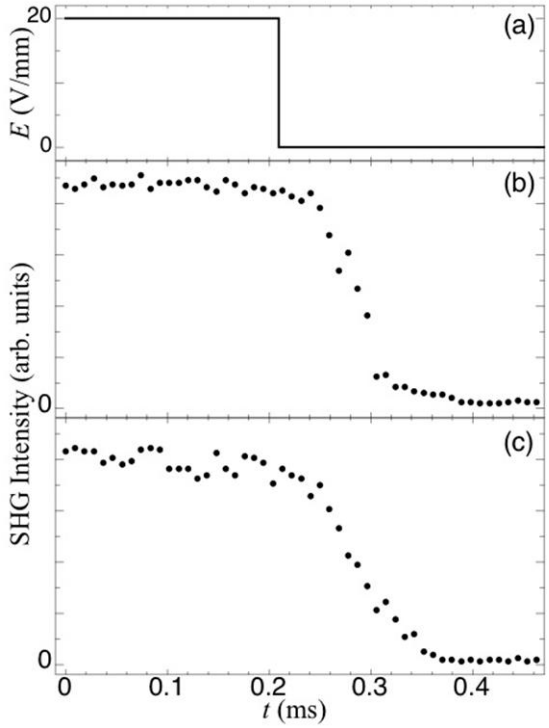

Fig. 63: SHG measurements as a function of time performed under the electric field depicted in (a) at 10ºC below the clearing point. The 90-10% fall times were obtained for the homochiral (60 μs) and racemic (100 μs) phases from (b) and (c) respectively.

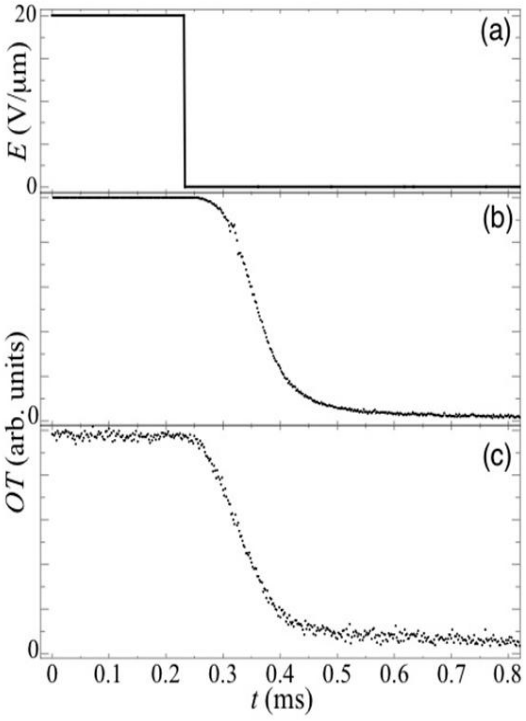

Fig. 64: Optical transmission measurements as a function of time performed under the electric field depicted in (a) at 10ºC below the clearing point. The 90-10% fall times were obtained for the homochiral (130 μs) and racemic (170 μs) phases from (b) and (c) respectively.

The light transmittance experiments were carried out using a polarization microscope. The light intensity was detected using a photodiode connected to an oscilloscope. Fig. 64b and c represent the transmitted intensity versus time under crossed polarizers for the homochiral and racemic phases respectively at the same conditions of temperature as in the SHG experiment and under a 20 $V\mu m^{-1}$ electric field. Using the same strategy to obtain the fall-times, the obtained values were 130 μs and 170 μs for the homochiral and racemic phases respectively. The fall-times for both the SHG and transmittance experiment were checked to be independent of the intensity of the applied electric field in all the cases.

According to the results, it can be stated that the material is antiferroelectric in both variants of the dark phase since the fall-times characteristic of the SHG measurements are shorter than those of the light transmittance. This fact implies a faster process for the switching from the ferroelectric to the antiferroelectric states than the time required for the structure to relax to the dark state.

It should be pointed out that in this compound the relaxation to the dark state, which implies a layer distortion at a mesoscopic scale, is extremely short in comparison to the standards in bent-core compounds [91][92][101][102][103][104][105]. And more remarkably, unlike other materials with dark textures, the effect is reversible, i.e., if the field is switched off, the dark texture reappears. This fact is used in Chapter 6 to propose an LCD mode using this material. Another important conclusion that can be drawn, at least for this compound, is that the layer distortion characteristic of the dark state is not driven by the escape of the polar order, since the ground state is antiferrolectric. As a consequence it seems reasonable to assume that this distortion is due to steric reasons. However, the threshold electric field that must be applied in the isotropic phase (homochiral case) or the virgin SmCP phase (racemic case) to provoke the dark state can be understood as a promoter that enhances the steric interaction probably due to higher order induced inside the layer.

As a complementary measurement, in Fig. 65 shows the SHG intensity for both phases when the material is subjected to a bipolar triangular wave of 30 Hz. The rest of the conditions are the same as in the above SHG measurements. These curves are a measure of the polarization response of the material, since, roughly, the SHG signal should be proportional to the polarization squared. Therefore they can be considered as an alternative to the most common polarization current method [106] for studying the switching dynamics.

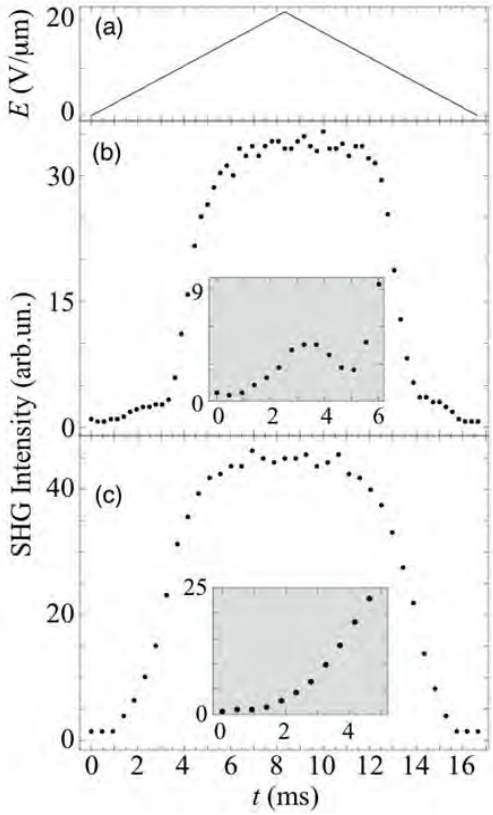

Fig. 65: SHG signal as a function of time performed under the 30Hz triangular wave shown in (a) at 10° below the isotropic transition, for (b) homochiral and (c) racemic phase. In the inset (wave amplitude 12 Vμm^{-1}) the bottom of the main peak is detailed to highlight the anomalous behavior in the homochiral phase. The scale used for the SHG intensity is the same in all graphs.

Surprisingly, whereas the observations are as expected for the racemic sample, the dynamics in the appearance and disappearance of the SHG signal in the homochiral structure occurs through an unexpected two-step process. The existence of two mechanisms is especially evident (see the inset in Fig. 65b) if the applied voltage is not high enough to reach the SHG saturation. Under the action of the step-wave field the second small hump can also be seen in Fig. 63b. This behavior is perfectly reproducible at different temperatures and illuminating different sample areas. In contrast, the switching of the racemic samples always takes place in a single process. Thus it seems that chirality is in some way involved in the explanation of the difference. One can speculate that there should be some structural differences in both dark phases. Evidently, though the proposed models for these phases do not rely on chirality [95], its existence can alter to some extent the resulting structures. To what extent these modifications are important remains an open problem.

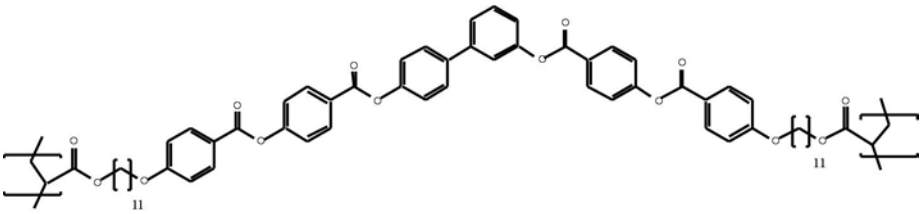

Fig. 66: Chemical structure of the studied polymer. The phase structure is SmCP at room temperature.

Finally another experimental evidence in support of the steric reasons for the formation of the dark phase is presented. The stability of the dark state during a process of in-situ photopolymerization is studied in the experiment. With this purpose a photopolymer based on the monomer studied in this work was prepared. Fig. 66 shows the chemical structure of the polymer. The synthesis and the experimental details of the photopolymerization process have been published elsewhere [107]. The bisacrylate monomer to be photopolymerized was introduced in a commercial Linkam cell of 5 μm thickness. The sample was cooled down from the isotropic phase under a square-wave electric field of 10 $V\mu m^{-1}$ and 10 Hz in order to obtain the homochiral dark state in the mesophase. The existence of the dark state in the monomer was checked in the polarization microscope after field removal exactly in the same way as the compound in Fig. 58. Afterwards, the in-situ photopolymerization was carried out under no electric field following the procedure explained in ref. [108]. In Fig. 67 the texture exhibited by the high-weight molecular material is depicted. As can be seen, the texture appears drastically modified after the photopolymerization process and it presents a fan-shaped structure characteristic of a SmCP mesophase. The phase was checked not to be ferroelectric since the material was SHG inactive. Moreover the extinction brushes are parallel to the directions of the polarizers, indicating a possible SmC_AP_A phase. The phase transformation that the material undergoes in the process, could give some information about the mechanism that drives the formation of the dark state in the low-weight molecular material. In fact, the lost of the dark ground

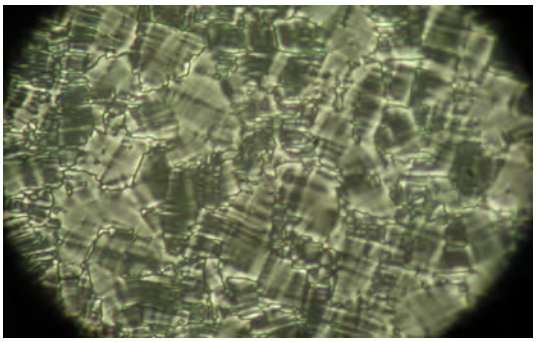

Fig. 67: Texture of the photopolymer at room temperature (photo 200 μm wide).

state during the photopolymerization process could point towards a steric origin of the layer distortion that would be deeply modified during the cross-linking process. This fact supposes an additional experimental support to the idea that the stabilization of the dark state is a consequence of the steric interactions at least in this compound. More studies should be carried out in different compounds in order to clarify if this mechanism is the unique one that can give rise to the dark state or, on the contrary, the interactions that originate this phase depends on the features of each compound.

To summarize, a bent-core compound where two types of optically isotropic phases (homochiral and racemic) can be induced by an electric field has been studied. SHG and electrooptic measurements indicate that the local ordering of dipoles in adjacent smectic layers is antiferroelectric in the ground state of both structures. It has also been found that cross-linking can destabilize the dark structures and transform them into normal smectics. As a conclusion, it is deduced that the main reasons for the folding of the smectic layers are steric effects. Chirality effects are ruled out, and the field induced polar order can perhaps reinforce the layer distortion since it promotes the separation of incompatible molecular fragments in different sublayers. However, the saddle-splay distortion must be of steric origin. Probably it is due to the mismatch of areas required by the different molecular fragments if they are to be accommodated in flat layers [109] [76].

Chapter 6

Functionalities of bent-core liquid crystal materials

Smart (or functional) materials are materials that have one or more properties that can be significantly changed in a controlled fashion by external stimuli, such as stress, temperature, moisture, pH, electric or magnetic fields. In other words, this type of materials take advantage of their properties to achieve a functional action.

Liquid crystals fall into this category and their functionalities have been already been used extensively: LCDs, sensors, etc. Despite of this, the prospects for these materials are even bigger, and improved and new functions are being suggested continuously.

Bent-core liquid crystals add new degrees of freedom to the existing materials and since the beginning have been thought as interesting for future applications. Expectations focus primarily in the field of ultrafast electrooptical modulators due to their improved nonlinear response above that of classical liquid crystals (see Chapter 3). A few distinct applications have been suggested in the literature (see, for example, [110][111][112]). For a review of bent-core liquid crystals as fucntional materials see [5].

In this chapter I want to add two new ideas for the use of these materials, which were found and explored while researching new molecular structures.

Liquid Crystal Display modes.

Liquid crystal displays (LCDs) are probably the most widespread, developed and profitable application of liquid crystals. A lot of work has been carried out to go from the first displays in the 60s to the huge colorful HD-LCD TVs available nowadays anywhere, but the basic operation remains relying mainly on the simple twisted nematic effect [113], in-plane switching (IPS) [114] or vertically aligned (VA) [115] modes. However, engineers are still looking for LCD modes with improved performance.

The requirements for an ideal LCD mode are the following:

- fast response
- high contrast ratio
- wide viewing angle
- continuous gray levels

Conventional modes using nematic liquid crystals lack an optimal fast response to an electric field and an approach using ferro- [116] and antiferroelectric [117] liquid crystal (FLC and AFLC) modes has been developed. These FLC modes need to present the so called V-shaped switching (continuous change of transmitted light intensity) to achieve a continuous gray scale.

Polarity in phases of bent-core molecules is almost always present, but because of the well established monopoly of nematics in the LCD industry and the early stage of research in which bent-core still are, these materials are not used for this end. Up to now, only a few applications have been proposed for this type of materials and, among them, two are LCD modes:

- In [111] A. Jákli *et al.* presented a scattering-type display using smectic phases of bent-core molecules. Depending on the clinicity of the phase the light passing through the material is more or less scattered. Scattering in materials occurs in the defects, where the optical tensor changes. In this case, this is related to the size of optical domains, which is usually larger in an anticlinic configuration than in the synclinic ones. The proposed display uses an electric field to switch the clinicity of the phase, and consequently the transparency of the "screen". The transmission in the scattering state is still high and this leads to a poor contrast ratio (circa 2:1). But the mode has its advantages, such as: fast switching times and that it does not need polarizers or aligned samples.
- In [112] Y. Shimbo *et al.* used a uniaxial smectic phase that was easily aligned in a homeotropic configuration. Consequently the sample was black between crossed polarizers. Initially presented as a $SmAP_R$ phase [118], later it was concluded that it consisted of small non-tilted ferroelectric domains pointing in random directions in the layer [119]. If an electric field was applied, these domains oriented themselves and a birefringent state (bright state) was achieved. The proposed LCD mode fulfills all the requirements for an ideal mode performance.

A last LCD mode has been proposed by our group [120]. It makes use of the dark phases studied in Chapter 5. In view of the behavior of the dark phase under field, it seemed straightforward to suggest it as a good LCD mode.

Dark phase liquid crystal display

(text adapted from[120]).

The material used is studied in depth in Chapter 5 (see Fig. 58 in page 68). It presents two dark phases, depending on the field treatment: homochiral and racemic. It was concluded that the formation of the dark phases was due to steric reasons that made (strongly) bent layers energetically favorable.

The working principles of the display are simple and appear sketched in Fig. 68. Without field the cells are dark between crossed polarizers (Fig. 68a and b). Under an electric field the smectic layers become partially unfolded and the material presents light transmission (Fig. 68c and d), since now the sample is a disordered cell of a SmCP-type phase. Both in the homochiral and racemic variants the field-on state consists of very small domains oriented at random. The switching is reversible and, due to the averaging process of the domains, the amount of light transmitted through an integrated area larger than 100x100 μm^2 is independent of the field polarity (Fig. 70).

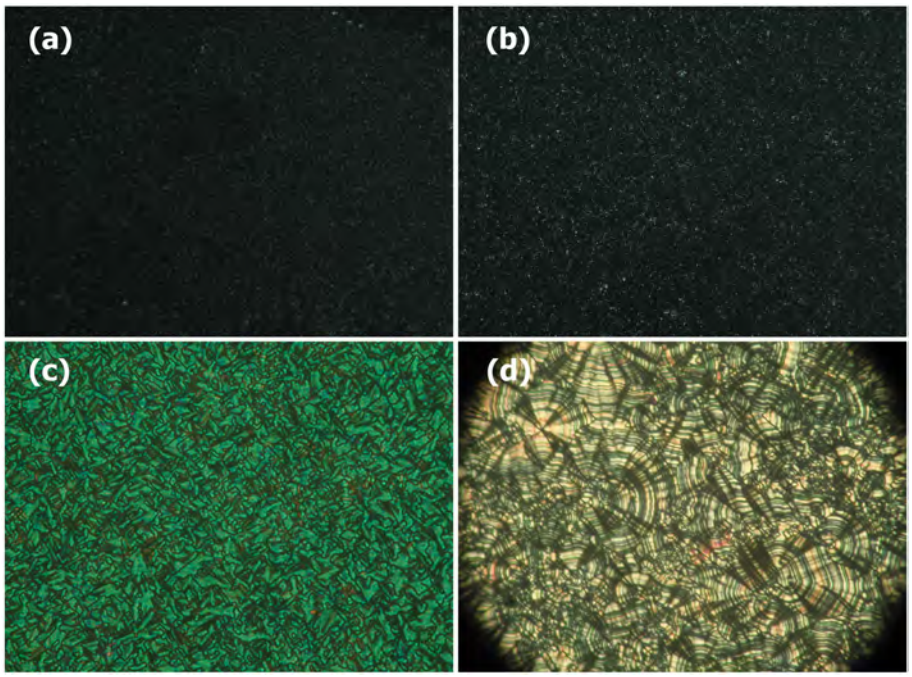

Fig. 68: (a) Texture of the homochiral isotropic state under crossed polarizers. On uncrossing the polarizers slightly, the chiral domains would be observed. (b) Texture of the racemic isotropic state. (c), (d) Textures of the material under crossed polarizers in the field-on state for the homochiral and racemic samples, respectively.

Some characteristics of the display are shown in Fig. 69. Under the action of a bipolar step wave the resulting rise and fall times of the electrooptic response are plotted as a function of the amplitude of the electric field. For these measurements Linkam™ 5 μm thick cells were used. Almost no field dependence is found for the fall times whereas the response upon field application varies between 0.35 ms and 0.08 ms. These characteristic times increase somewhat on decreasing temperature, but fast response below 0.5 ms is achieved in all the temperature range.

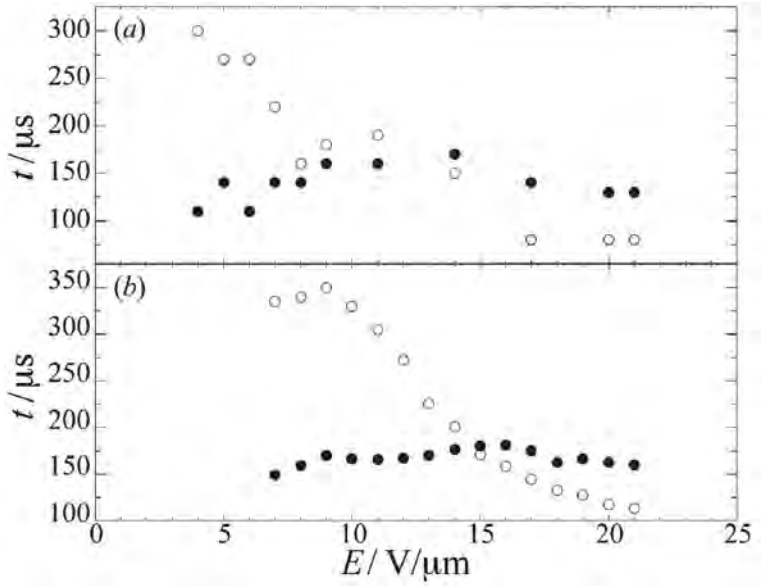

Fig. 69: Optical transmission fall times (full circles) and rise times (open circles) obtained under a bipolar step wave, as the one shown in Fig. 70, at 146 ºC for both (a) homochiral and (b) racemic phases.

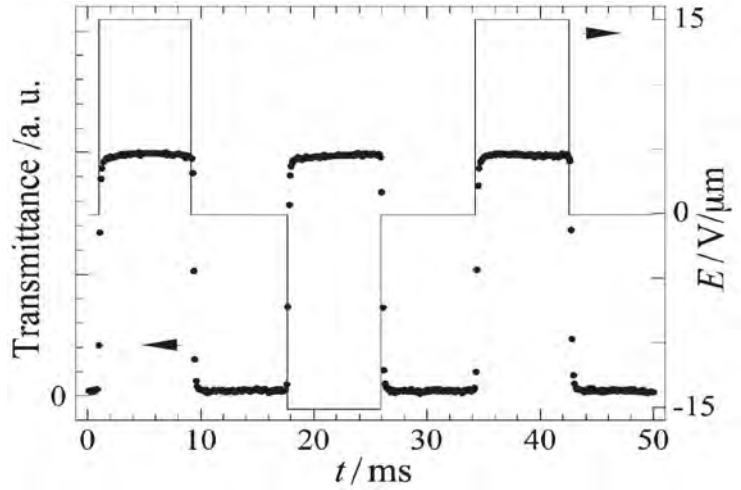

Fig. 70: Transmittance of the sample between crossed polarizers at 146 ºC in the racemic phase (points) together with the applied electric field (lines).

Fig. 71 shows the transmission as a function of the electric field. An almost perfect V-shaped switching is achieved without any threshold field for the electrooptic response. This permits the realization of continuous grey levels. The contrast ratio is rather high (about 300:1) for the homochiral variant and somewhat smaller (about 100:1) for the racemic one. This is due to presence of more defects in the ground state of the latter.

Finally a few words about the viewing angle of the device. Though no detailed analysis about this point has been carried out, a rather wide viewing angle is expected for the display. This idea is based on the perfect isotropy of the field-off states (rigorously independent of the illumination direction) and on the compensation effects on the angle dependence of the light transmission that the random orientation and small size of the domains (Fig. 68c and d) produce in the field-on states. In particular, due to these specific characteristics of our device the contrast ratio does not depend on the azimuth of the viewing direction.

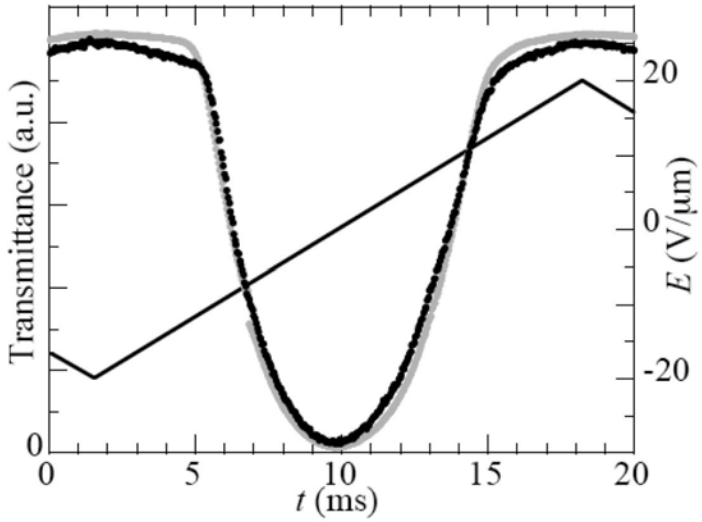

Fig. 71: Optical transmission measurements as a function of time performed under a 30 Hz triangular wave field at 146 ºC for both homochiral (gray symbols) and racemic (black symbols) phases. No threshold field is observed in the switching for any of the phases. The graphs are adapted to the optimal cell thickness for maximum transmission under field.

Summarizing, an LCD mode based on the optically isotropic phases shown by some bent-core molecules has been described. The LCD is fast, has quite large contrast ratio, permits to obtain continuous grey levels, and has wide viewing angles. As an additional advantage, there is no necessity for alignment, which is very important in practice and adds robustness to the device. The reported LCD mode compares very favorably to other existing display types such as vertical alignment, in-plane switching and ferroelectric LCD modes. More synthetic work is necessary to obtain materials possessing the adequate phases and characteristics in appropriate temperature ranges.

A liquid crystal material for molecular electronics.

The emerging field of molecular electronics is avid for new materials with certain characteristics that could help it to develop real applications. As its name indicates, molecular electronics aims at building electronic components composed of molecules, thus merging the fields of physics, chemistry and material science. It is clear that liquid crystals and related materials are serious candidates to fill that hole. Mesophases offer soft phases with lamellar, columnar or cubic arrangements and, consequently, the formation of ordered functional systems. Specially, the relative easy synthesis of specifically designed materials could be of great advantage, and this promotes research on structure-property relations. Also polarity and chirality appear as two new degrees of freedom to be utilized in devices.

Charge transfer processes are the key processes in the physics of materials for molecular electronics, but also other properties can be useful for certain applications. Materials which respond to fields such as temperature, pressure, light, etc. are remarkable because they can be used as, for example, sensors. Therefore, the incorporation of electro- and photoactive units into soft materials is of great interest.

Materials containing tetrathiafulvalene (TTF) units (see Fig. 75) and its derivatives are very well-known due to their intermolecular charge transfer properties and may be considered among the most prominent components of molecular electronics, giving rise to many good organic conductors and superconductors. They behave as excellent electron donors, working on the basis of the π–π overlap of the constituent molecules, which usually crystallize forming chains or stacks due to the strong interaction between sulfur atoms [121][122]. Semiconductors obtained from TTF derivatives are p-type and have allowed, for example, the implementation of organic field–effect transistors (OFET) [123][124] where the TTF derivative connects the source and drain electrodes, and a n-type Si semiconductor substrate constitutes the gate terminal. Furthermore, due to the strong photoresponsivity of the employed TTF derivative, some of these OFETs operate also as phototransistors, showing a clear increase of the drain current, for constant drain and gate voltages, when the device is illuminated with white light [124].

A further step in the investigation of new organic materials with good charge transport properties is the synthesis of liquid crystalline derivatives of TTF. However, although this strategy seems to be rather obvious, only a few mesogenic compounds derived of TTF have been reported up to now. These are calamitic and discotic liquid crystals with the TTF moiety at the center of their molecular cores [125][126][127][128]. The former ones present nematic and SmA mesophases in different temperature ranges, while rectangular columnar phases have been proposed for the discotic compounds. Some of these materials show ohmic response under dc voltages, and very low ac conductivity, mainly dominated by ionic impurities [127]. Others, however, exhibit fast electronic

conduction with mobilities as high as 1 $cm^2V^{-1}s^{-1}$. Successful OFET operation has been reported in a few cases [129].

Photoresponsivity and deracemization in a bent-core liquid crystalline derivative of tetrathiafulvalene

(text adapted from [130])

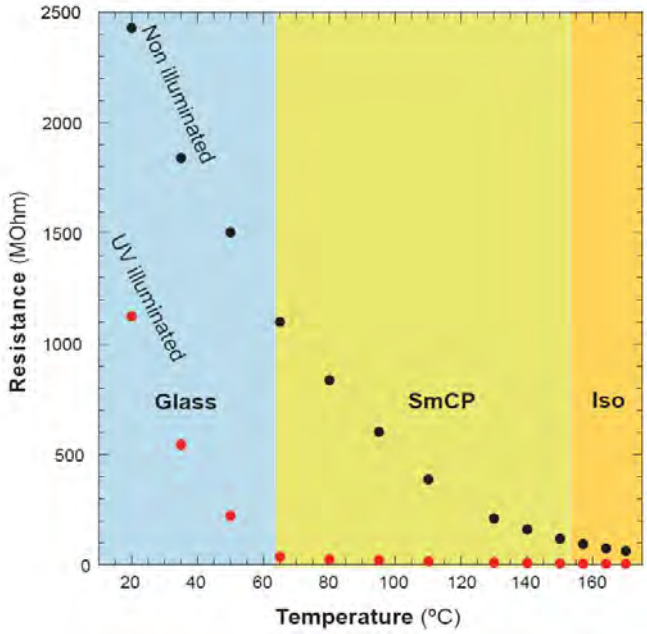

Fig. 72: Electrical resistance of the sample versus temperature, where the expected behavior before illumination (black dots) can be observed. The photoconductivity effect appears as a drastic decrease in the resistance when the sample is illuminated with UV light (red dots). In the mesophase the effect is especially noticeable.

Bent-core materials with TTF units were synthesized by our colleagues in Zaragoza [131] and their mesomorphism confirmed. The idea behind this effort was that the good packing of the bent-core molecules within the layers could enhance the charge-transfer properties of the TTF groups. Their structural characterization is described in Chapter 7 [31] , and here we will focus on the study of compound I in Fig. 76 (pg. 90). This material present a dark SmCP phase when cooling down from the isotropic liquid and, on further cooling, a glassy state. Applying an electric field the mesophase becomes irreversively birefringent and very interesting effects are observed when it is illuminated with UV light.

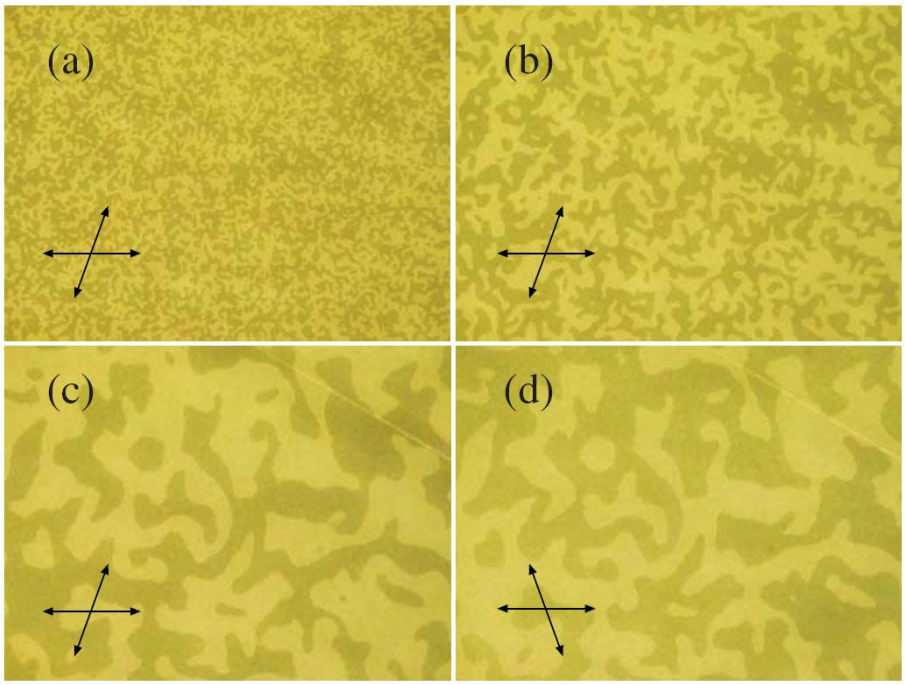

Fig. 73: Growth of chiral domains under electric field. The texture is obtained under electric field after light irradiation in the mesophase near the clearing point. The photographs (a)-(c) were taken subsequently in time intervals of 40 s. Arrows indicate polarizers orientation. (d) The same as (c) but with the polarizers uncrossed in the opposite sense.

We carried out photoconductivity studies in this material by measuring the sample electrical resistance in a Linkam cell (thickness = 5 μm, area = 81 mm^2). For the experiment a 10 MΩ resistor was set in parallel to the sample and the equivalent resistance was measured by using a HP 34401A multimeter. Prior to the irradiation with UV light the resistance was measured from room temperature up to appearance of the isotropic liquid. The sample resistance values in the different phases appear in Fig. 72 . As expected, conductivity increases with temperature, and in the glassy state the material presents very large resistance. After this preliminary characterization the sample was illuminated with an ELC-403 halogen lamp (Electro-lite Co.) and the irradiation on the sample in the wavelength range of 340–380 nm was ~50 $mWcm^{-2}$. As can be seen, the resistance decreases noticeably in the light-on state (red dots in Fig. 72). This effect is especially remarkable in the SmCP phase, where the difference is larger than one order of magnitude. Photoconductivity is also observed in the low-temperature glassy state but the effect is less important (the conductivity is about twice larger for the illuminated sample). In all phases the effect is reversible and its response time is much shorter than 1 s. During the illumination process the sample texture remains unaltered. The conductivity values are similar in the virgin dark state as in the field-induced SmC_AP_A phase. The general features of the photoconductivity and, in

particular, the ratios between dark and photocurrents in the three phases are similar to those found in liquid-crystal materials especially designed to present photoconductive properties [132].

However, an unusual behavior is observed if the sample is illuminated in the SmCP phase at a temperature close to appearance of the isotropic liquid (approximately less than 5 °C below the clearing point). Under these conditions, if the sample is irradiated in the field-induced birefringent state the texture becomes dark gradually, being perfectly isotropic after about 1 min. of illumination. After light removal, the texture remains dark and no chiral domains can be observed when the polarizers are uncrossed. In contrast to the non-illuminated sample, a subsequent electric field application does not result in a change to a birefringent texture. However, under electric field, the dark texture develops chiral domains of opposite handedness whose size increases noticeably in a short period of time (see Fig. 73). This field-induced texture demonstrates the mesomorphic character of the dark texture after the light is turned off. If the sample is heated up to the clearing point and subsequently cooled down into the mesophase, the birefringent texture is no longer obtained after electric field application. A grainy yellow texture embedded in the dark one is observed instead. This yellow birefringent texture relaxes into the chiral dark state after field removal. This effect is observed whenever the sample has been illuminated near the clearing point, either in the original dark state or in the field-induced birefringent state.

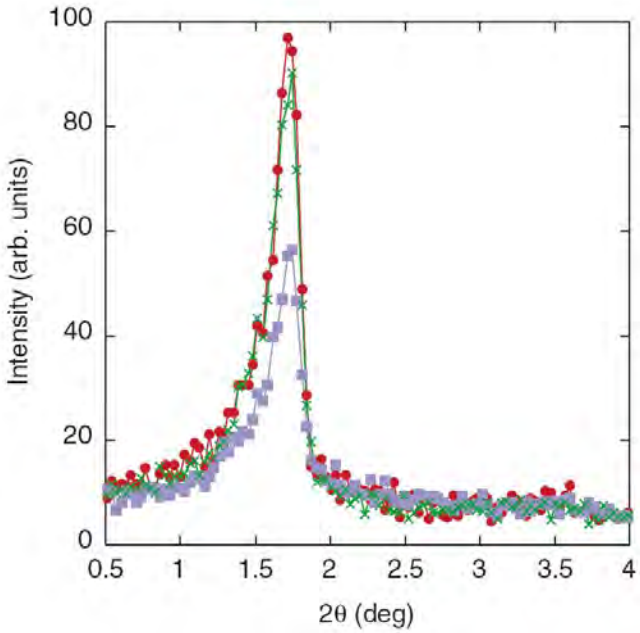

Fig. 74: Small angle X-ray diffraction pattern at 152 ºC. Red, blue and green points correspond respectively to data before, during and after the illumination of the sample with UV light. The second-order smectic peak is hardly visible because of the short exposure time to the x-ray beam (about 1 minute).

In order to clarify the light-induced transformation near the clearing point, small-angle X-ray diffraction studies were carried out in a powder sample at 152 °C (Lindemann capillaries of diameter 0.5 mm). The diffraction pattern shows two sharp peaks at small angles that correspond to the first and second orders of the smectic periodicity. In the experiment the irradiation conditions are similar to those described above. After 1 min of illumination the first-order peak clearly decreases and remains steady during the rest of the irradiation period (see Fig. 74). After the light is switched off, the peak recovers its initial value. This result indicates that, on illumination, part of the sample undergoes a phase transition to the isotropic liquid. The inner portion of the sample remains in the mesomorphic state probably due to the strong light absorption of the material.

The light-induced phase transition to the isotropic liquid cannot be explained in terms of a mere heating of the sample, since the field-induced birefringent phase, which appears in the virgin sample, is no longer obtained after UV light exposure. Therefore, an irreversible molecular alteration must have happened. Therefore, an irreversible molecular alteration must have happened. This process was studied in [133] by means of nuclear magnetic resonance and diffusion-ordered spectroscopy. Therein the formation of a dimer is suggested. A consequence is the reduction of the domain size to a mesoscopic scale due to the disorder induced by the altered molecules. This idea is supported by the small size of the grainy yellow texture embedded in the dark texture that the material shows under electric field. Assuming this hypothesis, only a small portion of the domains would present macroscopic size so as to exhibit birefringence (yellow grainy domains in Fig. 73).

It is important to point out that the electric field induces a fast chiral segregation in the dark texture that has been exposed to UV light near the clearing point (see Fig. 73). Presumably this segregation takes place even in the virgin mesophase after field application; in fact the texture is homochiral. However, as the material is birefringent, no rotatory power is observed. Field-induced chiral segregation has also been reported in calamitic racemic mixtures [134][135] but with much longer time scale (months) [135]. In this thesis, a similar chiral segregation is described in Chapter 5 when a material is cooled from the isotropic phase under field.

This coarsening dynamics of chiral domains was theoretically studied as a curvature-driven process in [136] making use of an exact result for the distribution of Hull-enclosed areas in two-dimensional coarsening with non-conserved scalar order parameter dynamics [137]. It is proved that deracemization in this bent-core liquid crystal belongs to the Allen-Cahn universality class. and that the exact formula, which gives us the statistics of domain sizes during coarsening, can also be used as a strict test for this dynamic universality class.

It is interesting to remark that the disappearance of the birefringent texture and its

substitution by the optically isotropic mesophase after illumination is an irreversible process. Even the procedure of heating the material up to the isotropic liquid point and cooling down again under field is insufficient to reproduce the birefringent phase. The starting point for the change of texture is likely to be the generation of charge carriers. In addition, at temperatures close enough to appearance of the isotropic liquid, a molecular modification takes place under light, which is evidenced by a transition to the isotropic liquid. Probably this modification involves a change of the molecular shape from the bent profile (adequate for promoting the mesophase) to something different. The investigation of the origin of these light-driven molecular changes will be a subject for future work. A similar isothermal transition to the isotropic liquid has also been observed upon illumination with blue light in some mesogens (including bent-core materials) whose molecules have azo or azoxy groups [30][138][139][140][141]. In those cases the molecular shape is changed by the passage from trans to cis conformations, and the effect is reversible. In the present case however the material "remembers" the transition to the isotropic liquid and is irreversibly transformed.

As has been mentioned above, the effect is different at lower temperatures far from the isotropic liquid. In these temperatures the light is unable to induce any transition to the isotropic phase and, as a consequence, the behavior of the material under field is normal (i.e., birefringent domains appear under field instead of a dark conglomerate phase). This indicates that the decrease of the electrical resistance upon illumination is due to the photo-generation of charge carriers that do not alter the chemical nature of the molecules.

The investigation of the character of the photo-current (ionic or electronic) has not been treated in this work. To analyze this point it would be very interesting to carry out time-of-flight measurements on very pure samples [142][143]. We consider that the conduction can be electronic in the mesophase due to the relatively high π–π overlap in the TTF groups of the constituent molecules, because of their efficient packing in this kind of structure. This idea is supported by the fact that the resistance ratio between light-off and -on states in the isotropic phase would be expected to be equal to or larger than that in the mesophase if the conduction was exclusively ionic [132]. On the contrary, in our case this ratio is 30% higher in the mesophase. The analysis of the nature of the conductivity is our project for future work.

In summary, a bent-core mesogen containing a TTF group has been studied. The material spontaneously presents an achiral optically isotropic mesophase (sponge-like SmCP phase), which can be converted into a normal SmC_AP_A phase after treatment with an electric field. In addition we have found some unusual photoinduced effects. Just below the clearing point, illumination with UV light induces a transition to the isotropic liquid, which creates a permanent memory in the material and suppresses the formation of macroscopic SmC_AP_A domains. A dark conglomerate phase appears instead, where the electric field segregates chiral domains of opposite chirality.

Furthermore, in the whole temperature range we have detected the existence of photoconductivity. The effect is especially remarkable in the mesophase and isotropic phase. The possibility of electronic conduction in the mesophase has been briefly discussed.

Chapter 7

Characterization of new bent-core liquid crystals with tetrathiafulvalene units

(text adapted from [31]).

Molecular design is a challenging issue in the liquid crystal field. The mesomorphic properties of liquid crystal materials present a high dependence on chemical structure modifications giving rise to new interesting properties. In this respect, great efforts are being made on synthesizing new materials with specific mesophases and features by using different molecular geometries and proper functional groups.

On the other hand, classical liquid crystal phases for calamitic or discotic materials are (more or less) well established, but the relatively new B phases are in an early stage of research and a lot of work is still to be done . From the structural point of view, the determination of the molecular organization is a challenge itself because there is no straightforward method.

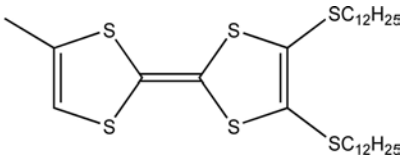

Fig. 75: Chemical structure of a TTF unit.

Three bent-core mesogenic materials containing tetrathiafulvalene (TTF) units (see Fig. 75) synthesized by the group of chemists at the University of Zaragoza [131] are characterized below. Based on electro-optical, X-ray scattering and SHG measurements, we elucidate the structure and some properties of the mesophases.

TTF and its derivatives are very well known due to their intermolecular charge transfer properties and are usually employed in molecular electronics as organic conductors

and semiconductors [54][55][57][144][145]. Their interest also lies in the fact that inside a molecule they behave as good electron donors [54]. Hence, this property can be useful for the development of materials with good nonlinear optical properties such as second harmonic generation. Other functionalities of this functional group are explained in Chapter 6, where a detailed analysis of one of compound I in Fig. 76 characterized below is made.

The chemical structures and phase sequences of the studied materials on cooling are shown in Fig. 76. The phase assignment will be discussed separately for each mesogen below. As can be seen, compound III has one TTF unit next to the terminal chain in both lateral structures of the molecule whereas compounds I and II possess only one TTF unit.

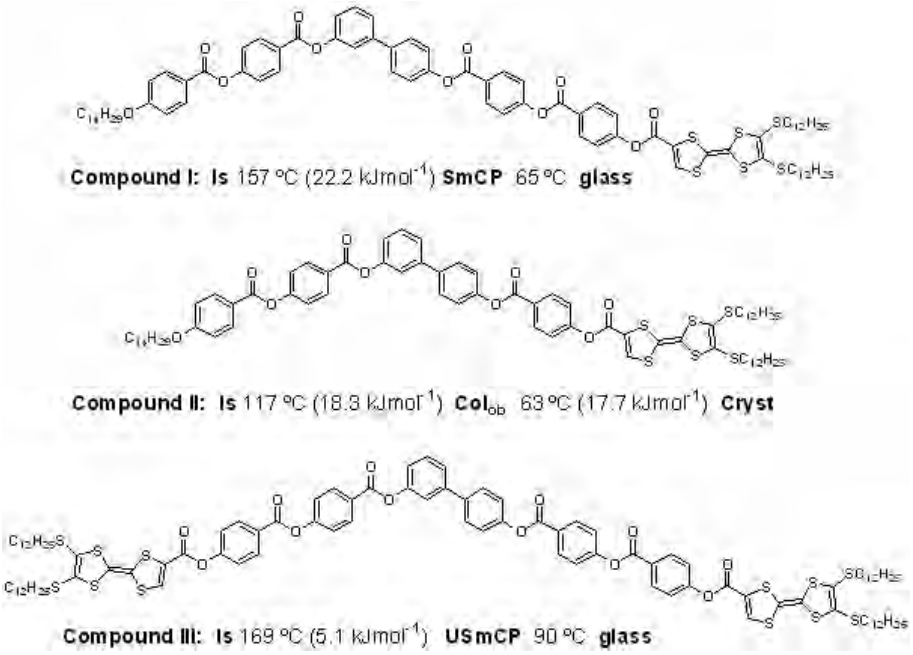

Fig. 76: Chemical structure of the compounds I, II and III, together with their phase sequence and enthalpies on cooling. The transition temperatures were obtained from differential scanning calorimetry.

Compound I

This material shows a completely dark texture, indistinguishable from the isotropic liquid, down to room temperature on cooling from the isotropic phase. The X-ray diffraction pattern shows two peaks, which correspond to the first and second orders of a given periodicity. A diffuse peak is also observed at wide angles, which confirms the mesomorphic character of the phase above 65°C. Therefore, it can be concluded that the mesophase is lamellar. The layer spacing is 51 Å, which means that the molecules are tilted about 43° (assuming a molecular length of 70 Å in the most extended configuration and using MM2 Force Field modeling). Below this temperature

the material is no longer fluid but the diffuse peak still remains. This fact indicates a glassy nature of this phase. The glassy state has been observed to relax into a crystalline phase after several days.

After applying an electric field in the mesophase above a threshold of 12 $V\mu m^{-1}$, the texture becomes gradually birefringent. Under a square-wave electric field, the texture is initially grainy and bright yellow. After several seconds it gradually turns into darker green domains. In Fig. 77a both kinds of textures appear coexisting. After removing the electric field the isotropic black texture is no longer recovered. Yellow domains relax into a greenish gray texture whereas dark green ones become pale green (Fig. 77b). This behavior can be interpreted as a field induced flattening of the bent layers in the dark phase. In this particular case, the change is irreversible, probably due to surface effects, although the dark phase is recovered after heating the sample to the isotropic phase and cooling it down again. This behavior has been also reported in other bent-core materials [105][146].

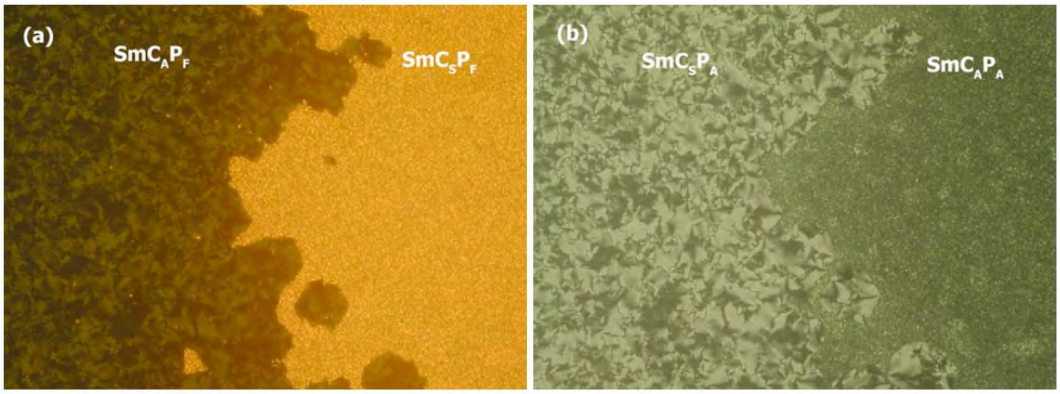

Fig. 77: Optical textures of compound I after electric field application at 110 °C, (a) with the field on (20 $V\mu m^{-1}$)and (b) once the field is removed. In both pictures racemic and homochiral states are coexisting. Pics are 600 μm wide.

The bright texture in Fig. 77a is highly birefringent and extinctions (hardly visible in the figure due to its low magnification) change with the field polarity which implies a homochiral synclinic (SmC_SP_F) arrangement under field. On the contrary the dark green texture is compatible with a racemic anticlinic structure (SmC_AP_F). Both textures relax, after field removal, into SmC_AP_A and SmC_SP_A respectively.

It must be mentioned that under a triangular-wave electric field the homochiral structure can be recovered. In this respect, chirality changes induced by the electric field waveform have been previously reported in reference [67]. However, in that work the behavior was the opposite we have found here, since the triangular-wave electric field favored the racemic state, whereas the square-wave induced the homochiral state.

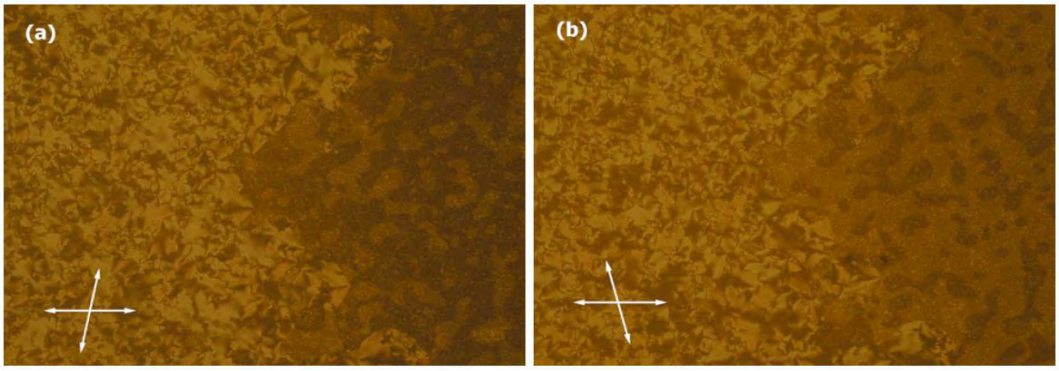

Fig. 78: Chiral domains of the homochiral phase (right side) coexisting with domains (left side) of compound I at 110 ºC. The optical activity can be observed due to the small domain size in the homochiral phase, which gives rise to an almost optically isotropic texture without electric field. In (a) and (b) polarizers are slightly uncrossed in both senses.

It must be also pointed out that the homochiral state presents very small domain size, which gives rise to a very low birefringence in the ground state. As a consequence chiral domains can be observed when uncrossing the polarizers (see Fig. 78a and b)

Optical activity can also be observed as we enter the mesophase from the isotropic state with the field on. Large chiral domains are clearly visible against a dark background before the birefringent texture grows over them as the temperature goes down (Fig. 79). Therefore it can be concluded that the field is responsible for the segregation of domains with different chirality. This process is not new in this thesis as it has also appeared in the material of Fig. 58 (pg. 68) [147].

Fig. 79: Large chiral domains are visible at 156 ºC on cooling from the isotropic phase with the electric field applied (12 $V\mu m^{-1}$) by uncrossing the polarizers (1200 μm wide).

SHG measurements confirmed the antiferroelectric character for the ground state: null signal without field and nonzero with the field on. However, the polarization

switching current under a triangular-wave voltage shows only one peak per half cycle [131] (polarization about 400 $nCcm^{-2}$). See Chapter 3 for an analysis of the SHG efficiency of this compound.

Photosensitivity due to the TTF units has been also found in this material. Upon illumination with UV-vis light, the conductivity increases greatly in the mesophase. Furthermore, light induces a phase transition near the clearing point and somehow alters the properties of the material at the irradiated zone. These issues have been discussed in detail in [130].

Compound II

Fig. 80 represents the small-angle X-ray diffraction diagram obtained at 110 °C on cooling. The indexing of the pattern was carried out on the basis of an oblique 2D lattice, the cell parameters being a=39Å, c=48Å, and β=78°. The validity of the indexing scheme was checked at different temperatures on heating and cooling. A continuous variation of the lattice parameters was detected, β reduces in 2° at 95 °C. The high intensity of the peak indexed as (01) suggests a strong lamellar character. From its corresponding periodicity, a tilt of 46° is obtained if a molecular length of 67Å deduced from molecular modeling in an all-trans conformation is assumed.

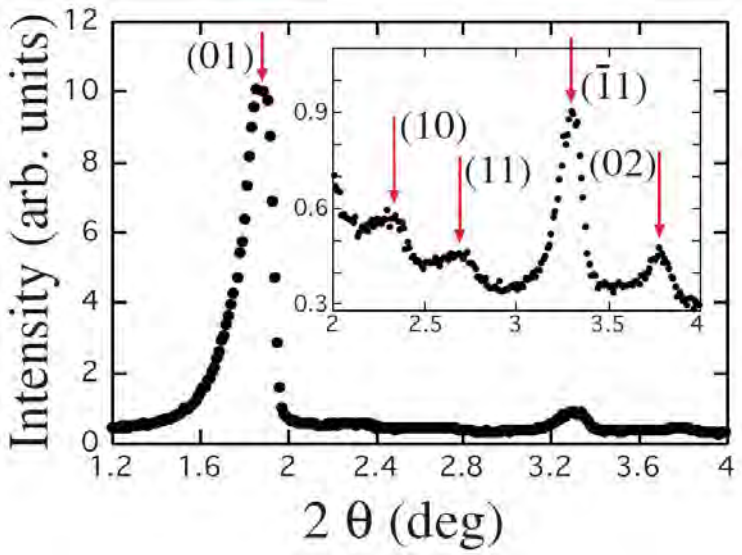

Fig. 80: X-ray diffraction pattern of compound II at 105 °C, together with the peak indexation proposed. Intensity is plotted against 2θ, where θ is the Bragg angle. The inset shows an enlarged view of the small peaks appearing to the right of the largest one. Arrows indicate the theoretical positions of the maxima.

The optical textures observed during the electro-optical studies for this material are shown in Fig. 81. On cooling from the isotropic state a texture possessing pale colors

with birefringence between 0.04 (greenish yellow) and 0.10 (brownish orange) is obtained (Fig. 81a). If a large electric field is applied (30 $V\mu m^{-1}$, 10 Hz, square-wave) the texture becomes green (Fig. 81b) with Δn=0.14. It is to be stressed that no optical switching is observable, and the green texture remains after the field is removed. Furthermore, SHG is detected only when the field is on, indicating that the material is ferroelectric under field and antiferroelectric without field. Consequently, the lack of optical switching means that the polarization inversion occurs through molecular rotations about their long axes (chiral switching). The high birefringence of the texture in Fig. 81b indicates that the arrangement is synclinic (both in the ground and in ferroelectric states). Therefore, Fig. 81a corresponds to a disordered bulk where the molecular dipoles are mainly parallel to the glass plates. Then, the field effect is just to rearrange the structure by orienting the dipoles in the direction perpendicular to the glasses with the consequent increase of Δn (Fig. 81b). A similar electrooptic effect has been previously reported in columnar phases of other bent-core materials [148][149]. In the present case, after the molecular reorientation, no electrooptic effect is further detected, even if the field is removed.

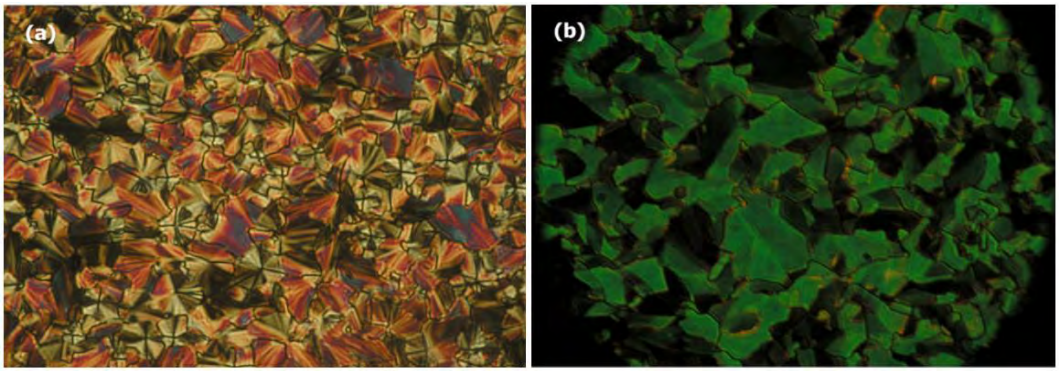

Fig. 81: Optical textures of compound II at 105 ºC: (a) (240 μm wide) on cooling from the isotropic phase and (b) (200 μm wide) after applying the electric field (20 $V\mu m^{-1}$).Once the field is applied, the texture is the same as (b) with or without field.

We propose now a structural model for the mesophase of our material. First we analyze and choose the appropriate 2D electron density distributions among those in agreement with the observed X-ray diagram. The method is depicted in Chapter 2 (page 19) and makes use of the peak intensities. In the case of this compound, the density maps obtained for any of the sign combinations are very similar to that shown in Fig. 82. The lamellar character and a modulation of the electronic density are clearly present. The combination of signs was chosen in order to maximize the length of the white areas in the map, where the electronic density is higher, with the aim of allowing suitable molecular packing and reducing empty regions as much as possible. Fig. 83a represents a possible structural model for the mesophase. Molecular directors have been set in such a way that are compatible with the observed optical tilt and almost

perpendicularly to the longest direction of the brighter areas in the map of Fig. 82. This arrangement permits to obtain the best packing. The phase resembles a SmC_SP_A phase undulated according to a sawtooth wave. The structure is racemic since it is synclinic antiferroelectric, therefore blue and red molecules must be present in equal proportion. It is important to point out that, as the phase is not strictly smectic, the tilt angle must be understood as the angle of the molecular director with respect to the (001) direction, i.e., perpendicular to the *a* vector in Fig. 82. Another alternative possibility to Fig. 83a is a racemic synclinic organization but with the polarity reversing now along the *a* direction. This has the advantage that the aromatic rod-like wings become aligned parallel at the edge of the blocks and this is expected to have lower energy (see, e.g., Fig. 18 in Ref. [150]). With conventional non-resonant X-ray diffraction these alternatives cannot be distinguished.

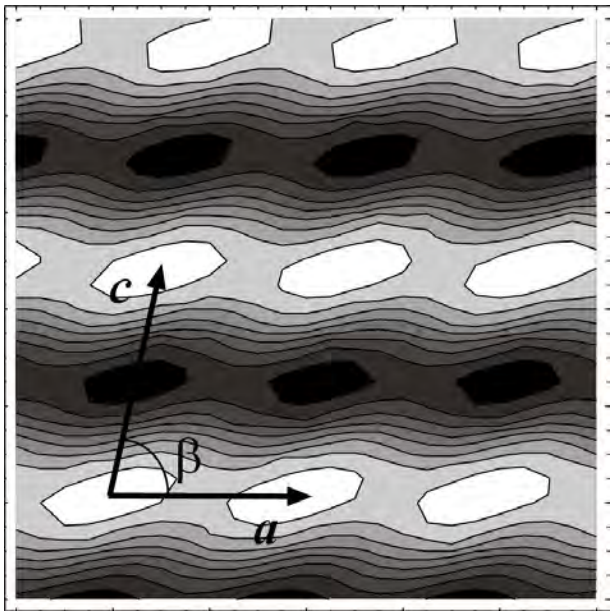

Fig. 82: 2D electron density map calculated from the data of Fig. 80 for compound II. The brighter regions represent the areas of higher electron density. In this particular case the signs chosen in eq. (2) in pg. 16 for the structure factors are (− − − − +). The order of signs corresponds to the appearance of the peaks in Fig. 80. The unit cell parameters are also sketched on it.

Finally, Fig. 83b and c illustrate the chiral switching mechanism under inversion of the electric field polarity: red molecules become blue or vice versa. The three structures in Fig. 83 are optically indistinguishable, and correspond to the texture in Fig. 81.

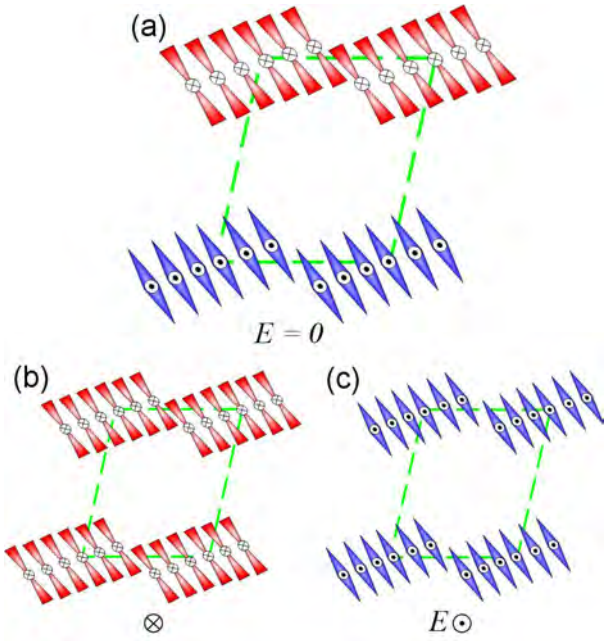

Fig. 83: (a) Arrangement of the molecules proposed for compound II together with the corresponding structures (b) and (c) under field. The molecular packing is in agreement with the electron density inFig. 82. The antiferroelectric ordering of the dipoles is based on the SHG measurements, but their exact distribution is unknown.

Compound III

On cooling this compound from the isotropic phase the texture shown in Fig. 84 is obtained. Circular domains with the extinction crosses parallel to the polarizers are observed, pointing towards an anticlinic order of the molecules in the mesophase. This texture is maintained down to room temperature. Upon application of a large electric field (20 $V\mu m^{-1}$) the birefringence increases somewhat but no appreciable switching is observed. The sample degrades if larger fields are applied.

Small angle X-ray diffraction experiments were also performed in this compound. Fig. 85 shows the diffraction profile at 138°C. Four peaks are unambiguously detected, and a small hump also appears by the side of the largest one. All of them were indexed using a simple two-dimensional rectangular lattice with cell parameters a=141 Å and c=52 Å. No substantial changes were observed at other temperatures within the mesophase, indicating that the rectangular geometry of the lattice is not by chance. Therefore the symmetry of the structure is orthorhombic, which implies an anticlinic molecular arrangement (a synclinic arrangement is always monoclinic). Modeling the molecule in an all-trans conformation, a molecular length of 82 Å is obtained and the

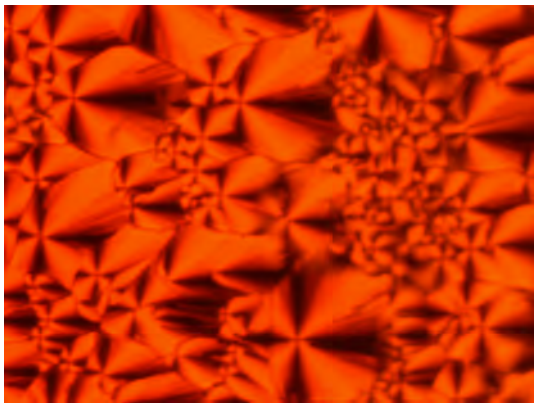

Fig. 84: Optical texture of compound III at 163 ºC on cooling from the isotropic phase with the sample between two glass slides. The red colour is due to the absorption of the compound. Pic is 240 μm wide.

resulting tilt is 51°. This tilt angle and the anticlinic order should give a low value for the birefringence, so the reddish color in Fig. 84 is mainly attributed to the large absorption of the material in the blue region. The fact that the peak indexed as (01) is the largest strongly suggests a lamellar character.

SHG measurements were also performed, but no signal was detected even with a large field applied (20 $V\mu m^{-1}$). Therefore, fields below the threshold for the dielectric rupture (about 25 $V\mu m^{-1}$) are not enough to induce the ferroelectric order.

We propose now a structural model for this mesophase using the same procedure as for compound II. The rectangular symmetry of the electron density map and the existence of the (01) reflection restrict the possible plane groups of the density map to pm2m and pm2g [151]. These symmetries imply the two following possible relations among the structure factors: $F(hl)=F(\bar{h}l)$ or $F(hl)=(-1)^h F(\bar{h}l)$, respectively [30]. Many of the sign combinations in Eq. (2) (pg. 17) produce the same density maps with shifts in the origin of the coordinate system. This fact leaves only a few different possibilities. Examining the electron density graphical representations obtained for the different sign choices, we can discard those possessing a non-lamellar character or layer structures with narrow electron density rich areas. Taking those facts into account one ends up with the possibility shown in Fig. 86. A clear modulation of the layer density is noticeable. One peculiar feature of the density map is the existence of two maxima per molecular core. This can be understood as being originated by the two TTF groups at the end of the core, which are by far the molecular parts with the highest electron density. This characteristic is very unusual and is due to the especial molecular chemical structure. In addition, the positions of the two maxima determine the molecular orientation, which is compatible with the anticlinic arrangement and with the magnitude of the tilt angle calculated above. A plausible arrangement of the

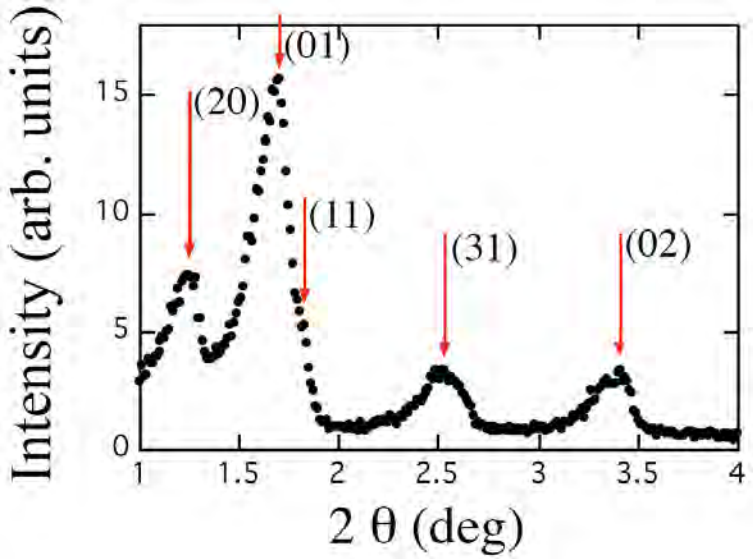

Fig. 85: X-ray diffraction pattern of compound III at 138ºC, together with the peak indexation proposed. Intensity is plotted against 2θ, where θ is the Bragg angle. Arrows indicate the theoretical positions of the maxima.

molecules in this phase is sketched in Fig. 87. The proposed structure implies the existence of defect regions to accommodate molecules with opposite tilt. The higher disorder expected in these areas diminishes the effective charge density corresponding to the TTF groups. It is difficult to determine the precise molecular arrangement at the defects but probably the connections at these regions are achieved through splay of the polarization [152].

It is interesting to compare this map with that of compound II, where the double maximum per molecular core is not visible. From a mere experimental viewpoint this fact occurs because of the small size of the (02) reflection (see Fig. 80) in comparison with the corresponding peak in compound III (last maximum of Fig. 85). In compound II there is only one electron-rich group per molecule and this implies on the one hand a smaller average electronic density; but, on the other hand and more importantly, it also gives rise to a larger disorder in the smectic layer since two TTF groups per molecule (compound III) permit a better orbital overlap in neighboring molecules and lead to a more efficient molecular packing through the connection between TTF groups. As a consequence the electron-rich region is smeared out in the map of compound II but is clearly visible in the present case.

The structure in Fig. 87 is not the unique possibility but it is certainly one of the simplest. The phase would be homochiral and antiferroelectric. Essentially, the structure is an undulated SmCP (USmCP) phase and the modulation within a layer can be understood as due to a packing fault or defect where the density is smaller than in the rest of the layer. The defects would occur at the crests and troughs of the

undulation [25]. This molecular organization corresponds to the so-called $SmCPU_A[S]$ structure as defined in Ref. [25]. Here U means undulation, A indicates opposite slopes in adjacent stripes, and [S] denotes that adjacent stripes have the same chirality. Other possible arrangements compatible with the X-ray and SHG data are the antiferrolectric racemic $SmCPU_A[S,A]$ structures (two kinds of defects between adjacent stripes, one with the same chirality and one with the opposite chirality in successive stripes).

Since the tilt alternates along the layer and not between consecutive layers (as in the traditional SmC_AP_A) it seems that the switching should be strongly hindered. This is in fact experimentally observed since the material undergoes dielectric breakdown before showing any switching.

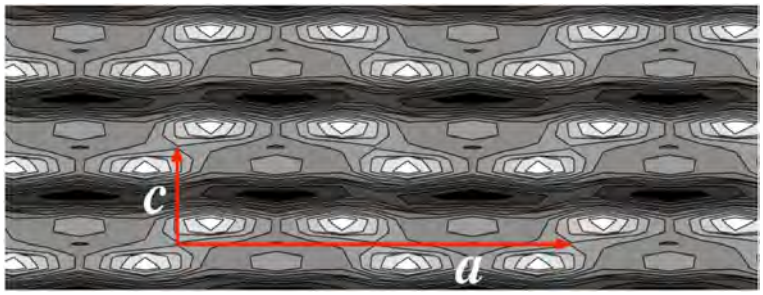

Fig. 86: 2D electron density map calculated from the data of Fig. 85 for compound III and unit cell parameters. The brighter regions represent the areas of higher electron density. The signs chosen in Eq. (2) (page 17) for the structure factors are (+ − − − −). The order of signs corresponds to the appearance of the peaks in Fig. 85.

Finally it is worth mentioning the unusually small enthalpy associated with the mesophase-isotropic liquid transition (see Fig. 76). A possibility is that due to the bulky TTF groups the cores are able to rotate almost freely around the long axes making the phase non-polar. We would have the structure of Fig. 86 but with random orientation of the dipoles within the ribbons, thus, explaining the low enthalpy and the absence of switching and SHG activity. Anyway, this small enthalpy is compatible with the existence of an important amount of cybotactic groups in the isotropic phase. These smectic clusters were evidenced by X-ray measurements, which revealed an abnormal persistence of a broadened smectic peak several degrees above the clearing point.

Summarizing, three bent-core liquid crystals with TTF units in their lateral structures have been studied. Three different mesophases have been found: a lamellar optically isotropic phase, a two-dimensional oblique phase, and a 2D rectangular phase, the last two with a high degree of "lamellarization". The first one undergoes a transition to a SmCP phase above a threshold electric field. For compounds II and III structural models have been deduced from the electronic density distributions obtained by using the intensities of the X-ray reflection peaks. According to the SHG results, the ground state of the materials is antiferroelectric (with the possibility of compound III being

non-polar).

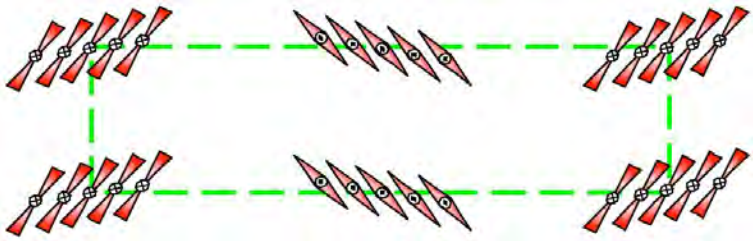

Fig. 87: Arrangement of the molecules proposed for compound III. The molecular packing is in agreement with the electron density in Fig. 86. The antiferroelectric ordering of the dipoles is based on the SHG measurements, but their exact distribution is unknown.

Conclusions

The phenomenology of liquid crystals is rich and very interesting from the basic-research point of view. Bent-core liquid crystals add the possibility of chiral phases composed of achiral molecules and a more proper geometry for the appearance of polarity. In this thesis, I have tried to shed some more light on the behavior, properties and structure of some of these materials, reaching the following conclusions:

- Improved NLO properties have been achieved by introducing better well-conjugated donor and acceptor groups in the already proper geometry of a bent-core material. NLO coefficients of the due order of magnitude for applications were measured. Different fundamental wavelengths for SHG were used and, when necessary, the absorption was taken into account in the calculations. Improving molecular hyperpolarizability to attain better NLO liquid crystal materials proved to be a good approach. There is still great potential for achieving even better materials by following this idea.

  Another molecular geometry was tested with the aim of obtaining better NLO liquid crystal materials. An H-shaped dimer-like mesogenic material with the DR-1 unit directed along the polar direction of the SmC* phase was characterized by means of SHG, and the largest reported NLO coefficients for calamitic liquid crystals were obtained. This approach was also shown to be good and further research in an analog trimer-like material is in progress.

  The presence of an absorption band at the wavelengths used in some of the experiments is not trivial and highly complicates the measurements and their theoretical interpretation. For the first time, it has been taken explicitly into account. In exchange of this added difficulty, it allowed for the study of the real effects of SHG resonances in liquid crystals.

- Several materials possessing a B1 to SmCP transition have been studied by X-ray diffraction in aligned samples. The temperature dependence of the diffraction patterns has led us to propose a mechanism for this transition. The model accounts for the low enthalpy usually observed in this process.

  In addition, the relative orientation of the dipoles among the blocks of the columnar phases has been reexamined. It is concluded that these structures

show a big degree of lamellarization with pseudo-smectic ferroelectric layers along the (11) crystallographic planes.

- SHG together with electrooptical measurements is used to characterize the so-called dark phase, which is an optically isotropic phase with smectic order found in bent-core liquid crystal compounds. A material with two variants of this type of phase (one homochiral and the other racemic) depending on the field treatment is found and studied. The local structure is shown to be antiferroelectric and the saddle-splay distortion leading to this sponge-like phase is concluded to have a steric origin, due to the impossibility of molecules to accommodate in flat layers.

  From the practical viewpoint, we have demonstrated the possibility of constructing an LCD using this phase and the performance of the device has been evaluated.

- The B4 phase has been reviewed in this thesis. Its X-ray diffraction diagram has been fully indexed, its electron density diagram calculated and even an aligned sample obtained. A local antiferroelectric structure is proposed, accounting for some phenomena that other structural models failed to explain, such as its low SHG efficiency.

- Bent-core molecules incorporating TTF units have been shown to give rise to materials with interesting properties and functionalities. Apart from an improved SHG efficiency, the material presents interesting photoinduced effects as photoconductivity or chiral segregation under field if the sample has been exposed to UV light.

References

[1] P. J. Collings, M. Hird, *Introduction to Liquid Crystals. Chemistry and Physics*, CRC Press, 1997.

[2] P. G. de Gennes, J. Prost, *Physics of Liquid Crystals*, Clarendon Press, 1993.

[3] R. Amaranatha Reddy *et al.*, J. Mat. Chem. **16**, 907 (2006)

[4] H. Takezoe *et al.*, Jpn. J. Appl. Phys. **45**, 597 (2006)

[5] J. Etxebarria *et al.*, J. Mat. Chem. **18**, 2919 (2008)

[6] A. Yariv, *Quantum Electronics*, Wiley, 1989.

[7] I. Alonso, *Nonlinear optical and structural properties of new bent-core liquid crystal materials* (PhD Thesis), 2008

[8] M. Nakata, *Chirality and Polarity in Bent-core Liquid Crystals* (PhD Thesis), 2006

[9] O. Lehmann, Z. Physikal. Chem. **4**, 462 (1889)

[10] F. Reinitzer, Monatsh Chem. **9**, 421 (1888)

[11] G. T. Stewart, Liq. Cryst. **30**, 541 (2003)

[12] G. T. Stewart, Liq. Cryst. **31**, 443 (2004)

[13] S. Chandrasekhar *et al.*, Pramana **9**, 471 (1977)

[14] S. Chandrasekhar *et al.*, Liq. Cryst. **24**, 67 (1998)

[15] T. J. Dingemans *et al.*, J. Phys. Chem. B **105**, 8845 (2001)

[16] S. Huh, Liq. Cryst. **25**, 285 (1998)

[17] J. Ortega *et al.*, Liq. Cryst. **23**, 285 (1997)

[18] R. B. Meyer *et al.*, J. Phys., Lett. (Orsay, Fr.) **36**, L69 (1975)

[19] T. Niori *et al.*, J. Mat. Chem **6**, 1231 (1996)

[20] D. R. Link *et al.*, Science **278**, 1924 (1997)

[21] C. Keith *et al.*, Chem. Eur. J **13**, 2556 (2007)

[22] G. Heppke *et al.*, Phys. Rev. E **60**, 5575 (1999)

[23] J. Bedel *et al.*, Phys. Rev. E **69**, 061702 (2004)

[24] M. Nakata *et al.*, Phys. Rev. Lett. **96**, 067802 (2006)

[25] D. A. Coleman *et al.*, Science **301**, 1204 (2003)

[26] N. Vaupotic *et al.*, Phys. Rev. E **72**, 031701 (2006)

[27] M. Nakata *et al.*, Phys. Rev. E **71**, 011705 (2005)

[28] J. Ortega *et al.*, Phys. Rev. E **69**, 011703 (2004)

[29] R. A. Reddy *et al.*, Chem. Mater. **16**, 4050 (2004)

[30] C. L. Folcia *et al.*, Chem. Mat. **18**, 4617 (2006)

[31] I. Alonso *et al.*, Phys. Rev. E **78**, 041701 (2008)

[32] E. Gorecka *et al.*, ChemPhysChem **6**, 1807 (2005)

[33] E. Gorecka *et al.*, Chem. Mater. **19**, 3027 (2007)

[34] N. Vaupotic *et al.*, Soft Matter **5**, 2281 (2009)

[35] Ingo Dierking, *Textures of Liquid Crystals*, Wiley-VCH, 2003.

[36] X. Zeng *et al.*, Nature Mater. **4**, 562 (2005)

[37] J. Ortega *et al.*, Liq. Cryst. **31**, 579 (2004)

[38] F. Araoka *et al.*, Jpn. J. Appl. Phys. **38**, 3526 (1999)

[39] J. Ortega *et al.*, Phys. Rev. E **63**, 011702 (2001)

[40] W. N.Herman *et al.*, J. Opt. Soc. Am. B **12**, 416 (1995)

[41] F. Kentischer *et al.*, Liq. Cryst. **25**, 341 (1998)

[42] S.-W. Choi *et al.*, Jpn. J. Appl. Phys. **37**, 3408 (1998)

[43] R. Macdonald *et al.*, Phys. Rev. Lett. **81**, 4408 (1998)

[44] J.-Y. Liu *et al.*, J. Appl. Phys. **70**, 3426 (1991)

[45] F. Araoka *et al.*, Phys. Rev. E **66**, 021705 (2002)

[46] S.T. Lagerwall, P.G. Rudquist, D. S. Hermann, *Encyclopedia of Optical Engineering Vol. 12*, Marcel Dekker Inc., 2003.

[47] H. E. Katz *et al.*, J. Am. Chem. Soc **116**, 6636 (1994)

[48] I. C. Pintre *et al.*, Chem. Mat. **18**, 4617 (2006)

[49] L. T. Cheng *et al.*, J. Phys. Chem. **95**, 10641 (1991)

[50] J. Jerphagnon *et al.*, J. Appl. Phys. **41**, 1667 (1970)

[51] D. M. Walba *et al.*, J. Am. Chem. Soc. **118**, 1211 (1996)

[52] Y. Zhang *et al.*, (to be published), (2009)

[53] M. Schadt, Liq. Cryst. **14**, 73 (1993)

[54] J. L. Segura *et al.*, Angew. Chem., Int. Ed. **40**, 1372 (2001)

[55] M. R. J. Bryce, Chem. Soc. Rev. **20**, 355 (1991)

[56] N. S. Nalwa, *Handbook of Organic Conductive Molecules and Polymers*, Wiley, 1997.

[57] M. R. J. Bryce, J. Mater. Chem. **10**, 589 (2000)

[58] G. Dantlgraber *et al.*, Chem. Mat. **14**, 1149 (2002)

[59] H. N. Shreenivasa Murthty *et al.*, Liq. Cryst. **13**, 1347 (2004)

[60] H. N. Shreenivasa Murthty *et al.*, J. Mat. Chem **16**, 1634 (2006)

[61] J. Kirchhoff *et al.*, Appl. Phys. Lett. **90**, 161905 (2007)

[62] C. L. Folcia *et al.*, Phys. Rev. E **74**, 031702 (2006)

[63] T. Sekine *et al.*, J. Mater. Chem. **8**, 1307 (1997)

[64] J. Martínez-Perdiguero *et al.*, Phys. Rev. E **74**, 031701 (2003)

[65] G. Heppke *et al.*, Liq. Cryst. **27**, 313 (2000)

[66] W. Weissflog *et al.*, Liq. Cryst. **31**, 923 (2004)

[67] G. Heppke *et al.*, Phys. Rev. E **60**, 5575 (1999)

[68] R. Kuroda, Rev. Sci. Instrum. **72**, 3802 (2001)

[69] L. E. Hough *et al.*, Phys. Rev. Lett. **98**, 037802 (2007)

[70] L. E. Hough *et al.*, Phys. Rev. Lett. **95**, 107802 (2005)

[71] J. Etxebarria *et al.*, Phys. Rev. E **101**, 079801 (2008)

[72] J. Thisayukta *et al.*, J. Am. Chem. Soc. **122**, 7741 (2000)

[73] S. Choi *et al.*, Chirality **19**, 250 (2007)

[74] T. Sekine *et al.*, J. Mater. Chem. **8**, 1307 (1997)

[75] G. Pelzl *et al.*, Adv. Mater. (Weinheim, Ger.) **11**, 707 (1999)

[76] L. Hough *et al.*, *Poster B18*, 10th FLCC, Stare Jablonky, Poland, 2005.

[77] F. Araoka *et al.*, Phys. Rev. Lett. **94**, 137801 (2005)

[78] H. Niwano, J. Phys. Chem. B **108**, 14889 (2004)

[79] J. Martínez-Perdiguero *et al.*, J. Mater. Chem (accepted), (2009)

[80] D. M. Walba *et al.*, Cryst. Growth Des. **5**, 2091 (2005)

[81] M. Nakata *et al.*, Liq. Cryst. **28**, 1301 (2001)

[82] I. C. Pintre *et al.*, J. Mater. Chem. **17**, 2219 (2007)

[83] J. Thisayukta *et al.*, Jpn. J. Appl. Phys. **40**, 3277 (2001)

[84] A. Immirzi *et al.*, Act. Cryst. A **33**, 216 (1977)

[85] A. I. Kitaigorodski, *Molekülkristalle*, Akademieverlag, 1979.

[86] T. Sekine *et al.*, Jpn. J. Appl. Phys. **36**, 6455 (1997)

[87] M. Zennyoji *et al.*, Mol. Cryst. Liq. Cryst. **366**, 2545 (2001)

[88] E. Gorecka *et al.*, Phys. Rev. Lett. **85**, 2526 (2000)

[89] H. Kurosu *et al.*, J. Phys. Chem. A **108**, 4674 (2004)

[90] D. M. Walba *et al.*, Cryst. Growth Des. **5**, 2091 (2005)

[91] J. Ortega *et al.*, Phys. Rev. E **68**, 011707 (2003)

[92] A. Jákli *et al.*, Adv. Mat. **15**, 1606 (2003)

[93] L. E. Hough, *Layer Curvature and Optical Activity in BentCore Liquid Crystalline Phases* (PhD Thesis), 2007

[94] H.T. Hyde at al., Science **1**, 653 (1996)

[95] B. A. DiDonna *et al.*, Phys. Rev. Lett. **86**, 215504 (2002)

[96] D. Shen *et al.*, J. Am. Chem. Soc. **122**, 1593 (2000)

[97] S. Diez *et al.*, Liq. Cryst. **30**, 1407 (2003)

[98] J. Etxebarria *et al.*, Phys. Rev. E **67**, 042702 (2003)

[99] P. Pyc *et al.*, J. Mat. Chem. **14**, 2374 (2004)

[100] D. Pociecha *et al.*, Phys. Rev. E **72**, 060701 (2005)

[101] M. W. Schröder *et al.*, J. Mat. Chem **18**, 1877 (2003)

[102] R. Amaranatha Reddy *et al.*, Liq. Cryst. **30**, 1031 (2003)

[103] W. Weissflog *et al.*, Adv. Mat. **15**, 630 (2003)

[104] M. W. Schröder *et al.*, Liq. Cryst. **31**, 633 (2004)

[105] C. Keith *et al.*, J. Am. Chem. Soc. **128**, 3051 (2006)

[106] K. Miyasato, Jpn. J. Appl. Phys., Suppl. **22**, L661 (1983)

[107] J. Barberá *et al.*, J. Am. Chem. Soc. **126**, 7190 (2004)

[108] J. A. Gallastegi *et al.*, J. Appl. Phys. **98**, 083501 (2005)

[109] R. Amaranatha Reddy *et al.*, J. Mat. Chem. **16**, 907 (2006)

[110] A. Jakli *et al.*, Phys. Rev. E **67**, 051702 (2003)

[111] A. Jákli *et al.*, Liq. Cryst. **29**, 377 (2002)

[112] Y. Shimbo *et al.*, Jpn. J. Appl. Phys. **45**, L282 (2006)

[113] M. Schadt *et al.*, Appl. Phys. Lett. **18**, 127 (1971)

[114] W. Kiefer *et al.*, Proc. IDRC, 547 (1992)

[115] K. Ohmuro, SID Dig. Tech.Pap., 845 (1997)

[116] T. Nonaka, Liq. Cryst. **26**, 1599 (1999)

[117] J.M. Otón *et al.*, Optoelectronics Review **12**, 263 (2004)

[118] D. Pociecha *et al.*, Phys. Rev. Lett. **91**, 185501 (2003)

[119] Y. Shimbo *et al.*, Phys. Rev. Lett. **97**, 113901 (2006)

[120] I. Alonso *et al.*, Liq. Cryst. **34**, 655 (2007)

[121] M. Bendikov *et al.*, Chem. Rev. **104**, 4891 (2004)

[122] R. P. Shibaeva *et al.*, Chem. Rev. **104**, 5347 (2004)

[123] M. Mas-Torrent *et al.*, J. Am. Chem. Soc. **126**, 8546 (2004)

[124] M. Mas-Torrent *et al.*, ChemPhysChem **7**, 86 (2006)

[125] R. Andreu *et al.*, Synth. Met. **86**, 1869 (1997)

[126] R. Andreu *et al.*, Tetrahedron **54**, 3895 (1998)

[127] R. A. Bissell *et al.*, Chem. Commun. **1998**, 113 (1998)

[128] R. Andreu *et al.*, J. Mater. Chem. **8**, 881 (1998)

[129] M. Katsuhara *et al.*, Synth. Met. **149**, 219 (2005)

[130] J. Martínez-Perdiguero *et al.*, Phys. Rev. E **77**, 020701 (2008)

[131] I. C. Pintre *et al.*, Chem. Commun. **2008**, 2523 (2008)

[132] M. Funahashi *et al.*, Jpn. J. Appl. Phys. **35**, L703 (1996)

[133] I. C. Pintre, *Materiales funcionales basados en cristales líquidos de tipo banana. Diseño, síntesis y caracterización* (PhD Thesis), 2009

[134] Y. Takanishi *et al.*, Angew. Chem., Int. Ed. **38**, 2354 (1999)

[135] A. Kane, ChemPhysChem **8**, 170 (2007)

[136] A. Sicilia *et al.*, Phys. Rev. Lett. **101**, 197801 (2008)

[137] J. J. Arenzon *et al.*, Phys. Rev. Lett. **98**, 145701 (2007)

[138] M. Eich *et al.*, Makromol. Chem. **8**, 59 (1987)

[139] G. G. Nair *et al.*, J. Appl. Phys. **90**, 48 (2001)

[140] H. Kim *et al.*, Phys. Rev. E **69**, 061701 (2004)

[141] A. Jákli *et al.*, Phys. Rev. E **71**, 021705 (2005)

[142] D. Adam *et al.*, Phys. Rev. Lett. **70**, 457 (1993)

[143] M. Funahashi *et al.*, Phys. Rev. Lett. **78**, 2184 (1997)

[144] N. S. Nalwa, *Handbook of Organic Conductive Molecules and Polymers*, Wiley, 1997.

[145] Various authors, Chem. Rev. **104**, 4887 (2004)

[146] J. Ortega *et al.*, Phys. Rev. E **68**, 011707 (2003)

[147] J. Martínez-Perdiguero *et al.*, Phys. Rev. E **75**, 031701 (2006)

[148] J. Ortega *et al.*, Phys. Rev. E **69**, 011703 (2004)

[149] J. Szydlowska *et al.*, Phys. Rev. E **67**, 031702 (2003)

[150] C. Keith *et al.*, Chem. Mater. **19**, 694 (2007)

[151] V. Kopsky and D. B. Litvin, *International Tables for Cystallography, Subperiodic Groups* , Kluwer Academic, 2002.

[152] N. Vaupotic *et al.*, Phys. Rev. Lett. **98**, 247802 (2007)

List of publications

" Highly efficient nonlinear optical response from a bent-core liquid liquid crystal"
Ros, M. B.; Pintre, I. C.; Serrano J. L.; Martinez-Perdiguero, J.; Alonso, I.; Ortega, J.; Folcia, C. L.; Etxebarria, J.; Alicante, R.; Villacampa, B.
Chemistry of Materials, (submitted) (2009)

"Azo-Bridged Dimer-Like Ferroelectric Liquid Crystals for Second-Order Nonlinear Optics: Ferroelectricity and Second Harmonic Generation"
Zhang, Y.; Martínez-Perdiguero, J.; Baumeister, U.; Walker, C.; Etxebarria, J.; Tschierske, C.; O'Callaghan, M. J.; Handschy, M.
Journal of the American Chemical Society, (submitted) (2009)

"*Local structure of the B4 phase studied by second-harmonic generation and X-ray diffraction measurements*"
Martínez-Perdiguero, J.; Alonso, I.; Folcia, C. L.; Etxebarria, J.; Ortega, J.
Journal of Materials Chemistry **19**, 5161 (2009)

"*Experimental test of curvature-driven dynamics in the phase ordering of a twodimensional liquid crystal*"
Sicilia, A.; Arenzon, J. J.; Dierking, I.; Bray, A. J.; Cugliandolo, L. F.; Martínez-Perdiguero, J.; Alonso, I.; Pintre, I. C.
Physical Review Letters **101**, 197801 (2008)

"*Polar structures of bent-core liquid crystals with tetrathiafulvalene units*"
Alonso, I.; Martínez-Perdiguero, J.; Folcia, C. L.; Etxebarria, J.; Ortega, J.; Pintre, I. C.; Ros, M. B.
Physical Review E **78**, 041701 (2008)

"*TTF-based bent-core liquid crystals*"
Pintre, I. C.; Serrano, J. L.; Ros, M. B.; Ortega, J.; Alonso, I.; Martínez-Perdiguero, J.; Folcia, C. L.; Etxebarria, J.; Goc, F.; Amabilino, D. B.; Puigmartí-Luis, J.;

Gomar-Nadal, E.
ChemComm, 2523 (2008)

"*Bent-core liquid-crystalline derivative of tetrathiafulvalene: Photoresponsivity and deracemization*"
Martínez-Perdiguero, J.; Alonso I.; Ortega, J.; Folcia, C. L.; Etxebarria, J.; Pintre, I. C.; Ros, M. B.; Amabilino, D.
Physical Review E **77**, 020701 (2008)

"*Characteristics of a liquid crystal display using optically isotropic phases of bentcore mesogens*"
Alonso, I.; Martínez-Perdiguero, J.; Ortega, J.; Folcia, C. L.; Etxebarria, J.
Liquid Crystals, **34,** 655 (2007)

"*Some aspects about the structure of the optically isotropic phase in a bent-core liquid crystal: chiral, polar, or steric origin*"
Martínez-Perdiguero, J.; Alonso, I.; Folcia, C. L.; Etxebarria, J.; Ortega, J.
Physical Review E **74**, 031701 (2006)